

EXPLORING ULTRASONIC ADDITIVE MANUFACTURING FROM
MODELING TO THE DEVELOPMENT OF A SMART METAL-MATRIX
COMPOSITE

A Thesis

Submitted to the Faculty

of

Purdue University

by

Dennis M. Lyle

In Partial Fulfillment of the

Requirements for the Degree

of

Master of Science in Mechanical Engineering

May 2020

Purdue University

West Lafayette, Indiana

THE PURDUE UNIVERSITY GRADUATE SCHOOL
STATEMENT OF THESIS APPROVAL

Dr. James M. Gibert, Chair

School of Mechanical Engineering

Dr. Fabio Semperlotti

School of Mechanical Engineering

Dr. J. Stuart Bolton

School of Mechanical Engineering

Approved by:

Dr. Nicole L. Key

Head of the Mechanical Engineering Graduate Program

ACKNOWLEDGMENTS

I would like to thank my advisor, Dr. James Gibert, for his patience with me and his continuing guidance on this research topic. I would like to thank my committee members: Dr. J. Stuart Bolton and Dr. Fabio Semperlotti for being part of this process and providing feedback to make me a better researcher.

Additionally, I would like to thank Hongcheng Tao for his help with developing triboelectric sensors, and Sami Khreisat for his help with the operation of the UAM machine. I would like to thank Dr. Francesco Danzi for his interesting conversations on various research topics. I would like to thank Mark Norfolk for his support with our UAM machine and allowing me to visit the Fabrisonic facility to learn more about the UAM process. I would like to thank the Herrick facility staff for providing me the tools and assistance necessary to perform experiments.

Finally, I would like to thank my parents, without whom I would not be here and their unconditional love and support has allowed me to achieve this.

TABLE OF CONTENTS

	Page
LIST OF TABLES	vii
LIST OF FIGURES	viii
ABSTRACT	xiii
1. INTRODUCTION	1
1.1 Overview	1
1.1.1 Advantages and Disadvantages of UAM Process	5
1.2 Literature Review	7
1.2.1 Previous UAM Modeling	7
1.2.2 Embedding Smart Materials in Metal-Matrices via UAM	10
1.3 Motivation	12
1.4 Thesis Outline	12
2. UAM MODELING DERIVATION	14
2.1 Introduction	14
2.2 Governing Equation	15
2.3 Free Vibration	16
2.3.1 Orthogonality of the Approximate Mode Shapes	19
2.4 Forced Vibration	19
2.5 Forcing Models	21
2.5.1 Pure Stick Forcing Model Definition	22
2.5.2 Pure Slip Forcing Model Definition	23
2.5.3 Partial Slip Forcing Model Definition	24
2.6 Summary	24
3. UAM MODELING RESULTS	26
3.1 Introduction	26
3.2 Free Vibration Solution	27
3.2.1 Convergence Analysis	27
3.2.2 Substrate Resonance and Mode Shape Analysis	28
3.3 Transverse Velocity Response in Comparison to Experimental Results	32
3.3.1 Transverse Velocity Response at $a = 0.5$ in	34
3.3.2 Transverse Velocity Response at $a = 0.75$ in	36
3.3.3 Transverse Velocity Response at $a = 1$ in	37
3.3.4 Transverse Velocity Response at $a = 2$ in	39
3.3.5 Transverse Velocity Response at $a = 2.5$ in	39

	Page
3.4 Selective Time Traces of Response	42
3.4.1 Selective Time Traces for $a = 1$ in	43
3.4.2 Selective Time Traces at $a = 2$ in	50
3.4.3 Selective Time Traces at $a = 2.5$ in	56
3.5 Transverse Velocity Response to Variations in Substrate Height	62
3.5.1 Critical Height-To-Width Ratio At Substrate Width of 0.5 in . .	65
3.6 Summary	66
4. EMBEDDING TRIBOELECTRIC NANOGENERATOR IN METAL MA- TRIX VIA UAM	69
4.1 Introduction	69
4.2 Triboelectric Nanogenerator	69
4.3 Design of TENG-AL3003 Composites	71
4.4 Fabrication of TENG-AL3003 Composites	73
4.5 Experimental Testing of TENG-AL3003 Composites	77
4.5.1 Touch Testing	78
4.5.2 Solenoid Testing	81
4.5.3 Drop Testing	85
4.6 Summary	87
5. CONCLUDING REMARKS	89
5.1 Summary	89
5.2 Contributions	90
5.3 Future Work	91
REFERENCES	93
A. MODESHAPES	99
B. MODEL VALIDATION	101
B.1 Model Approximation of Euler-Bernoulli Beam Response	101
B.1.1 Pure Stick Forcing Euler-Bernoulli Beam Approximation . . .	102
B.1.2 Pure Slip Forcing Euler-Bernoulli Beam Approximation . . .	103
B.1.3 Partial Slip Forcing Euler-Bernoulli Beam Approximation . .	105
B.2 Code and Model Validation through ODE45 Comparison	107
B.2.1 Pure Stick Forcing ODE45 Comparison	107
B.2.2 Pure Slip Forcing ODE45 Comparison	108
B.2.3 Partial Slip Forcing ODE45 Comparison	109
C. RAW EXPERIMENTAL DATA FOR SOLENOID TESTING	112
D. FRICTION COEFFICIENT RELATIONSHIP WITH SUBSTRATE MODEL RESPONSE	116
E. EXPERIMENTAL CALIBRATION OF SONOTRODE VIBRATION AM- PLITUDE	119

F. FABRISONIC R220 SONOTRODE CLEANING PROCEDURE	121
---	-----

LIST OF TABLES

Table	Page
3.1 Material properties for AL3003 at 25C.	27
3.2 Comparison of Galerkin Approximation with Finite Element Model Natural Frequencies.	29
3.3 Critical heights versus natural frequencies of substrate.	31
3.4 Parameter values for model simulation of forced response for experimental comparison.	33
4.1 Estimated signal-to-noise ratio analysis for touch testing results from Figure 4.6.	79
4.2 Parameter list for solenoid testing	81
4.3 Estimated signal-to-noise ratio analysis for preliminary solenoid testing (5 V, 1 Hz) from Figure 4.8.	84
4.4 Estimated signal-to-noise ratio analysis for drop testing results from Figure 4.11.	87
B.1 Parameter list of Euler-Bernoulli beam approximation for pure stick forcing	103
B.2 Parameter list of Euler-Bernoulli beam approximation for pure slip forcing	104
B.3 Parameter list of Euler-Bernoulli beam approximation for partial slip forcing	106
B.4 ODE45 Parameter list for pure stick forcing	108
B.5 ODE45 Parameter list for pure slip forcing	109
B.6 ODE45 Parameter list for partial slip forcing	110

LIST OF FIGURES

Figure	Page
1.1 (a) Overview of ultrasonic additive manufacturing process, and (b) metal combinations that can be ultrasonically welded [3]	1
1.2 Acoustic softening versus thermal softening of aluminum specimens from [14].	3
2.1 Schematic of the 3-D parallelepiped UAM model with dimensions $a \times b \times c$ subjected to a moving line load.	15
3.1 First six modeshapes of dimension 1.0 in \times 1.0 in \times 2.5 (additional dimensions can be seen in Appendix A) with natural frequencies : a) $f_1 = 21863.74$ Hz, b) $f_2 = 24990.16$ Hz, c) $f_3 = 27524.47$ Hz, d) $f_4 = 38661.71$ Hz, e) $f_5 = 44142.78$ Hz, and f) $f_6 = 53281.16$ Hz.	30
3.2 Semilog plot of first ten natural frequencies versus substrate height c . Dotted red line indicates 20 kHz operating frequency of sonotrode.	31
3.3 Transverse velocity response directly under forcing model moving line load compared to experimental response from [17] for substrate height $a = 0.5$ in.35	
3.4 Transverse velocity response directly under forcing model moving line load compared to experimental response from [17] for substrate height $a = 0.75$ in.36	
3.5 Transverse velocity response directly under forcing model moving line load compared to experimental response from [17] for substrate height $a = 1$ in (the response in [17] is for $a = 0.9375$ in).	38
3.6 Transverse velocity response directly under forcing model moving line load compared to experimental response from [17] for substrate height $a = 2$ in. 40	
3.7 Transverse velocity response directly under forcing model moving line load for substrate height $a = 2.5$ in.	41
3.8 Pure stick forcing transverse velocity response for substrate height $a = 1$ in broken down. The first column is transverse velocity response modal contributions, the second column is the modal response in blue and forcing in red at $t = 0$ s, and third column is the modal response in blue and forcing in red at $t = 0.75$ s.	44

Figure	Page
3.9 Pure slip forcing transverse velocity response for substrate height $a = 1$ in broken down. The first column is transverse velocity response modal contributions, the second column is the modal response in blue and forcing in red at $t = 0$ s, and third column is the modal response in blue and forcing in red at $t = 0.75$ s.	47
3.10 Partial slip forcing transverse velocity response for substrate height $a = 1$ in broken down. The first column is transverse velocity response modal contributions, the second column is the modal response in blue and forcing in red at $t = 0$ s, and third column is the modal response in blue and forcing in red at $t = 0.75$ s.	49
3.11 Pure stick forcing transverse velocity response for substrate height $a = 2$ in broken down. The first column is transverse velocity response modal contributions, the second column is the modal response in blue and forcing in red at $t = 0$ s, and third column is the modal response in blue and forcing in red at $t = 0.75$ s.	51
3.12 Pure slip forcing transverse velocity response for substrate height $a = 2$ in broken down. The first column is transverse velocity response modal contributions, the second column is the modal response in blue and forcing in red at $t = 0$ s, and third column is the modal response in blue and forcing in red at $t = 0.75$ s.	53
3.13 Partial slip forcing transverse velocity response for substrate height $a = 2$ in broken down. The first column is transverse velocity response modal contributions, the second column is the modal response in blue and forcing in red at $t = 0$ s, and third column is the modal response in blue and forcing in red at $t = 0.75$ s.	55
3.14 Pure stick forcing transverse velocity response for substrate height $a = 2.5$ in broken down. The first column is transverse velocity response modal contributions, the second column is the modal response in blue and forcing in red at $t = 0$ s, and third column is the modal response in blue and forcing in red at $t = 0.75$ s.	57
3.15 Pure slip forcing transverse velocity response for substrate height $a = 2.5$ in broken down. The first column is transverse velocity response modal contributions, the second column is the modal response in blue and forcing in red at $t = 0$ s, and third column is the modal response in blue and forcing in red at $t = 0.75$ s.	59

Figure	Page
3.16 Partial slip forcing transverse velocity response for substrate height $a = 2.5$ in broken down. The first column is transverse velocity response modal contributions, the second column is the modal response in blue and forcing in red at $t = 0$ s, and third column is the modal response in blue and forcing in red at $t = 0.75$ s.	60
3.17 Maximum and RMS of transverse velocity response directly under forcing model moving line load versus height for substrate of width $b = 1$ in, text arrows indicate dominant modes.	63
3.18 Maximum and RMS of transverse velocity response directly under forcing model moving line load versus height for substrate of width $b = 0.5$ in, text arrows indicate dominant modes.	67
4.1 Vertical contact mode triboelectric nanogenerator: (a) schematic of two dielectric generator, (b) process of contact electrification, and (c) triboelectric series that is an amalgamation of several different series from the literature [64].	70
4.2 Triboelectric metal-matrix composite: (a) embedded TENG sensor cross-section with ITO/PET and Kapton dielectric layers, (b) single sensor channel design, (c) single sensor pocket design, and (d) pocket design sensor array.	72
4.3 Schematic of complete manufacturing and assembly of TENG metal-matrix composites using UAM.	74
4.4 Prototypes of TENG metal-matrix composites: (a) sensor B, (b) sensors C and D, and (c) sensor E.	76
4.5 Experimental touch test setup: (a) schematic of test setup and (b) picture of test setup	79
4.6 Touch testing results: (a) sensor B (pocket design) touch test response, (b) sensors C and D (pocket design sensor array) touch test responses, and (c) sensor E (channel design) touch test response.	80
4.7 Experimental solenoid test setup: (a) schematic of test setup and (b) picture of test setup	82
4.8 Preliminary solenoid testing results: (a) sensor C (pocket design) response to 5 V and 1 Hz solenoid actuation, (b) sensor D (pocket design) response to 5 V and 1 Hz solenoid actuation, and (c) sensor E (channel design) response to 5 V and 1 Hz solenoid actuation.	83
4.9 Calibration of the average impulse peaks of the sensor output voltage to the solenoid input voltage: (a) sensor C and (b) sensor D.	84

Figure	Page
4.10 Experimental drop test setup	85
4.11 Drop testing results: (a) sensor C (pocket design) drop test response, (b) sensor D (pocket design) drop test response, and (c) sensor E (channel design) drop test response.	86
A.1 First six modes of dimension $2.0 \text{ in} \times 1.0 \text{ in} \times 2.5$ with natural frequencies: a) $f_1 = 7182.97 \text{ Hz}$, b) $f_2 = 11476.17 \text{ Hz}$, c) $f_3 = 11611.02 \text{ Hz}$, d) $f_4 = 25498.50 \text{ Hz}$, e) $f_5 = 25597.53 \text{ Hz}$, and f) $f_6 = 27992.99 \text{ Hz}$. .	99
A.2 First six modes of dimension $2.5 \text{ in} \times 1.0 \text{ in} \times 2.5$ with natural frequencies: a) $f_1 = 4828.97 \text{ Hz}$, b) $f_2 = 8498.22 \text{ Hz}$, c) $f_3 = 9017.96 \text{ Hz}$, d) $f_4 = 19795.63 \text{ Hz}$, e) $f_5 = 20560.21 \text{ Hz}$, and f) $f_6 = 22613.99 \text{ Hz}$. . .	100
B.1 Pure stick forcing model approximation compared to exact solution of Euler-Bernoulli beam vibration response.	103
B.2 Pure slip forcing model approximation compared to exact solution of Euler-Bernoulli beam vibration response.	105
B.3 Partial slip forcing model approximation compared to exact solution of Euler-Bernoulli beam vibration response.	106
B.4 Semi-analytical convolution response and ODE45 response to pure stick forcing using parameters listed in Table B.4.	108
B.5 Semi-analytical convolution response and ODE45 response to pure slip forcing using parameters listed in Table B.5.	110
B.6 Semi-analytical convolution response and ODE45 response to partial slip forcing using parameters listed in Table B.6.	111
C.1 Solenoid testing for sensor C, where the subfigure caption contains the respective solenoid voltage amplitude and actuation frequency.	113
C.2 Solenoid testing for sensor D, where the subfigure caption contains the respective solenoid voltage amplitude and actuation frequency.	114
C.3 Solenoid testing for sensor E, where the subfigure caption contains the respective solenoid voltage amplitude and actuation frequency.	115
D.1 The transverse velocity response under the moving line load for pure stick forcing with different coefficients of friction, μ	117
D.2 Maximum and RMS value of transverse velocity response of substrate with dimensions $a = 0.5 \text{ in}$, $b = 1 \text{ in}$, and $c = 2.5 \text{ in}$, to pure stick forcing for various coefficients of friction.	118

Figure	Page
E.1 Fabrisonc R220 sonotrode, marked by dotted red line, with red dot on face indicating measurement location for calibration.	119
E.2 Sonotrode vibration amplitude versus controller amplitude percent in free air. The line marked 'PU' is the calibration curved developed when the Fabrisonic R220 was at Purdue University and the line marked 'UL' is when it was at University of Louisville.	120
F.1 Sonotrode cleaning set-up on Fabrisonic R220 UAM machine with sonotrode, plastic cup, and NaOH solution labeled.	122

ABSTRACT

Lyle, Dennis M. MSME, Purdue University, May 2020. Exploring Ultrasonic Additive Manufacturing from Modeling to the Development of a Smart Metal-Matrix Composite. Major Professor: James M. Gibert, School of Mechanical Engineering.

The advent of additive manufacturing has opened up new frontiers in developing metal structures that can have complex geometries, composite structures made of dissimilar metals, and metal structures with embedded sensing and actuation capabilities. These types of structures are possible with ultrasonic additive manufacturing (UAM); a novel manufacturing technology that combines additive manufacturing through the ultrasonic welding of thin metal foils with computer numerical control (CNC) milling. However, the process suffers from a critical limitation, i.e., a range of build heights within which bonding between a foil and the substrate cannot be originated. This work has two research objectives, the first is a fundamental understanding of the complex dynamic interaction between the substrate and ultrasonic horn, or sonotrode. Specifically, it focuses on the effects that specific modes of vibration have on the dynamic response of the substrate. The second objective is to utilize the UAM process to create metal structures with an embedded sensor that can detect contact or impact. In addressing the first objective, a semi-analytical model was developed to determine the response to three forcing descriptions that approximate the interfacial friction between the foil and substrate induced by sonotrode compression and excitation. Several observations can be seen in the results: as the height increases the dominant modes of vibration change, the modes of vibration excited also change during a single weld cycle as the sonotrode travels across the length of the substrate, and finally the three forcing models do not have a significant impact on the substrate response trends with height and during the weld cycle. In addressing the second objective, three prototypes were created by embedding a triboelectric nano-

generator (TENG) sensor within an AL3003 metal-matrix. TENGs utilize contact electrification between surfaces of dissimilar materials, typically polymers, combined with electrostatic induction to generate electrical energy from a mechanical excitation. The sensors demonstrate a discernible response over a 1-5 Hz frequency range. In addition, the sensors have a linear relationship between output voltage and a mechanically applied load, and have the ability to sense contact through both touch and due to an impacting object.

1. INTRODUCTION

1.1 Overview

Ultrasonic additive manufacturing (UAM) is a solid-state fabrication technique that consists of bonding layered foils of similar and dissimilar metals. UAM was first developed by Dawn White who founded Solidica, Inc. which manufactured the first commercial UAM system [1]. In 2011, Fabrisonic LLC was founded and now owns the UAM technology developed by Solidica Inc, [2]. Figure 1.1 a) shows an overview of the UAM process. The UAM process begins with placing a thin metal foil, ap-

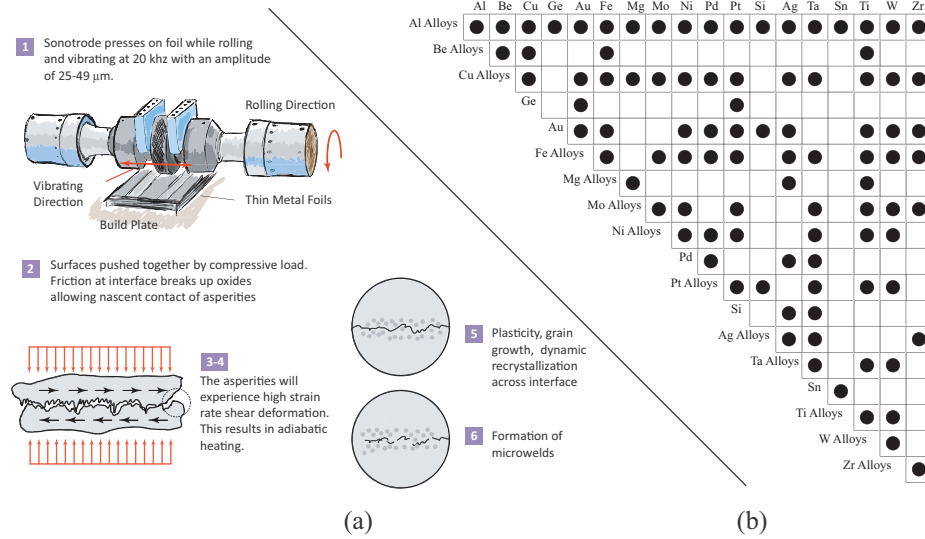


Figure 1.1. (a) Overview of ultrasonic additive manufacturing process, and (b) metal combinations that can be ultrasonically welded [3]

proximately 150 μm in thickness, onto a sacrificial baseplate that can be preheated. After foil placement, a rolling horn, commonly referred to as a sonotrode, compresses the foil and vibrates transversely at a nominal frequency of 20 kHz. The combination of compression and ultrasonic transverse vibrations results in bonding the foil to the

baseplate. After the first layer is bonded, additional layers are sequentially bonded to create a substrate, and a computer numerical control (CNC) mill is used to machine the previously consolidated layers into the desired contour of the final part. The commonly accepted theory of bond formation from [4–6] is as follows: the compression from the sonotrode brings the interfacial surfaces of the foil and baseplate into close contact; the sonotrode transverse vibrations induce differential motion between foil and baseplate to shear surface asperities and disperse surface oxides; the high frequency transverse vibrations result in high strain rate shear deformations causing plasticity and heating at the foil-baseplate interface; the high strain rate and heating induce grain growth and dynamic recrystallization across the interface; and finally microwelds are formed at the bonding interface. Although the bond formation is the result of many mechanisms, solid-state metal bonding requires at the least two conditions to be met: interfacial surfaces between workpieces must be cleaned of oxide layers or other contaminants, and the surfaces must be brought into intimate contact [7].

Not included in the previous discussion of the bonding mechanism for UAM is a phenomena known as ultrasonic or acoustic softening. There is not a commonly accepted theory elucidating the physics of acoustic softening; however, researchers do believe that it plays a part in bond formation [8–12]. Acoustic softening phenomenon was first noted by [13]. The observations of acoustic softening is that when ultrasonic vibrations are applied to various metal specimens there is a significant reduction in the yield stress, seen in Figure 1.2. During UAM, acoustic softening likely plays a role due to the ultrasonic vibrations of the sonotrode causing a reduction in the yield stresses of the foil and baseplate/substrate. The reduction in yield stress can, similarly to heating, increase plastic deformation at the foil-substrate interface resulting in better bond formation.

Although UAM is a relatively new additive manufacturing technique, the development was based on ultrasonic metal welding process (UMW) that was developed in the 1950s and 1960s. The UMW process consists of two workpieces that are clamped

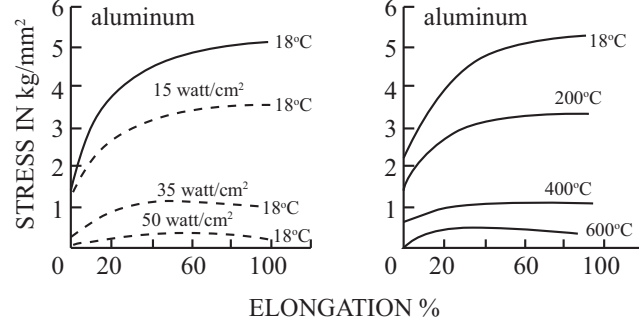


Figure 1.2. Acoustic softening versus thermal softening of aluminum specimens from [14].

between a weld tip, similar to the sonotrode, and an anvil [15]. The mechanism of bonding is that the friction between the two workpieces clears and disperses surface oxides at the bonding interface, which combined with the compression allows for intimate pure metal-to-metal contact [15]. The process and mechanism between the two manufacturing techniques, UAM and UMW, are similar but there are a few key differences. In UMW, the welding time is on the order of seconds, whereas in UAM the welding time is on the order of milliseconds. This is due to the rolling sonotrode that requires a higher normal force and power input in UAM. The benefit of the longer welding time in UMW is that capturing the dynamics of the workpieces during bonding is much less challenging.

An issue that plagues UAM is the critical height-to-width ratio, at which subsequent bonding of foil layers is no longer possible. This issue was first noted by [16], who experimentally demonstrated that changing the height-to-width ratio of the substrate affected bonding. As the height-to-width ratio approached one, bonding between the subsequent foil and the substrate could no longer occur. They theorized that the failure in bonding was due to an increase in static compliance of the substrate which reduced differential motion between foil and substrate that is required to break surface oxide layers. [17] experimentally demonstrated similar findings as [16], however, height-to-width ratios above the critical height-to-width ratio were also tested. They discovered that bonding could be reinitiated above the critical height-to-width

ratio, and theorized that resonances in the substrate increased its dynamic compliance resulting in the less differential motion between foil and substrate. This theory was tested by measuring the substrate response in the sonotrode vibration direction directly underneath the sonotrode contact patch during a weld cycle. They found that response of the substrate increases as the height-to-width ratio approaches one, and then the response decreases after the height-to-width ratio is further increased past one. Although the substrate response can be used to approximate the differential motion, actual slip between foil and substrate during a weld cycle was not directly measured until [18] performed experimental testing using a photon Doppler velocimetry (PDV) system to capture the motion of the sonotrode, foil, and substrate simultaneously. They discovered that for a successful weld there is initially large slippage between foil and substrate that decreases during the weld time until the foil and substrate have similar velocity profiles in phase. For an unsuccessful weld, there was initial slippage between foil and substrate, however, the relative velocity between foil and substrate was about half as large as for the successful weld. The success of a weld was not controlled by height-to-width ratios, but rather the success of a weld was controlled by welding parameters. Due to the insufficient experimental testing of foil-substrate interface motion in UAM, UMW provides some additional insight into the welding process of UAM but with longer process times and static sonotrode location, i.e. not a rolling sonotrode. The sonotrode, foil, and substrate velocity profiles during UMW was studied in [19]. They found that initially there is a large relative velocity between foil and substrate that decreases over 50 ms until the relative velocity is near zero for the remainder of the welding process. This slip phase between foil and substrate occurs for approximately 20 to 30% of the total weld time. The experimental results from these studies indicate that a sufficiently large differential motion between foil and substrate is necessary for bonding to occur. In the absence of differential motion measurements, the response of the substrate can be used to approximate the magnitude of differential motion between foil and substrate, assuming little or no slip between foil and sonotrode.

1.1.1 Advantages and Disadvantages of UAM Process

Comparing UAM to other metal additive manufacturing techniques provides information on the advantages and disadvantages of the UAM process. Other common additive manufacturing techniques are selective laser melting (SLM), electron beam melting (EBM), and direct metal deposition (DMD) [20]. SLM and EBM are both powder bed fusion processes in which a metal powder is applied to a substrate, and a device selectively melts the powder to generate the cross-section for that layer [20]. The primary difference between the two processes is that SLM uses a laser whereas EBM uses an electron beam [20]. DMD is within a group of manufacturing techniques known as beam deposition processes. In DMD, powder or wire feeding can be utilized, however, the general process remains the same. A laser head is focused onto the top surface of the substrate forming a molten pool, and the feedstock, either powder or wire, is fed into the molten pool [20]. As compared to powder bed fusion processes, the placement and melting of the feedstock occurs simultaneously instead of sequentially. Thus, the previously described other manufacturing processes require that the metal-matrix must be melted and then solidified, whereas in UAM the process is entirely solid-state. The solid-state process is the basis for most of the advantages for UAM in the following discussion.

In SLM, EBM, and DMD, the operating temperature is above the melting temperature of the metal, whereas in UAM the process temperature is less than half of the melting temperature of the matrix material [1, 21]. The lower process temperature in UAM reduces the residual stresses and brittle intermetallic phases created in the metal-matrix, as compared to SLM, EBM, and DMD processes in which there is melting and subsequent solidification of the metal-matrix [1, 20]. Additionally, the lower process temperature allows embedding of sensitive electronics and sensors in metal-matrix composites without fear of damaging the components [1]. In order to embed components in a metal-matrix via SLM, inserts had to be placed between the metal-matrix and a piezoelectric sensor during the embedding process in order to

prevent the piezoelectrics from burning [22]. Placing an insert between the metal-matrix and embedded component reduces the accuracy of the measurement because there is no longer direct contact between the sensor and the metal-matrix. There are also safety concerns associated with SLM, EBM, and DMD processes, such as the high-temperature metallic powders are an explosive hazard in a combustible atmosphere [23]. Therefore, the atmosphere is tightly controlled to be inert in the case of SLM and DMB, and in the case of EBM a vacuum is used [20]. As a reminder, in UAM these safety hazards are not present due to the solid-state fabrication process.

Like most manufacturing techniques, the UAM process is not without its disadvantages. In UAM, any complex geometry of the structure must be milled from the substrate which produces excess waste material. There is potential for waste materials in SLM, EBM, and DMD, however, due to the selective nature of the melting there is less waste material and some can be recycled [20]. UAM is not effective at building complex external geometries, due to the requirement of sufficient stiffness to support the compressive load and transverse vibrations from the sonotrode. In SLM and EBM, the powder bed supports the complex external geometry during formation, and in DMD supporting structures can be printed [20]. In UAM, the material properties are anisotropic due to the presence of voids at the bonding interface and the cold rolling process induced by the sonotrode changing the grain orientation [20]. In DMD, the direction of deposition can be changed between layers to reduce the anisotropic material properties [20].

Although we have explored the advantages and disadvantages, something that has not been discussed that does not easily fit into either category is the desired matrix material. Much of UAM research has been focused on creating metal-matrices made of aluminum alloys [24]. Whereas for SLM, EBM, and DMD, the materials used are mainly much harder metals, such as titanium, stainless steel, inconel, etc [20]. This factor should be included in the decision process in determining which technique to utilize.

From this review of the various metal additive manufacturing processes, if the goal is to embed a component within a metal-matrix using aluminum, then implementation is much more straight-forward via the UAM process. If the goal is to build a complex external structure, then SLM, EMB, or DMD could be more viable manufacturing options.

1.2 Literature Review

In addressing the critical height-to-width ratio, dynamic models have been developed of the UAM process. The focus in reviewing previous literature will be on models developed to study this issue. Additionally, a great portion of UAM research has been devoted to developing smart metal-matrix composites. The focus in reviewing previous literature will be on composites created to sense their interaction with their respective environments.

1.2.1 Previous UAM Modeling

Previous UAM models can be broken into two categories: thermo-mechanical models that are focused on studying and characterizing bond formation, and dynamic models that are focused on studying the changes in dynamics of the substrate. The previous thermo-mechanical UAM models have found that plasticity increased by thermal and acoustic softening at the interface is the main mechanism to allow bond formation, but they have not performed height-to-width ratio studies to develop an understanding of the critical height-to-width ratio [8–11, 25–31].

To explore the cause of the critical height-to-width ratio, researchers have developed dynamic models of the UAM process focused on the dynamics of the substrate. The effect of substrate dynamics on UAM bond formation was first studied by [32] who developed a dynamic 2-D FEM model to understand the changing dynamics as the height-to-width ratio is varied. As the height-to-width ratio of the substrate increases towards the critical height-to-width ratio, the frictional stress amplitude and

contact interface displacement decreases. They attribute this reduction in frictional stress and relative motion at the critical height-to-width ratio to a complex 1-D wave interference pattern at the contact interface due to the substrate height. Continuing to increase the height-to-width ratio further decreases the frictional stress at the interface, but increases the relative motion at the contact interface.

The previous researchers continued with their work into [33], where they theorized that the stress-strain field in the substrate combined with friction and displacement at the foil-substrate interface at various build heights can be used to elucidate the cause of the critical height-to-width ratio. A 2-D dynamic FEM model was developed to explore the changing dynamics and determine bond strength by energy density at the interface. At the critical height-to-width ratio and greater, the contact interface displacement increases while the shear strain at the interface decreases such that plastic deformation is unlikely. To understand the decrease in shear strain, a 2-D dynamic vibration model of the substrate and sonotrode was developed. The shear strain distributions in the 2-D analytical solution match the shear strain distributions in the FEM model. The inability to bond at heights equal to and greater than the critical height-to-width ratio is due to a complex interference pattern from the induced vibration from the sonotrode.

Concurrent to the previous research efforts, [17, 34] used a 3-D cantilevered parallelepiped with a moving vibratory force to model the built feature or substrate during the UAM process. The model was simulated at discrete heights to demonstrate an increase in dynamic compliance as the substrate height approached the critical height-to-width ratio, and a decrease in dynamic compliance as the substrate height was further increased. They attributed this dynamic compliance phenomenon at the critical height-to-width ratio to a resonant interaction of the substrate first natural frequency with the sonotrode. From their 3-D model, a simpler 2-D lumped parameter model was developed with a slip parameter dependent on the first natural frequency to describe the relative motion between the foil and substrate. As the substrate height is approaching the critical height-to-width ratio, the foil and substrate

purely stick. However, as the height of the substrate is further increased, the motion returns to stick-slip.

Building upon the discovery of this stick-slip behavior, [35] developed a lumped-parameter model of the substrate to further study the relative motion between foil and substrate. The model approximates the substrate as a stack of shear stiffness springs in parallel, such that increasing the substrate height reduces the effective stiffness. The model demonstrated that as the build height approaches a critical ratio, the relative slip motion between foil and substrate becomes aperiodic with some sticking and some slipping. The aperiodic slip motion can produce uneven energy distribution in bonding region and cause bond degradation. They found that decreasing the coefficient of friction or normal load near a critical build height can cause the aperiodic motion to return to periodic motion.

A new dynamic model was not developed until [36,37], who experimentally found that the input power to excite the sonotrode during the UAM process was height dependent, and decreased as the build height increased. To understand the reason for this, they developed a linear time-invariant model of the welder system to correlate the shear force and current as inputs into the model with voltage and welder velocity as outputs. To determine the effect of substrate height on system dynamics, the substrate was modeled as a 2-D elastic cantilevered beam. This description of the dynamics of the substrate does not provide insights into why the critical height-to-width ratio occurs because the dynamic compliance of the substrate in their model asymptotically approaches a minimum at approximately 10 layers (or a height-to-width ratio of 0.05).

A thorough explanation of why bond formation degrades at the critical height-to-width ratio was missing from previous dynamic UAM models. Thus, [12] developed probably the most complete UAM process model by connecting complex thermo-mechanical models with dynamic models of the substrate to determine the effects of substrate dynamics on bond formation. Her model was broken into several coupled sub-models to account for material plasticity, thermal softening, acoustic softening,

friction, and substrate dynamics. The sub-models were implemented into an overall FEM model in ABAQUS. The simulation was run on a high-performance cluster of 80 processors for approximately 24 hours. For height-to-width ratio studies, the simulation time was 0.7 ms, or 14 cycles of vibration. As the height-to-width ratio approaches one, the response of the substrate approaches that of the sonotrode meaning there is little or no differential motion between foil and substrate. The friction stresses near the interface in the substrate decreases, thus resulting in less plastic deformation and causing bond degradation. The model results were used to estimate linear weld density of the bonded interface by including an asperity layer that could plastically deform. They found that the minimum linear weld density occurs at a height-to-width ratio of 1.2.

1.2.2 Embedding Smart Materials in Metal-Matrices via UAM

From near its inception as a commercial manufacturing technology, embedding materials and devices to create smart metal-matrix composites has been on the forefront of UAM research. The resultant smart composites could be expanded to developing a system capable of structural health monitoring or be used to create components in adaptive structures. Previous research in the creation of metal-matrix composites using UAM can be broken into two categories: composites with the focus on changing material properties of the matrix material and composites with the focus on sensing.

The simplest smart metal-matrix composites are composites with embedded fibers or ribbons to increase the matrix material's stiffness or strength, similar to the idea of concrete and rebar. Embedding strong fibers in an aluminum matrix can greatly increase the strength of the composite while maintaining a lightweight structure. Previous researchers have found good mechanical interlocking between the embedding fiber/ribbon, such as silicon carbide fibers, and the aluminum matrix-material via UAM [7, 38–42]. Another area of interest is creating metal-matrix composites with tunable material properties by embedding a smart material into an aluminum

matrix. A number of researchers have investigated embedding NiTi, a shape memory alloy, fibers and strips via UAM so that the stiffness of the material can be modified by activating the embedded NiTi device [36,38,43–49]. Additionally, Galfenol, a magnetostrictive material, has been embedded into an aluminum matrix to develop a composite with tunable natural frequencies [48,50].

Concurrent to embedding fibers and smart materials to modify material properties of a composite, researchers have developed composites with embedded sensing technology. A majority of which is embedding different types of optical fibers. In [38,51], basic optical fibers were embedded in a metal-matrix and remained functional, however, the stress-strain capabilities were not evaluated. In order to monitor the stress-strain of the matrix, fiber Bragg grating arrays were embedded in aluminum matrices via UAM [52–55]. The fiber Bragg grating arrays were sensitive to various types of matrix loading (temperature, bending, etc.), and their strain measurements matched well with strain gauges during experimental testing. A new optical fiber technology called high-definition fiber optic sensing was embedded in an aluminum bracket for loading tests [56]. This technology demonstrated a good match during loading with digital image correlation strain calculations. Additionally, thermocouples have been embedded in UAM metal-matrix composites with the goal of monitoring the temperature of the structure during welding, [57], and others with the goal of monitoring the structure after embedding, [58]. The common thread in all these studies is that the composites are developed with the purpose being structural health monitoring.

Little research has been performed on developing composites with the capability of detecting the structure’s interaction with its environment, such as contact with an external object. To the author’s knowledge, only one such avenue has been previously explored in [59]. A PVDF phase sensor was embedded in an aluminum matrix via UAM and was dynamically loaded, without impact, with a solenoid actuator. They found that the sensor output was highly dependent upon the solenoid actuation frequency, but that adding an amplifying and filtering circuit to the PVDF sensor output could change the frequency response to be more broadband.

1.3 Motivation

The critical height-to-width ratio is the main limiting factor for UAM as a commercial additive manufacturing technique. The current methodology to bypass this issue is to initially build a wider substrate such that this ratio is not reached, and then machine the substrate down to the dimensions of the desired part. This method introduces issues in that it produces excess waste material from the additional machining of the final part and reduces efficiency since more layers must be bonded to maintain dimensions outside of the critical height-to-width ratio. Development of a dynamic model of the substrate is essential to understanding and finding a solution to this obstacle. Previous dynamic models ignore higher-order modes or do not fully capture the change in dynamics during the entire weld cycle. Higher-order modes are thought to play an impact at heights greater than the critical height-to-width ratio. Additionally, understanding the changing dynamics as the sonotrode traverses the substrate length during a weld cycle may provide researchers/engineers the knowledge to design an intelligent tool path to avoid regions of problematic dynamic compliance. Along with modeling the process, much of UAM research is focused on designing smart material composites. Previous embedded sensors are mainly focused on structural health monitoring, and traditionally the sensors are expensive, brittle, or require specialized instruments to measure the sensor output. The goal of this research was to develop a multi-modal model to explore the effect of the dynamic interaction between the substrate and sonotrode on the substrate modes of vibration during the entire weld cycle, and to develop an inexpensive, flexible embedded sensor in a metal-matrix via UAM that is capable of detecting contact or impact to the metal-matrix composite.

1.4 Thesis Outline

The remainder of this thesis is organized as follows:

In **Chapter 2**, a substrate model is derived with an applied moving line load to approximate the interfacial friction and applied load between the foil and the substrate

due to sonotrode compression and transverse vibration. The model derivation begins with the development of the governing equation for the system in section 2.2. Next, the free vibration solution is determined in section 2.3, and the forced vibration in section 2.4. In section 2.5, three forcing models are presented to approximate the interfacial friction for varying magnitude of foil-substrate differential motion.

In **Chapter 3**, the results for the developed model from Chapter 2 are presented. In section 3.2, convergence of the free vibration solution is demonstrated, and resonances near critical substrate heights are investigated. The model results are then compared to previous experimental results in section 3.3. In section 3.4, the substrate responses from section 3.3 are analyzed to understand the response variance during a weld cycle and with changes in height. In section 3.5, the response is studied versus a wide range of substrate heights, or height-to-width ratios, to investigate trends and predict problematic heights.

In **Chapter 4**, the design and testing of an embedded contact/impact sensor in an AL3003 metal-matrix is presented. Triboelectric nanogenerators, a new sensor technology, are introduced briefly in Section 4.2. The development of the embedded sensors and metal-matrix designs are presented in Section 4.3. In Section 4.4, the fabrication process of the smart metal-matrix composites are shown. Finally, in Section 4.5 the various testing methods are used to determine the efficacy of triboelectric nanogenerators as embedded contact/impact sensors.

In **Chapter 5**, the findings of this research project are summarized and contributions to potential applications are presented. Additionally, future work is discussed to demonstrate or provide ideas on areas of improvement based on the current work.

2. UAM MODELING DERIVATION

2.1 Introduction

The critical height-to-width ratio in UAM necessitates studying the dynamic interaction between the substrate and sonotrode. Several researchers have previously studied the dynamics of the substrate by developing models of the UAM process. It is currently theorized that resonant interactions between the substrate and the applied dynamic loading of the sonotrode reduce the differential motion between foil and substrate thus leading to bond degradation. However, previous models have ignored higher-order modes or do not take into account the dynamics of the entire weld cycle. Addressing these deficiencies could provide some insights on potential solutions to overcoming the critical height-to-width ratio. In order to study the dynamic interaction, we have developed a semi-analytical multi-modal model of the substrate to characterize the response to an approximated foil-substrate interfacial friction induced by sonotrode compression and transverse vibration. In approximating the interfacial friction, it is assumed that there is no slipping between foil and sonotrode, and thus the foil transverse motion is equivalent to the sonotrode vibration. In this chapter, first the governing equation of the developed model is presented. Next, the free and forced vibration solutions are derived. Finally, we present three different models of the approximate time-varying friction between the foil and substrate: pure stick, pure slip, and partial slip.

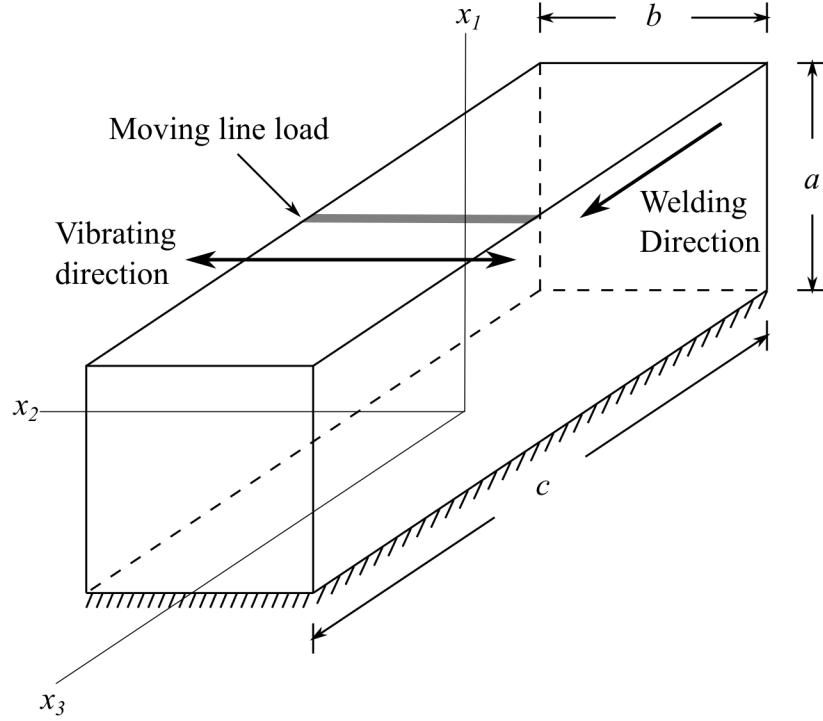


Figure 2.1. Schematic of the 3-D parallelepiped UAM model with dimensions $a \times b \times c$ subjected to a moving line load.

2.2 Governing Equation

The classic elastodynamic equation that governs the motion of a rectangular parallelepiped, i.e. the substrate, can be written in the following general form

$$c_t^2 \nabla^2 \mathbf{u} + (c_l^2 - c_t^2) \nabla (\nabla \cdot \mathbf{u}) + \frac{\mathbf{f}}{\rho} = \frac{\partial^2 \mathbf{u}}{\partial t^2}. \quad (2.1)$$

The parallelepiped has dimensions $a \times b \times c$, where a is the height, b is the width, and c is the length of the substrate. The unit vectors in the x_i , $i = 1, 2, 3$ coordinate directions are denoted as $\hat{\mathbf{e}}_i$, $i = 1, 2, 3$, allowing the displacement vector to be written as $\mathbf{u} = u_1 \hat{\mathbf{e}}_1 + u_2 \hat{\mathbf{e}}_2 + u_3 \hat{\mathbf{e}}_3$. The force per unit volume is defined as $\mathbf{f} = f_1 \hat{\mathbf{e}}_1 + f_2 \hat{\mathbf{e}}_2 + f_3 \hat{\mathbf{e}}_3$. Both the displacements and the forces are assumed to be functions of the coordinate directions and time. Respectively, they can be written as $u_i =$

$u_i(x_1, x_2, x_3, t)$, and $f_i = f_i(x_1, x_2, x_3, t)$, $i = 1, 2, 3$. The symbols $c_t = \sqrt{G/\rho}$ denote the transverse wave speed, $c_l = \sqrt{(\lambda + 2G)/\rho}$ is the longitudinal wave speed, ρ is the density of the material, λ and G are the Lamé constants, and ∇ represents the del operator $\nabla \equiv \left(\frac{\partial}{\partial x_1} \hat{i} + \frac{\partial}{\partial x_2} \hat{j} + \frac{\partial}{\partial x_3} \hat{k} \right)$.

The bottom face of the parallepiped is fixed and the Dirichlet boundary conditions can be written as

$$u_i(0, x_2, x_3, t) = 0, \quad i = 1, 2, 3 \quad \forall t. \quad (2.2)$$

In the free vibration problem the remaining surfaces are stress free. In simulating the UAM process, the force \mathbf{f} will represent the normal load due to the sonotrode compression and the dynamic interfacial friction between the foil and substrate caused by the excitation of the sonotrode.

2.3 Free Vibration

While exact analytical solutions of a free parallepiped have been developed [60], there are no corresponding solutions for a parallepiped with one surface fixed. Previous researchers have employed numerical methods in determining approximate natural frequencies and mode shapes [17, 61]. However, the current work diverges in that we seek to determine an approximate solution using a Galerkin approximation. The process begins by converting Equation (2.1) from the strong form into the weak form. Equation (2.1) can be rewritten as

$$\nabla \cdot \boldsymbol{\sigma} + \mathbf{f} = \rho \frac{\partial^2 \mathbf{u}}{\partial t^2}, \quad (2.3)$$

where the $\boldsymbol{\sigma}$ is the stress tensor. The constitutive relationship can be written as

$$\boldsymbol{\sigma} = 2G\boldsymbol{\epsilon} + \lambda(\nabla \cdot \mathbf{u})\mathbf{I}, \quad (2.4)$$

where \mathbf{I} is the second order identity tensor. The strain tensor can be written in terms of the displacement as

$$\boldsymbol{\epsilon} = \frac{1}{2} (\nabla \mathbf{u} + \nabla \mathbf{u}^T). \quad (2.5)$$

The governing equation now takes the form

$$\nabla \cdot [G (\nabla \mathbf{u} + \nabla \mathbf{u}^T) + \lambda (\nabla \cdot \mathbf{u}) \mathbf{I}] + \mathbf{f} = \rho \frac{\partial^2 \mathbf{u}}{\partial t^2}. \quad (2.6)$$

Letting $\mathbf{u} = \tilde{\mathbf{u}} e^{i\omega t}$ where ω is the natural frequency of the response, and setting $\mathbf{f} = \mathbf{0}$ yields

$$\nabla \cdot [G (\nabla \tilde{\mathbf{u}} + \nabla \tilde{\mathbf{u}}^T) + \lambda (\nabla \cdot \tilde{\mathbf{u}}) \mathbf{I}] = -\rho \omega^2 \tilde{\mathbf{u}}. \quad (2.7)$$

Multiplying the governing equation by a trial vector \mathbf{w} and integrating over the domain $\Gamma = [0, a] \times [-b/2, b/2] \times [-c/2, c/2]$ yields

$$\int_{\Gamma} \mathbf{w} \cdot (\nabla \cdot [G (\nabla \tilde{\mathbf{u}} + \nabla \tilde{\mathbf{u}}^T) + \lambda (\nabla \cdot \tilde{\mathbf{u}}) \mathbf{I}]) d\Gamma = -\rho \omega^2 \int_{\Gamma} \mathbf{w} \cdot \tilde{\mathbf{u}} d\Gamma. \quad (2.8)$$

Applying Green's Theorem

$$\int_{\Gamma} \mathbf{w} \cdot (\nabla \cdot \boldsymbol{\sigma}) d\Gamma = f, \quad (2.9)$$

and the final weak form of Equation (2.9) can be written as

$$\begin{aligned} \int_{\Gamma} \frac{G}{2} (\nabla \tilde{\mathbf{u}} + \nabla \tilde{\mathbf{u}}^T) \cdot (\nabla \mathbf{w} + \nabla \mathbf{w}^T) d\Gamma + \int_{\Gamma} \lambda (\nabla \cdot \tilde{\mathbf{u}}) (\nabla \cdot \mathbf{w}) d\Gamma = \\ -\rho \omega^2 \int_{\Gamma} \mathbf{w} \cdot \tilde{\mathbf{u}} d\Gamma, \end{aligned} \quad (2.10)$$

and rearranged to form the residual

$$\begin{aligned} R = \int_{\Gamma} \frac{G}{2} (\nabla \tilde{\mathbf{u}} + \nabla \tilde{\mathbf{u}}^T) \cdot (\nabla \mathbf{w} + \nabla \mathbf{w}^T) d\Gamma + \int_{\Gamma} \lambda (\nabla \cdot \tilde{\mathbf{u}}) (\nabla \cdot \mathbf{w}) d\Gamma + \\ \rho \omega^2 \int_{\Gamma} \mathbf{w} \cdot \tilde{\mathbf{u}} d\Gamma = 0. \end{aligned} \quad (2.11)$$

We set the vector of the trial functions equal to the approximate displacement vectors

$$\mathbf{w} = \tilde{\mathbf{u}} = \bar{\mathbf{u}}_1 \hat{\mathbf{e}}_1 + \bar{\mathbf{u}}_2 \hat{\mathbf{e}}_2 + \bar{\mathbf{u}}_3 \hat{\mathbf{e}}_3, \quad (2.12)$$

where the displacements are assumed to be of the form [17]

$$\begin{aligned} \bar{\mathbf{u}}_1 &= \sum_{i=1}^I \sum_{j=0}^J \sum_{k=0}^K A_{ijk} \hat{P}_i(\alpha) P_j(\eta) P_k(\zeta), \\ \bar{\mathbf{u}}_2 &= \sum_{l=1}^L \sum_{m=0}^M \sum_{n=0}^N B_{lmn} \hat{P}_l(\alpha) P_m(\eta) P_n(\zeta), \\ \bar{\mathbf{u}}_3 &= \sum_{p=1}^P \sum_{q=0}^Q \sum_{r=0}^R C_{pqr} \hat{P}_p(\alpha) P_q(\eta) P_r(\zeta), \end{aligned} \quad (2.13)$$

where A_{ijk} , B_{lmn} , C_{pqr} are unknown coefficients. Dimensional normalization to coordinate directions in the form of $\alpha = \frac{x_1}{a}$, $\eta = \frac{2x_2}{b}$, $\zeta = \frac{2x_3}{c}$ was applied to the polynomials in Equation (2.13). The polynomials \hat{P}_κ for $\kappa = i, l, p$ are on the interval $[0, 1]$ and generated by the Gram-Schmidt process. The polynomials P_κ for $\kappa = j, k$, $\kappa = m, n$ and $\kappa = q, r$ are the Legendre Polynomials on the interval $[-1, 1]$. The full details of determining the orthogonal basis polynomials can be found in [17].

The resulting polynomials satisfy the orthogonal condition

$$\int_0^1 \hat{P}_i(\alpha) \hat{P}_j(\alpha) d\alpha = \frac{1}{2j+1} \delta_{ij}. \quad (2.14)$$

Furthermore, this choice of polynomials automatically satisfies Equation (2.2) since the summation on \hat{P}_κ for $\kappa = i, l, p$ begins at one, while the other coordinates begin with zero. The Legendre Polynomials satisfy the orthogonal condition

$$\int_{-1}^1 P_i(\tau) P_j(\tau) d\tau = \frac{2}{2j+1} \delta_{ij}, \quad \tau = \eta, \zeta. \quad (2.15)$$

Minimizing the residual of the rectangular parallelepiped yields

$$\delta R = \frac{\partial R}{\partial A_{ijk}} \delta A_{ijk} + \frac{\partial R}{\partial B_{lmn}} \delta B_{lmn} + \frac{\partial R}{\partial C_{pqr}} \delta C_{pqr} = 0. \quad (2.16)$$

Equation (2.16) must be true for all arbitrary variations δA_{ijk} , δB_{lmn} , and δC_{pqr} . This implies that the following is true

$$\frac{\partial R}{\partial A_{ijk}} = 0, \quad \frac{\partial R}{\partial B_{lmn}} = 0, \quad \text{and} \quad \frac{\partial R}{\partial C_{pqr}} = 0, \quad (2.17)$$

and leads to the homogeneous equation of motion

$$(\mathbf{K} - \omega^2 \mathbf{M}) \boldsymbol{\phi} = \mathbf{0}, \quad (2.18)$$

where \mathbf{K} , \mathbf{M} , $\boldsymbol{\phi}$, and ω^2 are the stiffness matrix, mass matrix, eigenvectors, and eigenvalues, respectively. Equation 2.18 yields a set of $I(J+1)(K+1) + L(M+1)(N+1) + P(Q+1)(R+1)$ equations. We seek a nontrivial solution of this system by setting the determinant of the coefficient matrix to zero to find the eigenvalues and eigenvectors. The eigenvectors and eigenvalues in turn yield natural frequencies and mode shapes.

2.3.1 Orthogonality of the Approximate Mode Shapes

The eigenvectors are now used as coefficients of the polynomial functions resulting in the approximate mode shapes of the parallelepiped. The resulting mode shapes from the Galerkin approximation satisfy orthogonalization.

2.4 Forced Vibration

The process to develop a semi-analytical model continues with solving for the forced response using modal decomposition by following the process from [60]. The forced vibration solution is assumed to be of the form

$$\mathbf{u} = \sum_{\Theta} \bar{\phi}_{\theta} T_{\theta}(t), \quad (2.19)$$

where $\bar{\phi}_{\theta}$ is the mode θ vector of trial functions from $\tilde{\mathbf{u}}$ in Equation (2.12) and Equation (2.13), and $T_{\theta}(t)$ is the unknown time-varying modal response. Using the assumed free vibration solution, $\mathbf{u} = \tilde{\mathbf{u}}e^{i\omega t}$, and the assumed forced response, the governing equation from Equation (2.1) can be rewritten as

$$\sum_{\Theta} \bar{\phi}_{\theta} (\ddot{T}_{\theta} + \omega_{\theta}^2 T_{\theta}) = \frac{\bar{\mathbf{f}}}{\rho}. \quad (2.20)$$

The friction force to approximate the interfacial motion between foil and substrate is implemented as a moving line load of the form

$$\bar{\mathbf{f}} = (f_1 \hat{\mathbf{e}}_1 + f_2 \hat{\mathbf{e}}_2 + f_3 \hat{\mathbf{e}}_3) \frac{1}{a} \delta \left(\alpha - 1 \right) \frac{2}{c} \delta \left(\zeta - \frac{2}{c} \left(z_0 - st \right) \right), \quad (2.21)$$

where f_1 is the applied normal force, f_2 is the vibratory shear force caused by sonotrode excitation, f_3 is the vibratory shear force caused by sonotrode rolling and excitation, z_0 is the initial moving line load offset, and s is the speed of the moving line load. Note that f_1, f_2, f_3 are line loads with dimensions lbf/in.

An actual metal substrate created with UAM is damped so we apply modal damping, λ_d , to the model, and thus Equation (2.20) can be rewritten as

$$\sum_{\Theta} \bar{\phi}_{\theta} (\ddot{T}_{\theta} + 2\lambda_d \omega_{\theta} \dot{T}_{\theta} + \omega_{\theta}^2 T_{\theta}) = \frac{\bar{\mathbf{f}}}{\rho}. \quad (2.22)$$

In order to perform modal decomposition, the scalar product of the coupled equation of motion from Equation (2.22) and $\bar{\phi}_{\theta^*}$ is integrated over the spatial domain to form

$$\sum_{\Theta} (\ddot{T}_{\theta} + 2\lambda_d \omega_{\theta} \dot{T}_{\theta} + \omega_{\theta}^2 T_{\theta}) \int_{\Gamma^*} \bar{\phi}_{\theta} \cdot \bar{\phi}_{\theta^*} J^* d\Gamma^* = \int_{\Gamma^*} \frac{\bar{\mathbf{f}}}{\rho} \cdot \bar{\phi}_{\theta^*} J^* d\Gamma^*, \quad (2.23)$$

where J^* represents the Jacobian that is equal to $abc/4$ and Γ^* is the nondimensionalized differential volume that is equal to $d\alpha d\eta d\zeta$. Due to the orthogonality conditions of the mode shapes, Equation (2.23) can be written as a set of Θ modally-decoupled equations of motion

$$\ddot{T}_{\theta} + 2\lambda_d \omega_{\theta} \dot{T}_{\theta} + \omega_{\theta}^2 T_{\theta} = Q_{\theta}, \quad (2.24)$$

where

$$Q_{\theta} = \frac{1}{\rho E_{\theta}} \int_{\Gamma^*} \bar{\mathbf{f}} \cdot \bar{\phi}_{\theta} J^* d\Gamma^*, \quad \text{and} \quad E_{\theta} = \int_{\Gamma^*} \bar{\phi}_{\theta} \cdot \bar{\phi}_{\theta} J^* d\Gamma^*. \quad (2.25)$$

Applying the definitions from Equation (2.14) and Equation (2.15), E_{θ} from Equation (2.25) can be rewritten as

$$E_{\theta} = J^* \left[A_{ijk}^2 \left(\frac{1}{2i+1} \right) \left(\frac{2}{2j+1} \right) \left(\frac{2}{2k+1} \right) + B_{lmn}^2 \left(\frac{1}{2l+1} \right) \left(\frac{2}{2m+1} \right) \left(\frac{2}{2n+1} \right) + C_{pqr}^2 \left(\frac{1}{2p+1} \right) \left(\frac{2}{2q+1} \right) \left(\frac{2}{2r+1} \right) \right]. \quad (2.26)$$

The friction force, $\bar{\mathbf{f}}$, contains terms that are caused by the sonotrode excitation. Thus, nondimensional time in the form of $\tau = \Omega t$, where Ω is the sonotrode excitation frequency, is applied to the modally-decoupled equations of motion from Equation (2.24) and can be written as

$$T_{\theta}'' + 2\lambda_d \frac{\omega_{\theta}}{\Omega} T_{\theta}' + \frac{\omega_{\theta}^2}{\Omega^2} T_{\theta} = Q_{\theta}, \quad (2.27)$$

where

$$Q_{\theta} = \frac{1}{\rho \Omega^2 E_{\theta}} \int_{\Gamma^*} \bar{\mathbf{f}} \cdot \bar{\phi}_{\theta} J^* d\Gamma^*, \quad \text{and} \quad E_{\theta} = \int_{\Gamma^*} \bar{\phi}_{\theta} \cdot \bar{\phi}_{\theta} J^* d\Gamma^*. \quad (2.28)$$

Applying time nondimensionalization to the moving line load from Equation (2.21) changes it to

$$\bar{\mathbf{f}} = (f_1 \hat{\mathbf{e}}_1 + f_2 \hat{\mathbf{e}}_2 + f_3 \hat{\mathbf{e}}_3) \frac{1}{a} \delta\left(\alpha - 1\right) \frac{2}{c} \delta\left(\zeta - \frac{2}{c}\left(z_0 - \frac{s}{\Omega}\tau\right)\right). \quad (2.29)$$

An analytical solution is derived from Equation (2.27) and Equation (2.28) using convolution as follows

$$\begin{aligned} T_\theta(\tau) = & \int_0^\tau Q_\theta(\gamma) \frac{\Omega}{\omega_{d,\theta}} e^{-\lambda_d \frac{\omega_\theta}{\Omega}(\tau-\gamma)} \sin\left(\frac{\omega_{d,\theta}}{\Omega}(\tau-\gamma)\right) d\gamma + \\ & e^{-\lambda_d \frac{\omega_\theta}{\Omega}\tau} \left(\cos\left(\frac{\omega_{d,\theta}}{\Omega}\tau\right) + \frac{\lambda_d \omega_\theta}{\omega_{d,\theta}} \sin\left(\frac{\omega_{d,\theta}}{\Omega}\tau\right) \right) T_\theta(0) + \\ & \frac{\Omega}{\omega_{d,\theta}} e^{-\lambda_d \frac{\omega_\theta}{\Omega}\tau} \sin\left(\frac{\omega_{d,\theta}}{\Omega}\tau\right) T'_\theta(0), \end{aligned} \quad (2.30)$$

where γ is a dummy variable to perform the convolution, and $\omega_{d,\theta}$ is the damped natural frequency. After solving for $T_\theta(\tau)$, the solution is converted back into dimensional time t . Next, the modal response is inserted back into Equation 2.19 to finally solve for the response of the substrate.

2.5 Forcing Models

Three forcing models of the applied line load are developed: pure stick, pure slip, and partial slip. The forcing models are developed to study various approximations of the differential motion between the foil and substrate and their resulting dynamic interfacial friction. In developing the forcing descriptions, a dry friction model is assumed for all interfacial friction.

Pure stick forcing is approximating the dynamic friction force between the foil and substrate when there is no foil-substrate differential motion, i.e. pure stick. This is the lower limit on differential motion between the foil and substrate. To approximate the lack of differential motion between foil and substrate, the transverse vibratory shear force, f_2 , on the substrate has a sinusoidal waveform matching the sonotrode excitation waveform due to the no-slip assumption between foil and

sonotrode. This description of pure stick forcing is very similar to the forcing model developed in [17].

Pure slip forcing is approximating the dynamic interfacial friction force between the foil and substrate when the foil-substrate differential motion is equal to the sonotrode transverse vibration velocity. This is likely the upper limit on the differential motion between the foil and substrate. To approximate the pure slip behavior, the transverse vibratory shear force, f_2 , on the substrate has a nonsinusoidal waveform, similar to a square wave [62]. This definition of the pure slip forcing also includes a dynamic friction term in the longitudinal direction, f_3 , which has been theorized to exist in the UAM process due to the foil-substrate differential motion and rolling of the sonotrode [62].

Partial slip forcing is approximating the dynamic friction force between the substrate and foil when the foil-substrate differential motion is characterized by a combination of stick and slip behavior. Previous researchers have postulated that the actual behavior of the foil and substrate during the UAM process is stick-slip [17, 34–36]. To approximate the partial slip behavior, the transverse vibratory shear force, f_2 , on the substrate is developed as a clipped sine wave.

2.5.1 Pure Stick Forcing Model Definition

In pure stick forcing, line load components from Equation (2.29) take the form

$$\begin{aligned} f_1 &= -F_p, \\ f_2 &= \mu F_p \sin \tau, \end{aligned} \tag{2.31}$$

where μ is an approximate coefficient of friction and F_p is the sonotrode applied load. Applying the definition of pure stick forcing to Equation (2.29) results in

$$\bar{\mathbf{f}} = (-F_p \hat{\mathbf{e}}_1 + \mu F_p \sin \tau \hat{\mathbf{e}}_2) \frac{1}{a} \delta \left(\alpha - 1 \right) \frac{2}{c} \delta \left(\zeta - \frac{2}{c} \left(z_0 - \frac{s}{\Omega} \tau \right) \right). \tag{2.32}$$

2.5.2 Pure Slip Forcing Model Definition

In pure slip forcing, the line load components from Equation (2.21) take the form

$$\begin{aligned}
 f_1 &= -F_p, \\
 f_2 &= \mu F_p \frac{\dot{x}_r(\tau)}{\sqrt{s^2 + \dot{x}_r(\tau)^2}}, \\
 f_3 &= \mu F_p \frac{s}{\sqrt{s^2 + \dot{x}_r(\tau)^2}}, \\
 \dot{x}_r(\tau) &= \Omega X_{amp} \cos(\tau),
 \end{aligned} \tag{2.33}$$

where μ is an approximate coefficient of friction and F_p is the sonotrode applied load. The relative velocity term \dot{x}_r is the approximation of the foil-substrate differential motion, where X_{amp} is equal to the sonotrode vibration amplitude. In order to analytically solve the response using convolution, seen in Equation (2.30), the forcing components for pure slip are approximated using a Fourier series of the form

$$\begin{aligned}
 f_1 &\approx F_1(\tau) = a_0, \\
 f_2 &\approx F_2(\tau) = \sum_{n_f=1}^{N_f} a_{2,n_f} \cos(n_f \tau), \\
 f_3 &\approx F_3(\tau) = \sum_{n_f=1}^{N_f} a_{3,n_f} \cos(n_f \tau),
 \end{aligned} \tag{2.34}$$

where the Fourier series coefficients are obtained by

$$a_0 = \frac{1}{2\pi} \int_{-\pi}^{\pi} f_1 d\tau, \quad a_{i,n_f} = \frac{1}{\pi} \int_{-\pi}^{\pi} f_i \cos(n_f \tau) d\tau. \tag{2.35}$$

Applying this definition of the forcing to Equation (2.29) results in

$$\bar{\mathbf{f}} = (F_1(\tau) \hat{\mathbf{e}}_1 + F_2(\tau) \hat{\mathbf{e}}_2 + F_3(\tau) \hat{\mathbf{e}}_3) \frac{1}{a} \delta\left(\alpha - 1\right) \frac{2}{c} \delta\left(\zeta - \frac{2}{c}\left(z_0 - \frac{s}{\Omega}\tau\right)\right). \tag{2.36}$$

2.5.3 Partial Slip Forcing Model Definition

In partial slip forcing, the line load components from Equation (2.21) take the form

$$\begin{aligned} f_1 &= -F_p, \\ f_2 &= \begin{cases} \mu F_p \sin(\tau), & \text{if } |\mu F_p \sin(\tau)| \leq \max F \\ \max F, & \text{if } \mu F_p \sin(\tau) \geq \max F \\ -\max F, & \text{if } \mu F_p \sin(\tau) \leq -\max F \end{cases} \end{aligned} \quad (2.37)$$

where μ is an approximate coefficient of friction, F_p is the sonotrode applied load, and $\max F$ is the approximated shear force where slipping commences. Similar to pure slip forcing, in order to analytically solve the response using convolution, seen in Equation (2.30), the forcing components for partial slip are approximated using a Fourier series of the form

$$\begin{aligned} f_1 &\approx F_1(\tau) = a_0, \\ f_2 &\approx F_2(\tau) = \sum_{n_f=1}^{N_f} b_{2,n_f} \sin(n_f \tau), \end{aligned} \quad (2.38)$$

where the Fourier series coefficients are obtained by

$$a_0 = \frac{1}{2\pi} \int_{-\pi}^{\pi} f_1 d\tau, \quad b_{2,n_f} = \frac{1}{\pi} \int_{-\pi}^{\pi} f_2 \sin(n_f \tau) d\tau. \quad (2.39)$$

Applying this definition of the forcing to Equation (2.29) results in

$$\bar{\mathbf{f}} = (F_1(\tau) \hat{\mathbf{e}}_1 + F_2(\tau) \hat{\mathbf{e}}_2) \frac{1}{a} \delta\left(\alpha - 1\right) \frac{2}{c} \delta\left(\zeta - \frac{2}{c} \left(z_0 - \frac{s}{\Omega} \tau\right)\right). \quad (2.40)$$

2.6 Summary

A model is developed of a 3-D parallelepiped with a moving line load to study the dynamics of the substrate near critical build heights. The model solution is developed by first solving the free vibration problem. Next, the modes are used to perform modal decomposition of the forced vibration problem. However, there are no known exact analytical solutions of the 3-D parallelepiped with a fixed boundary

condition [17, 61]. Thus, we utilized a Galerkin approximation to obtain the natural frequencies and mode shapes. After performing modal decomposition, the damped response was solved using convolution for three types of forcing: pure stick, pure slip, and partial slip. With the three descriptions of forcing, the model can be simulated to determine the response at critical build heights for various approximations of the foil-substrate differential motion.

3. UAM MODELING RESULTS

3.1 Introduction

Experimental results in [16] and [17] demonstrated that as the height approaches the critical height-to-width ratio ($a/b = 1$), bonding deteriorates and subsequent bonding of layers can no longer occur. However, in [17] the substrate height was continued past this limit to show that the critical height-to-width ratio was merely an obstacle, and that bonding can be reinitiated past the critical height-to-width ratio. The commonly accepted theory for the critical height-to-width ratio at the nominal tape width is that resonant interactions between the substrate and sonotrode increase the dynamic compliance of the substrate, thus causing reduced differential motion and subsequent bond degradation [17]. In studying the critical height-to-width ratio, previous dynamic models, see literature review, ignore higher-order modes or do not consider the response for the entire weld cycle. Ignoring these potentially significant dynamic impacts could cause researchers to misinterpret the results and miss potential solutions to this issue. The effect of resonant interactions between the substrate and the sonotrode is explored by a multi-step process in which we study the natural frequencies dependence on substrate height, the various forcing models prediction of substrate response, the change in substrate response during an entire weld cycle, and the change in substrate response as the height is varied. In following this process, this chapter begins with demonstrating the convergence of the free vibration solution and studying the resonance of the natural frequencies with the excitation frequency as the substrate height is varied. Following, the transverse velocity response to pure stick, pure slip, and partial slip forcing is compared to the experimental results from [17] during a weld cycle. In order to understand the trends seen in the model and experimental results, the modal contributions to the transverse velocity response and

the modal response and forcing for three selected heights are analyzed to study the change in response with respect to each mode. Finally, the transverse velocity response versus substrate height is performed to develop a prediction of problematic height-to-width ratios that result from a change in dynamic compliance as the substrate height is varied. Note, in the future analyses of this chapter the substrate height is varied to change the height-to-width ratio mimicking the UAM process in which the substrate height changes.

3.2 Free Vibration Solution

The first step of the modal study is to use the free vibration solution to investigate the possibility of resonant interactions between the substrate and the sonotrode. Specifically, this examination is to understand when resonance of the substrate occurs at a width, b , of 1 in and a length, c , of 2.5 in over a range of substrate heights. This width is chosen because in UAM the nominal tape width is 1 in (25.4 mm). The length was chosen to be consistent with previously published results [12,17]. All further analyses will be performed at these substrate width and length dimensions.

3.2.1 Convergence Analysis

The Galerkin approximation is validated by demonstrating convergence of the natural frequencies as the span of basis functions in the approximation increases. The material properties used in this analysis are summarized in Table 3.1. We assumed

Table 3.1. Material properties for AL3003 at 25C.

Parameter	Value
E	$10.6 \times 10^6 \text{ lbf/in}^2$
ν	0.33
ρ	$2.61 \times 10^{-4} \text{ lbm/in}^3$

that the material properties are not affected by the localized heating at the bonding interface. Additionally, we assumed that the material properties are equal to those of the bulk material, which was influenced by the findings of [17] where the critical height-to-width ratio phenomenon also occurs in substrates of just gross material, i.e. non-UAM built substrates. The natural frequencies are compared to the natural frequencies determined from a finite element (FE) model of the cantilevered 3-D parallelepiped in ABAQUS. For each height-dependent FE model, approximately 100,000 elements were used. From Table 3.2, we have shown that as the number of basis functions increases, the percent error between the Galerkin and FE model natural frequencies decreases. For efficiency in all future analyses, we use $I = 7$, $J = 5$, and $K = 5$ as the span of basis functions in our Galerkin approximation. With these span of basis functions, the percent difference remains below 3% and in many of the cases is below 1%. Comparing the natural frequencies from the Galerkin approximation of the model to those determined through a FE model has given confidence in the free vibration solution.

3.2.2 Substrate Resonance and Mode Shape Analysis

From the free vibration solution, the mode shapes at the critical height-to-width ratio (for our model with dimensions $a = 1$ in, $b = 1$ in, and $c = 2.5$ in) are presented in Figure 3.1. An understanding of the mode shapes at the critical height-to-width ratio provides insight on the potential dynamic interaction between foil and substrate induced by sonotrode excitation. Mode shapes that produce large transverse deflection shapes will likely have a larger impact on the reduction of differential motion between foil and substrate than mode shapes with small transverse deflection shapes.

However, the deflection shape of each mode not only affects the response, but also the response is affected by the proximity of a natural frequency to the excitation frequency. A preliminary study of the natural frequencies of the first ten modes is performed over a wide range of heights (height-to-width ratios because the width, b ,

Table 3.2. Comparison of Galerkin Approximation with Finite Element Model Natural Frequencies.

Polynomial Terms	Mode	Percent Error %			
		$a = 0.5$ in	$a = 1.0$ in	$a = 1.5$ in	$a = 2.0$ in
$I = 7, J = 3, K = 3$	1	1.7577	1.156	0.88153	0.74308
	2	1.6418	1.0613	0.84479	0.73341
	3	2.1252	1.6555	1.3214	1.0592
	4	5.5699	7.8677	7.681	0.80716
	5	3.9511	0.60096	0.46979	1.9923
	6	7.279	6.8143	0.25689	0.34047
	7	15.139	0.58096	2.0455	7.1804
	8	11.15	0.5437	1.4953	0.96812
	9	12.458	2.0416	1.9381	3.2055
	10	2.5947	4.3181	3.6111	1.8595
$I = 7, J = 5, K = 5$	1	0.46037	0.34432	0.34204	0.35571
	2	0.40524	0.25612	0.22323	0.20759
	3	0.78236	0.42841	0.34429	0.30254
	4	0.56248	0.39121	0.30532	0.23704
	5	0.84103	0.24886	0.19596	0.16761
	6	0.90856	0.50877	0.092277	0.081464
	7	2.9425	0.22708	0.19566	0.21385
	8	1.8757	0.13026	0.1241	0.20895
	9	0.46677	0.35994	0.25312	0.10879
	10	0.47717	0.34749	0.20713	0.095058
$I = 7, J = 7, K = 7$	1	0.2087	0.22263	0.27451	0.31168
	2	0.18138	0.15378	0.16347	0.16747
	3	0.3037	0.1833	0.17386	0.1876
	4	0.2063	0.1381	0.13826	0.15934
	5	0.38893	0.14499	0.12898	0.12371
	6	0.28873	0.15928	0.057705	0.042755
	7	0.47945	0.12791	0.12356	0.12193
	8	0.26776	0.088503	0.090672	0.15604
	9	0.22652	0.11519	0.15697	0.071821
	10	0.21106	0.098341	0.082125	0.060367

is kept constant at the nominal tape width of 1 in and c is kept at 2.5 in). Figure 3.2 is a plot of the natural frequencies versus height with an included line indicating

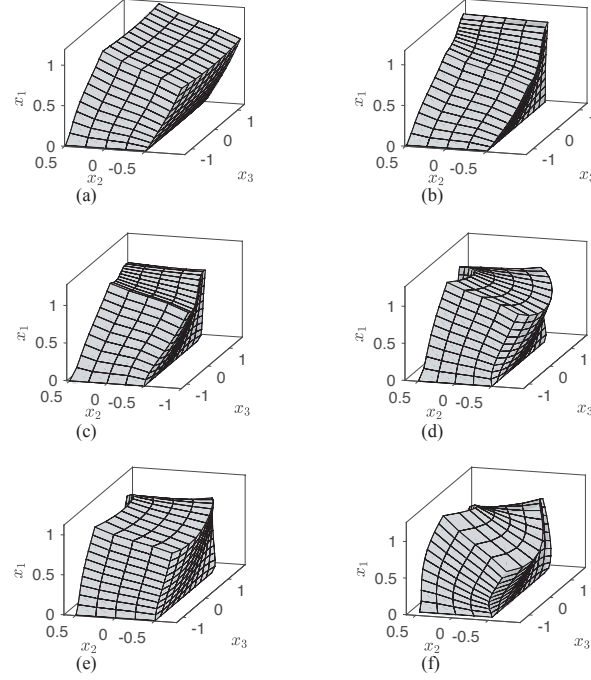


Figure 3.1. First six modeshapes of dimension $1.0 \text{ in} \times 1.0 \text{ in} \times 2.5$ (additional dimensions can be seen in Appendix A) with natural frequencies : a) $f_1 = 21863.74 \text{ Hz}$, b) $f_2 = 24990.16 \text{ Hz}$, c) $f_3 = 27524.47 \text{ Hz}$, d) $f_4 = 38661.71 \text{ Hz}$, e) $f_5 = 44142.78 \text{ Hz}$, and f) $f_6 = 53281.16 \text{ Hz}$.

the excitation frequency of the sonotrode, 20 kHz . From Figure 3.2, as the height, a , is increased to near 1 in , the natural frequency of the first mode approaches the sonotrode excitation frequency, i.e. resonance. As the height is further increased, the natural frequencies of higher-order modes also reach resonance with the sonotrode excitation frequency. We deem those heights at which a natural frequency of a mode is resonant with the sonotrode excitation frequency, a critical height. The critical heights for the first eight modes of the substrate can be seen in Table 3.3. Also at each critical height, the first eight normalized natural frequencies, normalized with respect to the sonotrode excitation frequency, are determined.

Although the free vibration solution provides information regarding resonances and the tools to determine critical heights, the effect of these resonances on the response cannot be determined solely from the free vibration solution. The current

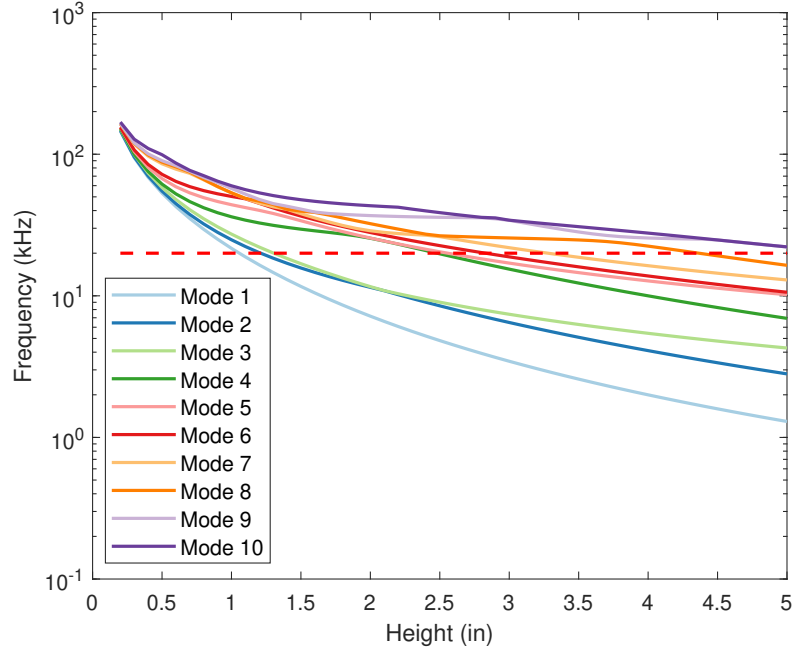


Figure 3.2. Semilog plot of first ten natural frequencies versus substrate height c . Dotted red line indicates 20 kHz operating frequency of sonotrode.

Table 3.3. Critical heights versus natural frequencies of substrate.

Critical heights	Normalized natural frequencies (ω_θ/Ω)							
	Mode 1	Mode 2	Mode 3	Mode 4	Mode 5	Mode 6	Mode 7	Mode 8
$a = 1.0559$ in	0.9999	1.1681	1.2817	1.7512	2.1424	2.4622	2.5297	2.5357
$a = 1.2101$ in	0.8162	1.0000	1.0937	1.6285	1.9977	2.2320	2.2396	2.3225
$a = 1.3046$ in	0.7269	0.9185	1.0000	1.5706	1.9038	2.0811	2.1209	2.2006
$a = 2.4802$ in	0.2449	0.4298	0.4547	0.9999	1.0312	1.1394	1.3197	1.3295
$a = 2.5571$ in	0.2317	0.4111	0.4400	0.9609	0.9999	1.1059	1.2810	1.3204
$a = 2.8292$ in	0.1924	0.3541	0.3946	0.8380	0.9032	1.0000	1.1595	1.2944
$a = 3.2786$ in	0.1460	0.2824	0.3366	0.6782	0.7785	0.8587	1.0000	1.2605
$a = 4.3654$ in	0.0843	0.1772	0.2474	0.4343	0.5835	0.6241	0.7453	0.9999

model is 3-D, and thus the resonant mode at a critical height may have a mode shape that is not greatly affected by the applied moving line load. Thus, the forced response

must be determined to fully evaluate resonant interactions between the applied moving line load and the substrate.

3.3 Transverse Velocity Response in Comparison to Experimental Results

Using the developed analytical solutions, pure stick, pure slip, and partial slip forcing descriptions are used to determine the response of the substrate for an entire weld cycle. In [17], a vibrometer was used to measure the transverse (perpendicular to weld direction) velocity response of the substrate directly underneath the sonotrode contact patch during a weld cycle for four height-to-width ratios. Therefore in the current model, the velocity response in the transverse direction (x_2) and directly underneath the moving line load ($x_1 = a, x_2 = 0, x_3 = z_0 + s t$) is recorded during the analysis. The simulation location of the model differs slightly from the measurement location of the experimental results in that the experimental results measurement location was along the side of the substrate at the top and thus would be at ($x_1 = a, x_2 = b/2, x_3 = z_0 + s t$). However, the measurement location of the model is useful because it provides information on the response of the substrate in the center of the bond interface, which can be used to deduce the foil-substrate differential motion and thus likelihood of bond degradation. The experimental results from [17] are compared to the model results for the three forcing descriptions. The goal of this study is to develop an understanding of the substrate transverse velocity response dependence on height and the variation during the weld cycle. Due to the inaccuracies in the approximated interfacial friction of the moving line load and slight differences in the measurement locations, a quantitative comparison is unlikely to provide concrete information. Therefore, a qualitative comparison of the trends in the experimental and model results is sufficient. Validation of the forced response of the model and the developed simulation script can be seen in Appendix B.

The parameters values used to study the dynamics of the substrate with respect to the three forcing models can be seen in Table 3.4, and the materials properties was previously provided in Table 3.1.

Table 3.4. Parameter values for model simulation of forced response for experimental comparison.

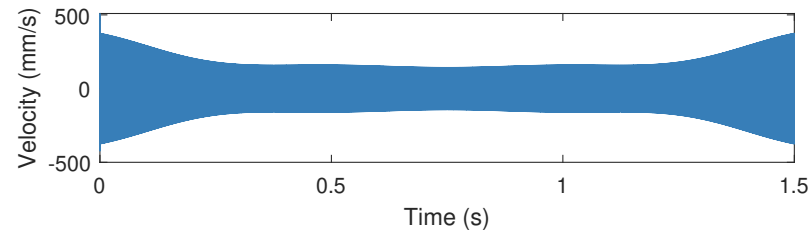
Parameters	Pure Stick	Pure Slip	Partial Slip
a	0.5, 0.75, 1, 2 in	0.5, 0.75, 1, 2 in	0.5, 0.75, 1, 2 in
b	1 in	1 in	1 in
c	2.5 in	2.5 in	2.5 in
F_p	1000 lbf/in	1000 lbf/in	1000 lbf/in
μ	0.3	0.3	0.3
Ω	$2\pi \times (20 \times 10^3)$ rad/s	$2\pi \times (20 \times 10^3)$ rad/s	$2\pi \times (20 \times 10^3)$ rad/s
s	$\frac{c}{1.5}$	$\frac{c}{1.5}$	$\frac{c}{1.5}$
z_0	$\frac{-c}{2}$	$\frac{-c}{2}$	$\frac{-c}{2}$
λ_d	0.05	0.05	0.05
maxF	N/A	N/A	250 lbf/in
X_{amp}	N/A	16 μm	N/A

The forced response was solved using a 10-mode approximation, as in the free vibration solution span was kept at $I = 7$, $J = 5$, $K = 5$, but the solution to modally-decoupled equation of motion, seen in Equation (2.27), was only for the first ten modes. For pure slip and partial slip forcing, the Fourier series approximation included 10-terms ($N_f = 10$) and 5-terms ($N_f = 5$), respectively. Additionally, the weld time or simulation time was equal to c/s which was forced to be 1.5 s. To maintain consistency, the sampling frequency for all the simulations was chosen to be 2 MHz because the 10-term Fourier series to approximate pure slip forcing introduced harmonic forcing components at 200 kHz.

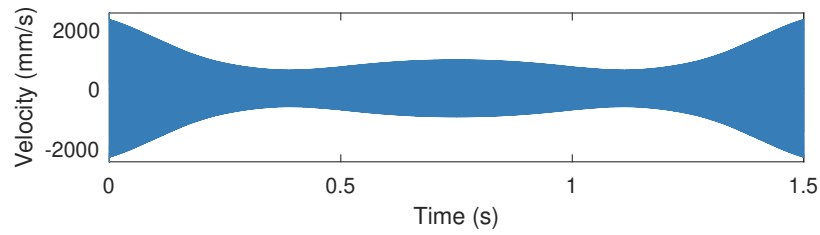
To simulate the response, a MATLAB script combined with a function containing the analytically- determined solution to Equation (2.30) for the three forcing models was developed. After analytically solving for the transverse displacement response of the substrate under the moving line load, a numerical derivative was applied to solve for the transverse velocity response.

3.3.1 Transverse Velocity Response at $a = 0.5$ in

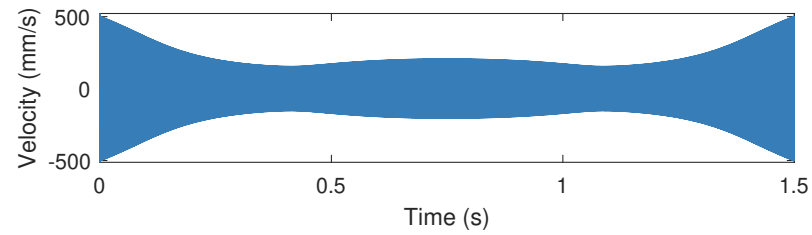
The transverse velocity response of the model is simulated at $a = 0.5$ in, which can be seen along with the experimental response in Figure 3.3. The experimental transverse velocity response includes a dwell section at the beginning of the weld cycle that was not included in the model, because a dwell section is typically not included during normal operations of current UAM machines. The transverse velocity responses to pure stick and partial slip forcing are very similar in magnitude, however, the amplitude of the partial slip forcing response is slightly larger. The transverse velocity response to pure stick forcing is much greater in magnitude than both pure slip forcing and partial slip forcing. The experimental and the model responses generally decrease in the middle of the weld cycle which indicates that the substrate is stiffer in the middle of its length as compared to the ends. However, for pure slip and partial slip forcing there is a slight increase in the transverse response amplitude in the middle of the weld cycle as the moving line load approaches the middle of the substrate's length. This increase in the middle of the weld cycle is absent in the pure stick forcing and the experimental response. The absence of the hump in the pure stick forcing response indicates that this is likely caused by multi-frequency harmonics in the approximated interfacial friction force for pure slip and partial slip.



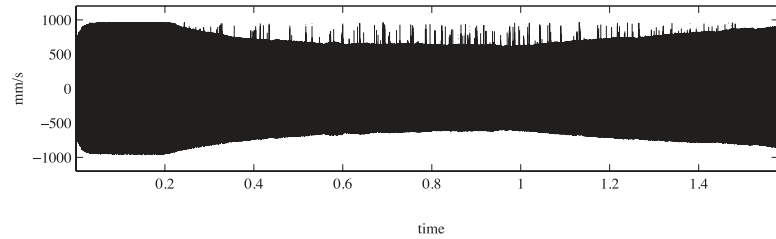
(a) Pure Stick Forcing



(b) Pure Slip Forcing



(c) Partial Slip Forcing



(d) Experimental Results [17]

Figure 3.3. Transverse velocity response directly under forcing model moving line load compared to experimental response from [17] for substrate height $a = 0.5$ in.

3.3.2 Transverse Velocity Response at $a = 0.75$ in

Next, the transverse velocity response of the model is simulated at $a = 0.75$ in, which can be seen along with the experimental response in Figure 3.4. As compared

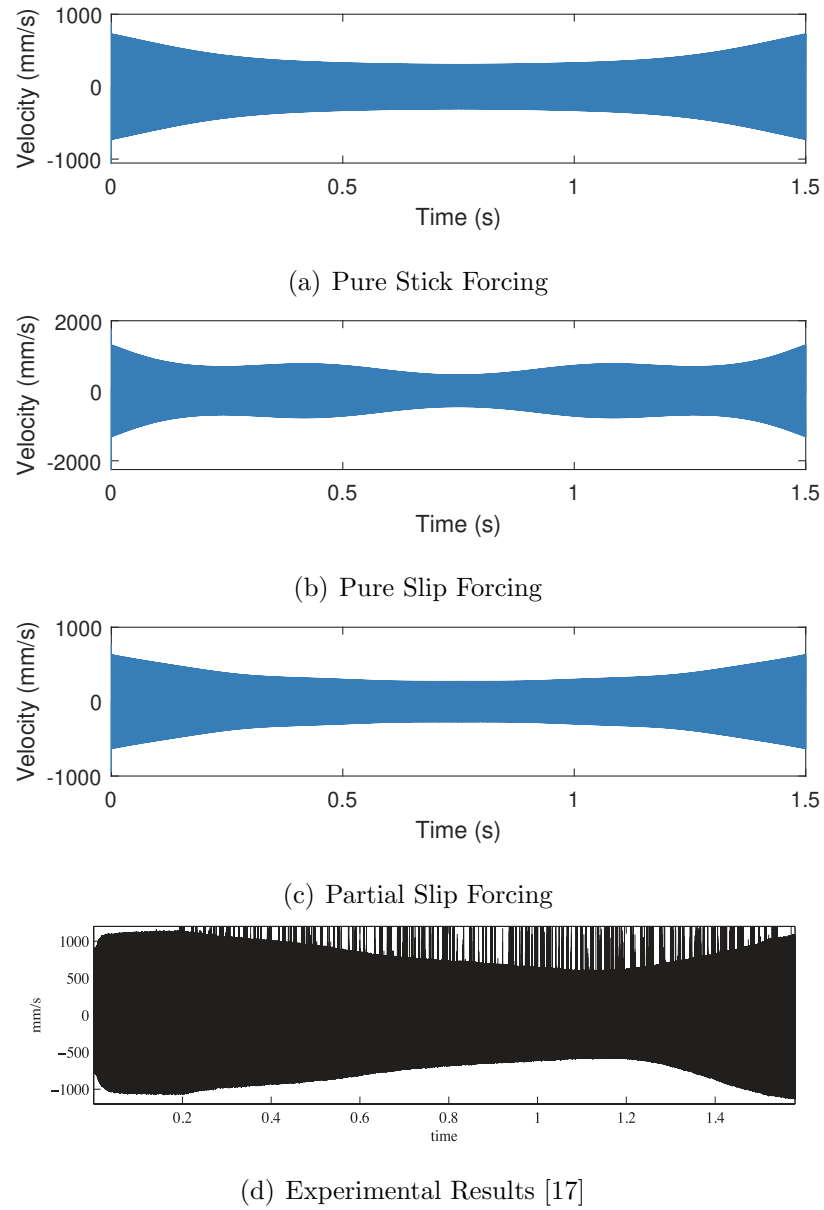


Figure 3.4. Transverse velocity response directly under forcing model moving line load compared to experimental response from [17] for substrate height $a = 0.75$ in.

to the responses at $a = 0.5$ in, the transverse velocity response amplitude increased in magnitude for pure stick, pure slip, partial slip, and for experimental results. This increase in amplitude indicates that the dynamic compliance of the substrate to the applied line load is increasing, and thus there is likely a decrease in foil-substrate differential motion. The magnitude of transverse velocity response amplitude was greater for partial slip than for pure stick forcing. Similar to Figure 3.3, the substrate is stiffer in the middle of its length. The transverse response to pure slip forcing shows a variation during the weld cycle that is not seen in the response to other forcing models. The response amplitude to pure slip forcing contains some wave-like variation during the weld cycle, which indicates some local decreases in substrate stiffness as the the moving line load traverses its length. The experimental transverse velocity response does not contain this wave-like variation in the response amplitude, but instead shows a similar shape during the weld cycle as the model response to pure stick and partial slip forcing.

3.3.3 Transverse Velocity Response at $a = 1$ in

Next, the height is increased to the critical height-to-width ratio, $a = 1$ in, and the transverse velocity response of the model simulation results can be seen along with the experimental response in Figure 3.5. Unfortunately, the power supply on the UAM machine used in [17] consistently failed at the critical height-to-width ratio, and there are no experimental measurements to compare to the model response. From the model results, the magnitude of the transverse velocity response amplitude increased drastically from the responses at $a = 0.75$ in, seen in Figure 3.4. The increase at the critical height-to-width ratio is attributed to the first natural frequency being near resonance with the excitation frequency, seen in Table 3.3. The increase in magnitude is expected, indicating an increase in the transverse dynamic compliance, which is in agreement with the bond degradation at the critical height-to-width ratio. Similar to previous heights, there is a slight decrease in the model transverse response amplitude

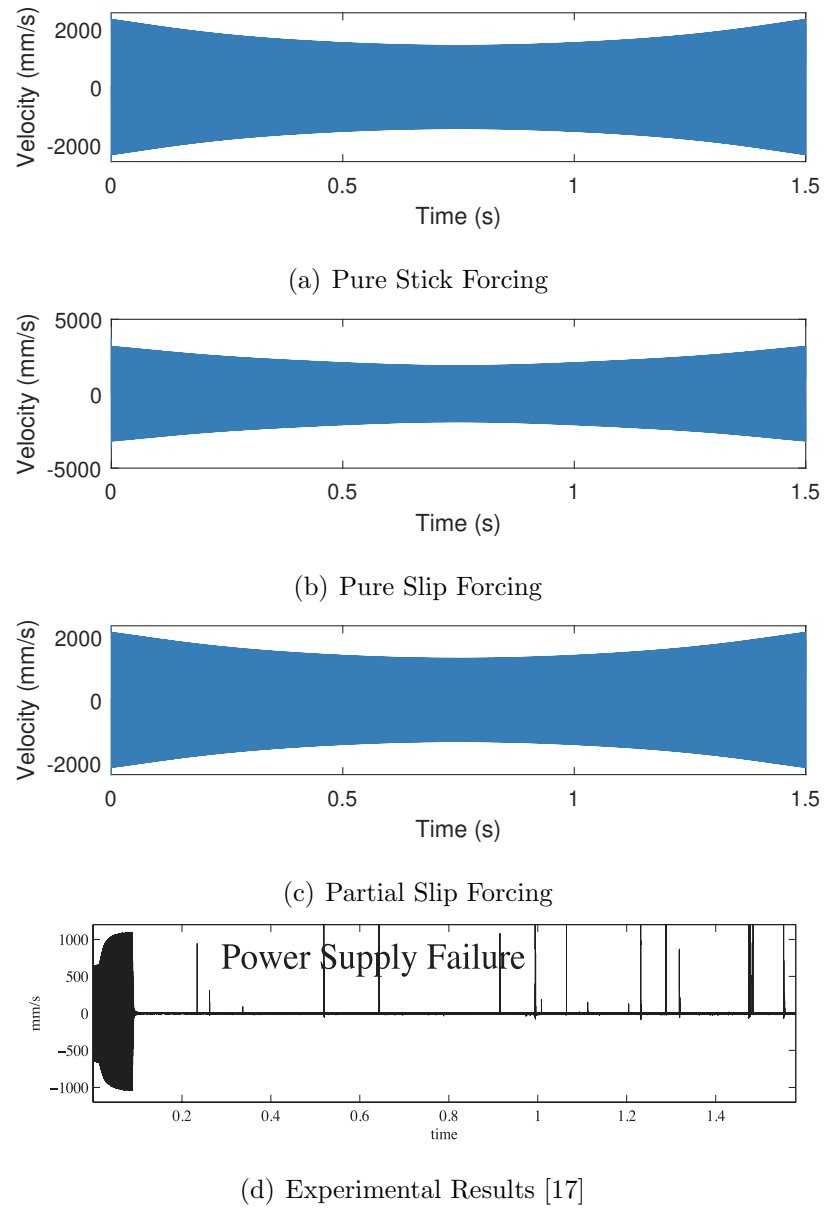


Figure 3.5. Transverse velocity response directly under forcing model moving line load compared to experimental response from [17] for substrate height $a = 1$ in (the response in [17] is for $a = 0.9375$ in).

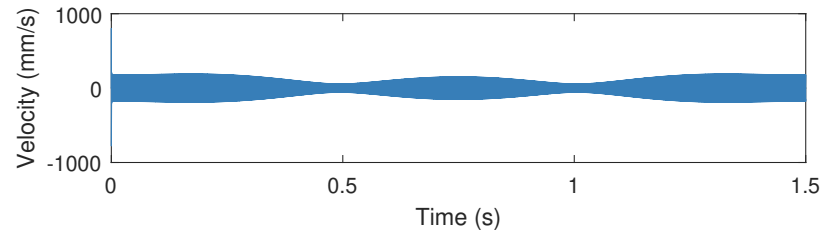
in the middle of the weld cycle indicating a local increase in substrate stiffness. The transverse velocity response to pure slip forcing is greater in magnitude than the response to pure stick forcing and partial slip forcing; however, a trend that changed from previous heights is that the transverse velocity response to pure stick forcing is greater in magnitude than the response to partial slip forcing.

3.3.4 Transverse Velocity Response at $a = 2$ in

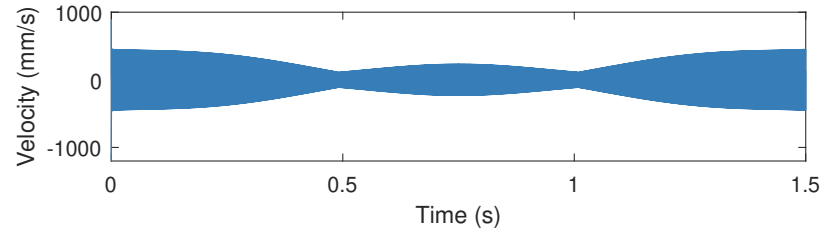
The height is further increased to $a = 2$ in, and the transverse velocity response of the model can be seen along with the experimental substrate response in Figure 3.6. As opposed to the previous trends with height increases, the transverse velocity response of the model decreased. The decrease in the transverse velocity response as compared to the critical height-to-width ratio indicates a decrease in dynamic transverse compliance. This is expected because bonding could be reinitiated at a substrate height of 2 in, which is above the critical height-to-width ratio [17]. The response from the three forcing models show a wave-like variation during the weld cycle that also occurs in the experimental response. The response to partial slip forcing is similar in magnitude to the response to pure stick forcing; however, both responses are less in magnitude than the response to pure slip forcing.

3.3.5 Transverse Velocity Response at $a = 2.5$ in

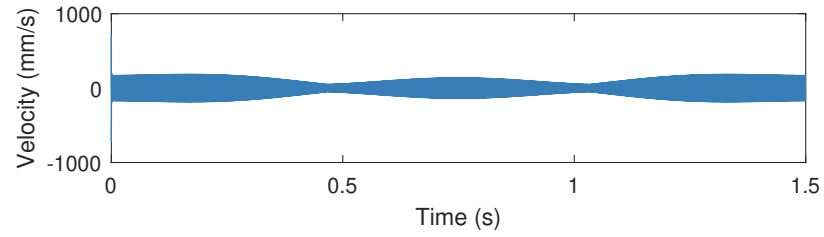
We would like to include an additional set of transverse velocity responses to pure stick, pure slip, and partial slip forcing. Although, there are no experimental results to compare to the model, we were interested in the model results at this height. The transverse velocity response at $a = 2.5$ in can be seen in Figure 3.7. The magnitude of the transverse velocity responses increased in comparison to the responses at $a = 2$ in. This can likely be attributed to a resonance with either mode 4 or mode 5, seen in Table 3.3. The trend of the transverse velocity response during the weld cycle is the same for each forcing model, with the response amplitude to pure slip forcing being



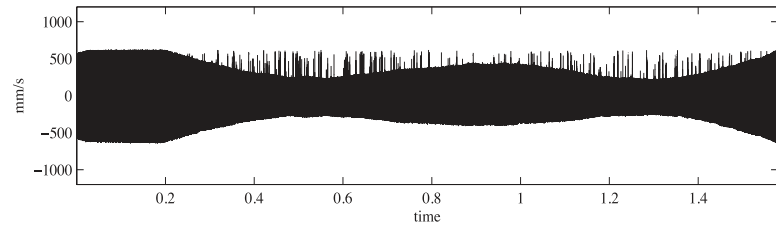
(a) Pure Stick Forcing



(b) Pure Slip Forcing

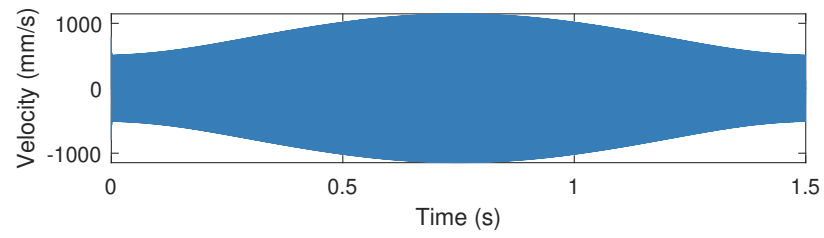


(c) Partial Slip Forcing

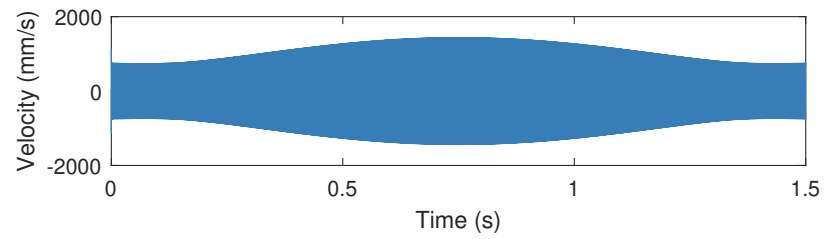


(d) Experimental Results [17]

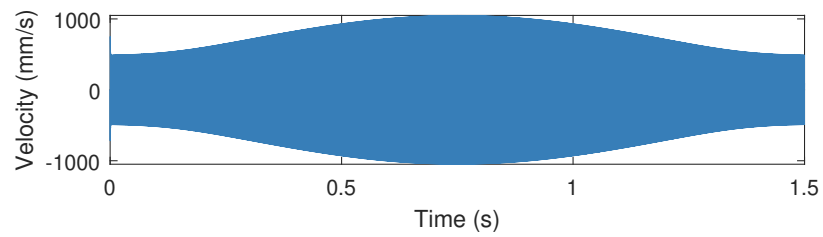
Figure 3.6. Transverse velocity response directly under forcing model moving line load compared to experimental response from [17] for substrate height $a = 2$ in.



(a) Pure Stick Forcing



(b) Pure Slip Forcing



(c) Partial Slip Forcing

Figure 3.7. Transverse velocity response directly under forcing model moving line load for substrate height $a = 2.5$ in.

the largest in magnitude. The transverse velocity response varies during the weld cycle in a manner not previously seen at any of the other heights. The transverse velocity response at $a = 2.5$ in is greatest in magnitude during the middle of the weld cycle, which indicates a decrease in the stiffness of the substrate near the middle of its length.

For the transverse velocity responses at $a = 0.5, 0.75, 1, 2,$ and 2.5 in, there is a variation in the magnitude of the response amplitude during the weld cycle as the moving line load, i.e. the sonotrode, traverses the length of the substrate. The qualitative comparisons to experimental results demonstrate that the pure stick forcing model matches the experimental trends during the weld cycle for all the heights tested, the partial slip forcing model matches the experimental trends during the weld cycle for all heights tested except at $a = 0.5$ in, and the pure slip forcing model matches the experimental trends for heights tested greater than $a = 0.75$ in. The transverse velocity response magnitude and shape during the weld cycle show a dependence upon the height of the substrate. The cause for this height dependence of the response magnitude and variance during weld cycle is currently unknown. The following section analyzes the transverse velocity response to develop an understanding of this amplitude variance during the weld cycle and variance with height.

3.4 Selective Time Traces of Response

The transverse velocity response at the experimental heights demonstrated a dependence on height and moving line load location during the weld cycle. To further study this phenomenon in the transverse velocity responses, three heights, $a = 1$ in, 2 in and 2.5 in, are chosen to analyze the response to pure stick, pure slip, and partial slip forcing in depth. These heights are chosen to demonstrate the change in response near and far from resonances since $a = 1$ in is near a resonance, $a = 2$ in is not near a resonance, and $a = 2.5$ in is near another resonance, seen in Table 3.3. The

transverse velocity responses are broken down by the contribution from the first four modes for $a = 1$ in and $a = 2$ in, and the first five modes for $a = 2.5$ in, where mode 5 is included due to the proximity of the natural frequency resonance. Performing the modal contribution analysis will indicate what mode causes the transverse velocity response dependence on height and what mode influences the transverse velocity response variation during the weld cycle. Additionally, the modal response, T_θ , and modal forcing, Q_θ , from Equation (2.30), along with the FFT and phase plot of the modal response, are determined for 1 ms of excitation beginning from $t = 0$ s and an additional 1 ms of excitation beginning from $t = 0.75$ s. These results will provide a zoomed-in view of each modal response, and indicate the influence of the modal forcing on the transverse velocity response.

3.4.1 Selective Time Traces for $a = 1$ in

The first height to be evaluated is $a = 1$ in, which is the critical height-to-width ratio for a substrate of nominal tape width.

3.4.1.1 Pure Stick Forcing

The transverse velocity response to pure stick forcing shown in Figure 3.5(a), is broken down into the modal contribution from the first four modes, seen in the first column of Figure 3.8. The transverse velocity response at $a = 1$ in to pure stick forcing is dominated by the first mode due to its near resonance with the excitation frequency. The first mode is a pure bending mode, illustrated in Figure 3.1, and thus changes in the moving line load location during the weld cycle do not greatly affect the contribution of mode 1 to the transverse velocity response. The response of the second mode varies greatly during the weld cycle, and is cut off in the middle of the weld cycle when the moving line load is in the middle of the substrate length. The second mode shape, seen in Figure 3.1, is a torsional mode and contains a node at the middle of the substrate length. The decrease in the transverse velocity response in the

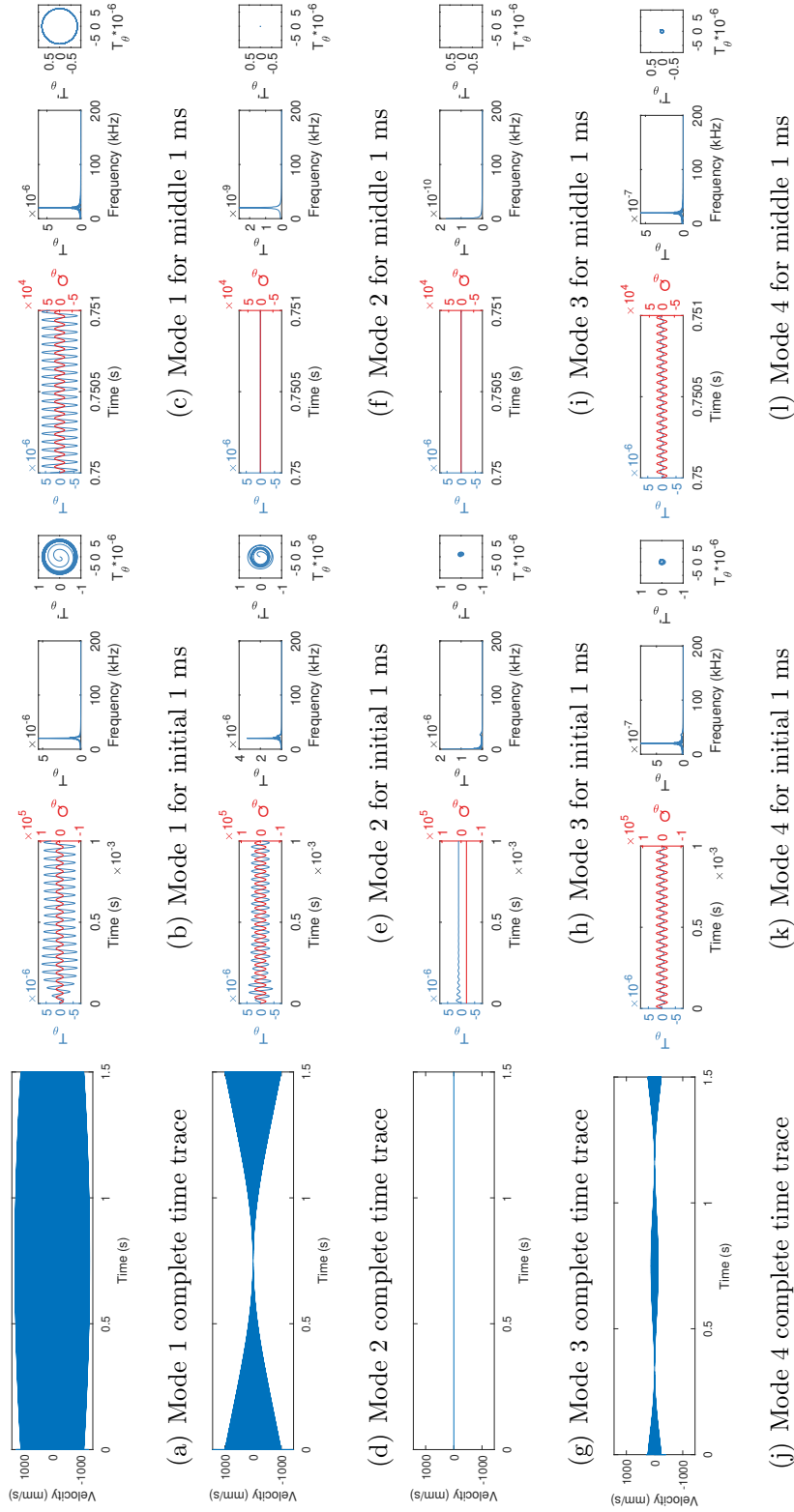


Figure 3.8. Pure stick forcing transverse velocity response for substrate height $a = 1$ in broken down. The first column is transverse velocity response modal contributions, the second column is the modal response in blue and forcing in red at $t = 0$ s, and third column is the modal response in blue and forcing in red at $t = 0.75$ s.

middle of the weld cycle is attributed to the second mode cutting off. The third mode contributes very little to the transverse velocity response during the entire weld cycle. The response from the fourth mode is insignificant to the total transverse velocity response as compared to the first and second modes. Additionally, the response of mode 4 varies during the weld cycle and appears to contain two nodes symmetric about the middle of the substrate length that results in mode 4 cutting on and off multiple times. To further study the dynamics, the modal response and forcing is analyzed and can be seen in the second and third columns of Figure 3.8. The variation of the pure stick modal responses during the weld cycle follows the same trends as the modal contributions to the transverse velocity response. For example, the transverse velocity response for mode 2 is large in magnitude at the beginning of the weld cycle and small in the middle of the weld cycle. The modal response is large at $t = 0$ s and small at $t = 0.75$ s, and thus the modal response follows the same trends as the modal contribution to the transverse velocity response during the weld cycle. However, the phase plots for the modal responses also provide information not easily observable in the modal contribution plots. For example, the modal response for mode 1 at $t = 0$ s, seen in the second column, contains transients that are damped out as indicated by the spiraling phase plot. However, by the middle of the weld cycle, seen in the third column, the modal response is a single harmonic as indicated by the circular phase plot. Similar observations can be seen in the phase plots for the additional modal responses. The modal forcing for modes 1, 2, and 4 resembles a sinusoidal waveform, and thus these modes are influenced by the f_2 forcing component. The modal forcing for mode 3 appears to be a DC offset, and thus is attributed to the normal forcing component f_1 . Therefore, the contribution of mode 3 to the transverse velocity response will be insignificant, as seen in Figure 3.8(g). On the other hand, perhaps the response for mode 3 is more complicated, and other forcing descriptions may provide some insight. From these results, the f_2 forcing component heavily influences the transverse velocity response, whereas other forcing components have a negligible effect.

3.4.1.2 Pure Slip Forcing

To continue analyzing $a = 1$ in, the transverse velocity response to pure slip forcing shown in Figure 3.5(b), is similarly broken down into the contribution from the first four modes, seen in the first column in Figure 3.9. The transverse velocity response modal contributions to pure slip forcing has the same trends during the weld cycle as the response to pure stick forcing, seen in the first column of Figure 3.8. These trends can be summarized as mode 1 is dominant and relatively invariant during the weld cycle, mode 2 contributes greatly at the beginning and end of the weld cycle, mode 3 is negligible, and mode 4 is relatively insignificant. The magnitude of the transverse velocity response to pure slip forcing is larger than that for pure stick forcing. The modal response and modal forcing variation in time to pure slip forcing is analyzed and illustrated in the second and third columns of Figure 3.9. The variation of the pure slip modal responses during the weld cycle follows the same trends as the modal contributions to the transverse velocity response for pure slip forcing during the weld cycle. Additionally, the modal response phase plots have similar trends as those for pure stick forcing, seen in the second and third columns of Figure 3.8. The modal forcing for modes 1, 2, and 4 resembles the square-wave of f_2 forcing component, which contains multiple harmonic components. The multiple harmonic components input more energy into the dominant modes, which results in the increased transverse velocity responses as compared to pure stick forcing. Mode 3 is influenced by the f_1 normal forcing component as indicated by the DC offset in the modal forcing, and the f_3 longitudinal forcing component as indicated by the impulse-like harmonic waveform in the modal forcing. Although the f_3 forcing component is observed in the modal forcing, it has a negligible effect on the total transverse velocity response.

3.4.1.3 Partial Slip Forcing

Finally for $a = 1$ in, the transverse velocity response to partial slip forcing shown in Figure 3.5(c), is broken down into the contribution from the first four modes to

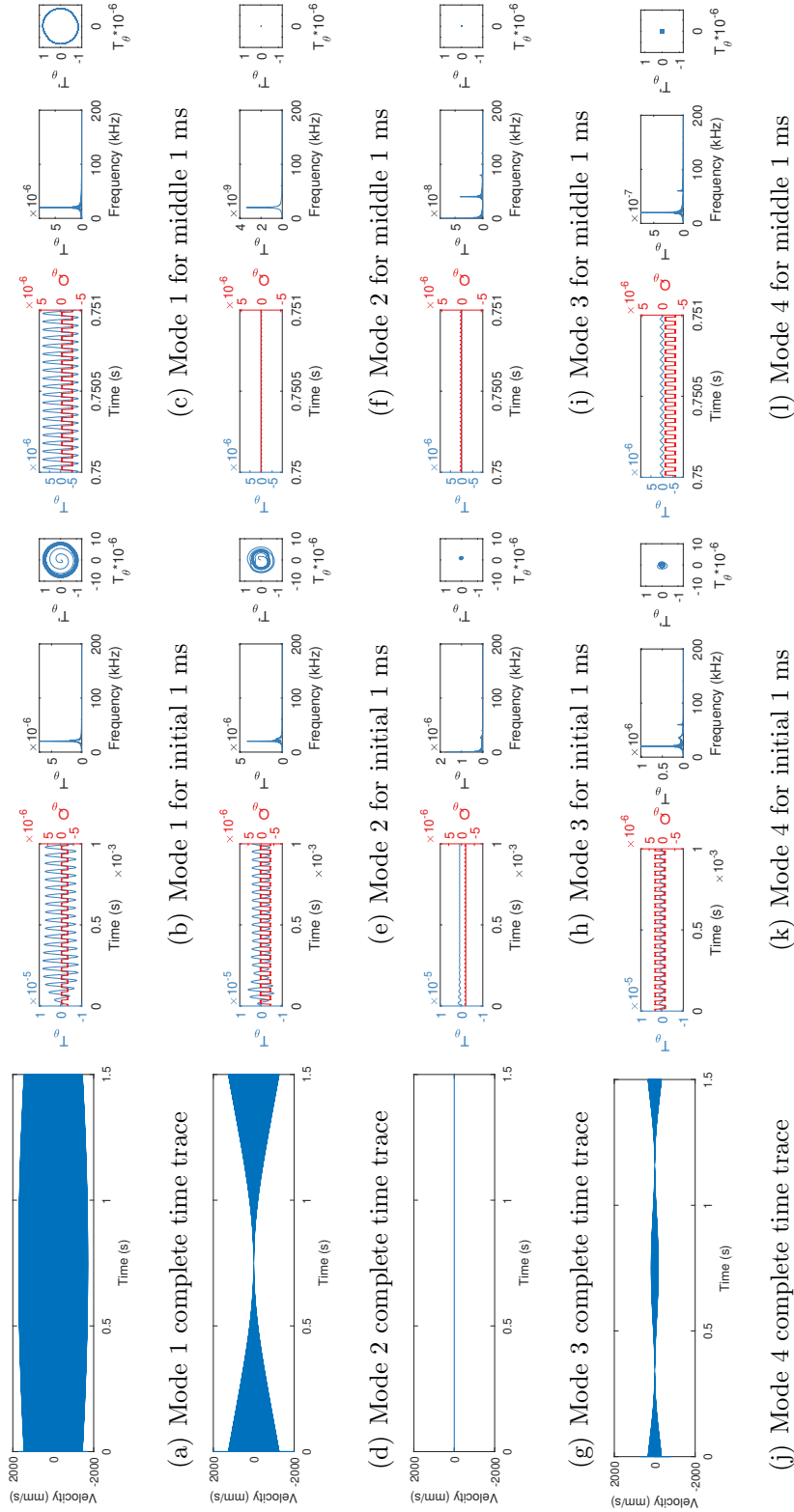


Figure 3.9. Pure slip forcing transverse velocity response for substrate height $a = 1$ in broken down. The first column is transverse velocity response modal contributions, the second column is the modal response in blue and forcing in red at $t = 0$ s, and third column is the modal response in blue and forcing in red at $t = 0.75$ s.

the response, seen in the first column of Figure 3.10. The modal contributions to the transverse velocity response for partial slip forcing has the same trends as those for pure stick forcing and pure slip forcing, seen in the first column in Figure 3.8 and Figure 3.9 respectively. The previously summarized trends are mode 1 is dominant and relatively invariant during the weld cycle, mode 2 contributes greatly at the beginning and end of the weld cycle, mode 3 is negligible, and mode 4 is relatively insignificant. The transverse velocity response to partial slip forcing is smaller in magnitude than the transverse velocity response to pure slip forcing and slightly smaller to pure stick forcing. The modal response and modal forcing variation in time to partial slip forcing is analyzed and illustrated in the second and third columns of Figure 3.10. The variation of the partial slip modal responses during the weld cycle follows the same trends as the modal contributions to the transverse velocity response for partial slip forcing during the weld cycle. Additionally, the modal response phase plots have similar trends as those for pure stick and pure slip forcing, seen in the second and third columns of Figure 3.8 and Figure 3.9 respectively. The modal forcing for modes 1, 2, and 4 resemble a clipped sine wave, which reinforces that the f_2 forcing component influences the responses of modes 1, 2, and 4. The f_2 forcing component for partial slip forcing contains higher-frequency harmonics, however, they have little impact on the magnitude of the transverse velocity response. This is likely due to choosing a less aggressive $\max F$, seen in Table 3.4, which is very close to the unclipped waveform amplitude. The resultant higher-order harmonics in the modal forcing are small in amplitude and do not greatly affect the transverse velocity response amplitude. The modal forcing for mode 3 contains a DC offset without a harmonic component, which is in agreement with the findings that this mode is influenced by the f_1 and f_3 forcing component.

From this analysis, the variation in the transverse velocity response amplitude with time is due to the moving line load cutting modes on and off during an entire weld cycle. For the height of $a = 1$ in, the dominant mode remains mode 1 for the entire weld cycle, however, mode 2 significantly impacts the transverse velocity response at

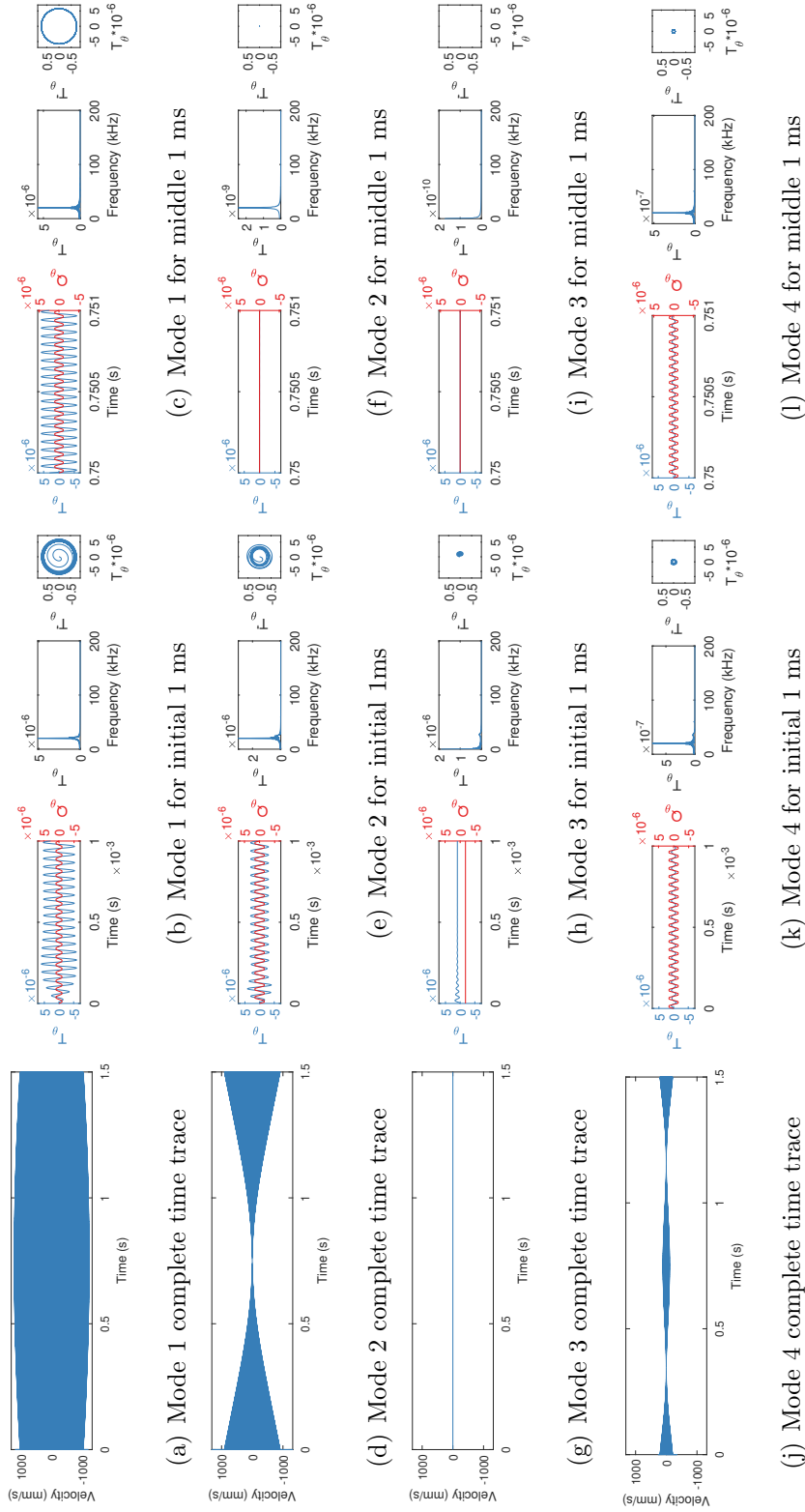


Figure 3.10. Partial slip forcing transverse velocity response for substrate height $a = 1$ in broken down. The first column is transverse velocity response modal contributions, the second column is the modal response in blue and forcing in red at $t = 0$ s, and third column is the modal response in blue and forcing in red at $t = 0.75$ s.

the beginning and end of the weld cycle. The trends of the modal contributions to the transverse velocity response do not change with the different forcing models. The dominant resonant interaction with the first mode could conceal the effects of the forcing models on the response, and hide the higher-order harmonics in pure slip and partial slip forcing.

3.4.2 Selective Time Traces at $a = 2$ in

Therefore, the next height to be investigated is $a = 2$ in because there are no resonances of the substrate with the excitation frequency, seen in Table 3.3.

3.4.2.1 Pure Stick Forcing

The transverse velocity response to pure stick forcing, shown in Figure 3.6(a), is broken down into the contribution from the first four modes, which can be seen in the first column of Figure 3.11. In this case, the transverse velocity response is dominated by mode 2 and mode 4. Mode 2 is dominant at the beginning and end of the weld cycle because of the torsional mode shape, and mode 4 is dominant at the middle of the weld cycle. The response from mode 1 is still significant, however, its contribution has decreased below the contribution of modes 2 and 4. The decrease in the contribution from mode 1 as the height was increased from $a = 1$ in to $a = 2$ in resulted from the shift down in the natural frequencies. The contribution of mode 3 to the transverse velocity response remains negligible. The wave-like variation in the transverse velocity response, seen in Figure 3.7(a), is caused by modes 2 and 4 cutting on and off during the weld cycle. The switching in dominant mode during the weld cycle at $a = 2$ in shows a change in dynamics from $a = 1$ in, where the dominant mode remains the same during the entire weld cycle. The modal response and modal forcing variation in time to pure stick forcing is analyzed and illustrated in the second and third columns in Figure 3.11. The variation of the pure stick modal responses during the weld cycle follows the same trends as the modal contributions to the transverse

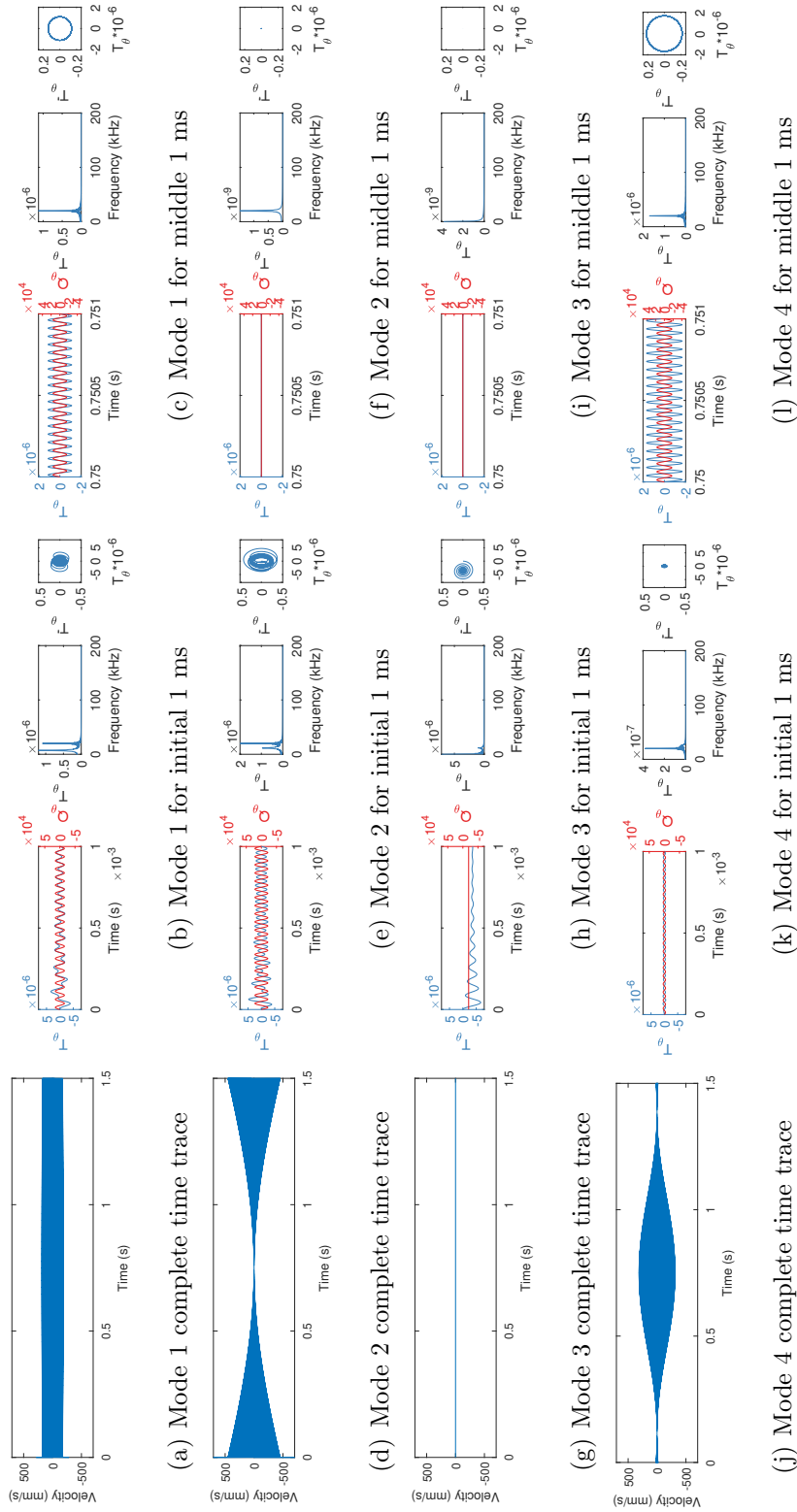


Figure 3.11. Pure stick forcing transverse velocity response for substrate height $a = 2$ in broken down. The first column is transverse velocity response modal contributions, the second column is the modal response in blue and forcing in red at $t = 0$ s, and third column is the modal response in blue and forcing in red at $t = 0.75$ s.

velocity response during the weld cycle for pure stick forcing. The phase plots for the modal responses show that at $t = 0$ s, seen in the second column, the response contains multiple harmonics due to the decaying transients. By the middle of the weld cycle, seen in the third column, the transients have been damped out and the response for modes 1 and 4 are single frequency, as indicated by the circular phase plots. Similar to $a = 1$ in, the pure stick f_2 forcing component influences modes 1, 2, and 4, and the f_1 forcing component influences mode 3.

3.4.2.2 Pure Slip Forcing

Continuing with the analysis of $a = 2$ in, the transverse velocity response to pure slip forcing, shown in Figure 3.6(b), is broken down into the contribution from first four modes, which can be seen in the first column in Figure 3.12. The modal contributions to the transverse velocity response for pure slip forcing has the same trends during the weld cycle as those for pure stick forcing, seen in the first column in Figure 3.11. These trends are mode 1 is significant but not dominant, mode 2 is dominant at the beginning and end of the weld cycle, mode 3 is negligible, and mode 4 is dominant in the middle of the weld cycle. The main difference between the forcing model results is the transverse velocity response to pure slip forcing is larger in magnitude than the transverse velocity response to pure stick forcing. The modal response and modal forcing variation in time to pure slip forcing is analyzed and illustrated in the second and third columns of Figure 3.12. The variation of the pure slip modal responses during the weld cycle follows the same trends as the modal contributions to the transverse velocity response for pure slip forcing during the weld cycle. The phase plots for pure slip modal responses differ from those for pure stick forcing, seen in the second and third columns of Figure 3.11. For pure slip, at $t = 0$ s, the modal responses look similar as to those for pure stick; however, at $t = 0.75$ s, the modal response for modes 1 and 4 are not perfectly circular, indicating that the response contains multiple harmonics. This trend differs from $a = 1$ in, where the

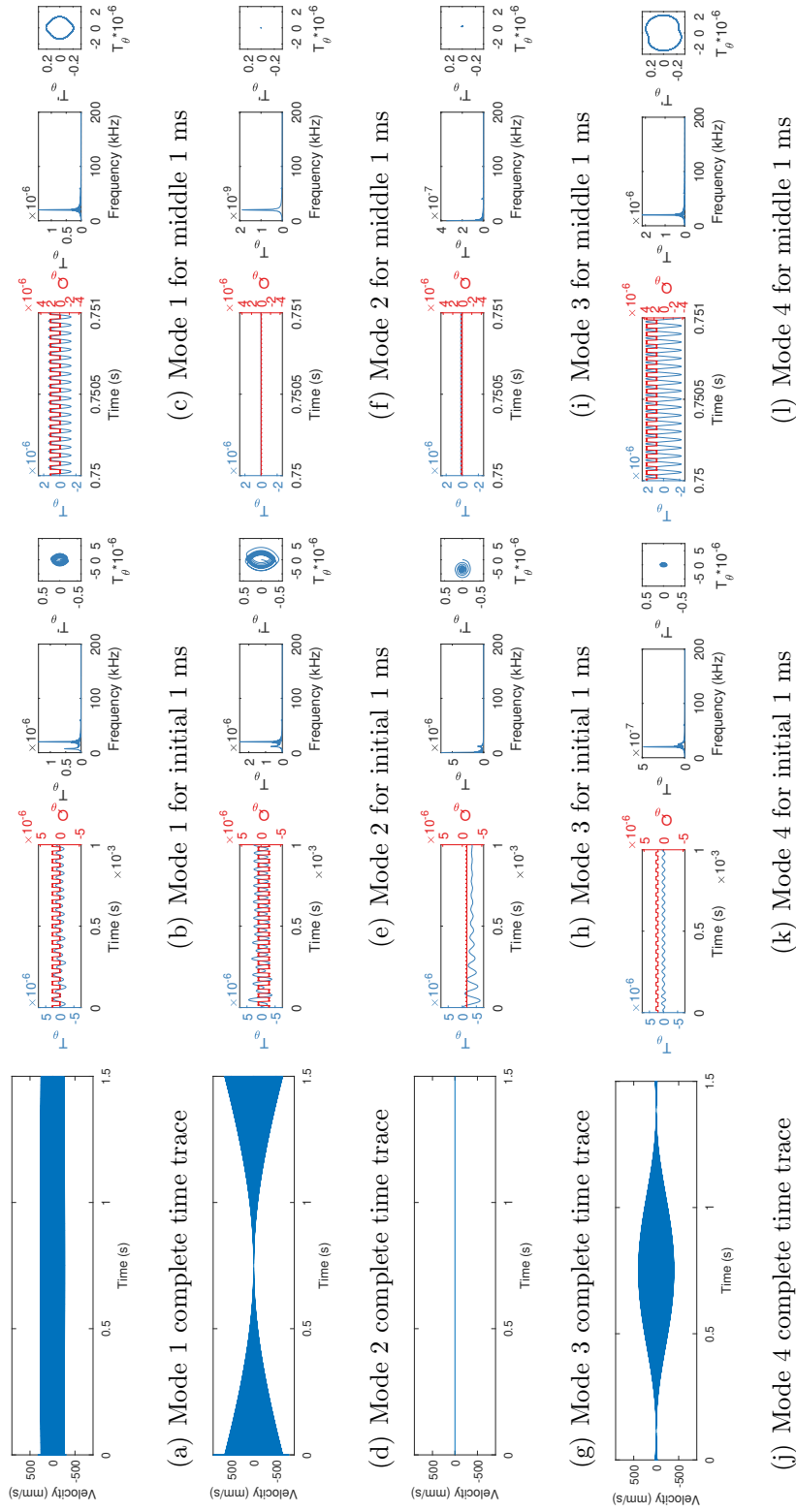


Figure 3.12. Pure slip forcing transverse velocity response for substrate height $a = 2$ in broken down. The first column is transverse velocity response modal contributions, the second column is the modal response in blue and forcing in red at $t = 0$ s, and third column is the modal response in blue and forcing in red at $t = 0.75$ s.

resonance of the first natural frequency dominated the response such that the higher-order harmonics are not observable. The pure slip f_2 forcing component influences modes 1, 2, and 4, and the f_1 and f_3 forcing components influence mode 3, which is similar to the results from $a = 1$ in.

3.4.2.3 Partial Slip Forcing

Finishing up the analysis of $a = 2$ in, the transverse velocity response to partial slip forcing, shown in Figure 3.6(c), is broken down into the contribution from the first four modes and can be seen in Figure 3.13. Once again, the modal contributions to the transverse velocity response for partial slip forcing has the same trends as those for pure stick and pure slip forcing, seen in Figure 3.11 and Figure 3.12 respectively. The trends are mode 1 is significant but not dominant, mode 2 is dominant at the beginning and end of the weld cycle, mode 3 is negligible, and mode 4 is dominant in the middle of the weld cycle. The transverse velocity response to partial slip forcing is smaller in magnitude than the transverse velocity response to pure slip forcing and slightly smaller to pure stick forcing. The modal response and modal forcing variation in time to partial slip forcing is analyzed and illustrated in the second and third columns in Figure 3.13. The variation of the partial slip modal responses during the weld cycle follows the same trends as the modal contributions to the transverse velocity response for partial slip forcing during the weld cycle. Additionally, the modal response phase plots have similar trends as those for pure stick forcing, seen in the second and third columns of Figure 3.11. Similar $a = 1$ in, the partial slip f_2 forcing component influences modes 1, 2, and 4, and the f_1 forcing component influences mode 3.

As the height increased from $a = 1$ in to $a = 2$ in, the dominant modes of the response switched from mode 1 to a combination of modes 2 and 4. The variation in the dominant modes as they cut on and off during the weld cycle results in a wave-like

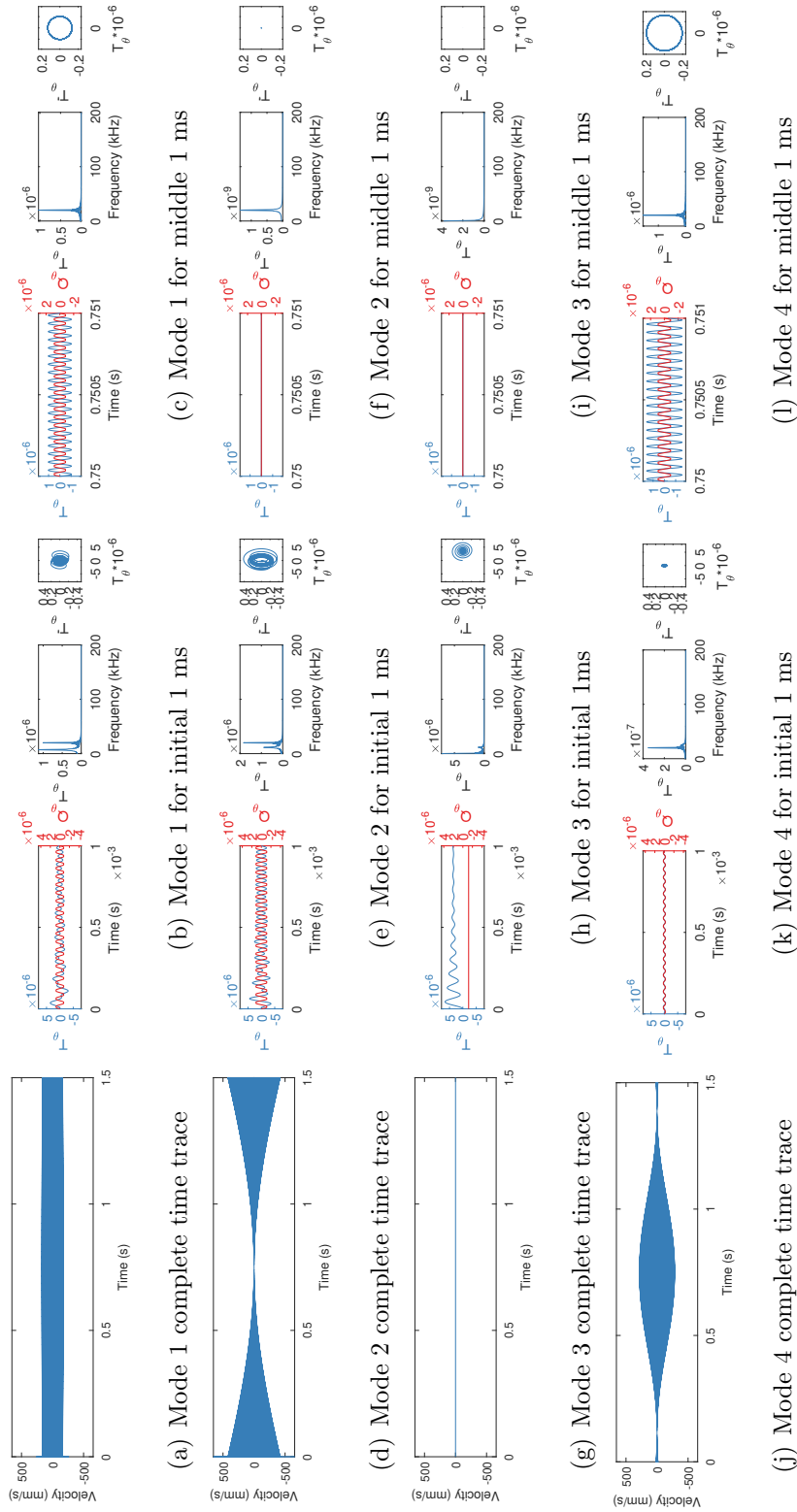


Figure 3.13. Partial slip forcing transverse velocity response for substrate height $a = 2$ in broken down. The first column is transverse velocity response modal contributions, the second column is the modal response in blue and forcing in red at $t = 0$ s, and third column is the modal response in blue and forcing in red at $t = 0.75$ s.

variation in the transverse velocity response amplitude at $a = 2$ in. Similar to $a = 1$ in, the dominant modes are the same for all forcing models at $a = 2$ in.

3.4.3 Selective Time Traces at $a = 2.5$ in

To complete this analysis, the height is further increased to $a = 2.5$ in where mode 4 becomes resonant.

3.4.3.1 Pure Stick Forcing

The transverse velocity response to pure stick forcing for $a = 2.5$ in, shown in Figure 3.7(a), is broken down into the contribution from the first five modes, which be seen in the first column in Figure 3.14. In this case, the transverse velocity response is dominated by mode 4. Modes 2 and 5 have a negligible effect on the response, whereas modes 1 and 3 have a significant but not dominant effect. Therefore, it appears that there has been some mode switching phenomenon in that the "order" of modes 2 and 3 have been reversed from the $a = 2$ in cases. The dominance of mode 4 explains the change in the transverse velocity response from $a = 2$ in to $a = 2.5$ in. The modal response and modal forcing variation in time to pure stick forcing is analyzed and illustrated in the second and third columns of Figure 3.14. The variation of the pure stick modal responses during the weld cycle follows the same trends as the modal contributions to the transverse velocity response for pure stick forcing during the weld cycle. Similar to previous heights, the phase plots at $t = 0$ s indicate that the response contains multiple harmonics due to transients, but are damped out by the middle of the weld cycle at $t = 0.75$ s, resulting in circular phase plots. Due to the modal switching, the f_2 forcing component influences the responses in modes 1, 3, and 4, as indicated by the harmonic waveform of the respective modal forcing. The modal forcing for modes 3 and 5 contains a DC offset, which indicates that the normal f_1 forcing component influences the response of modes 2 and 5.

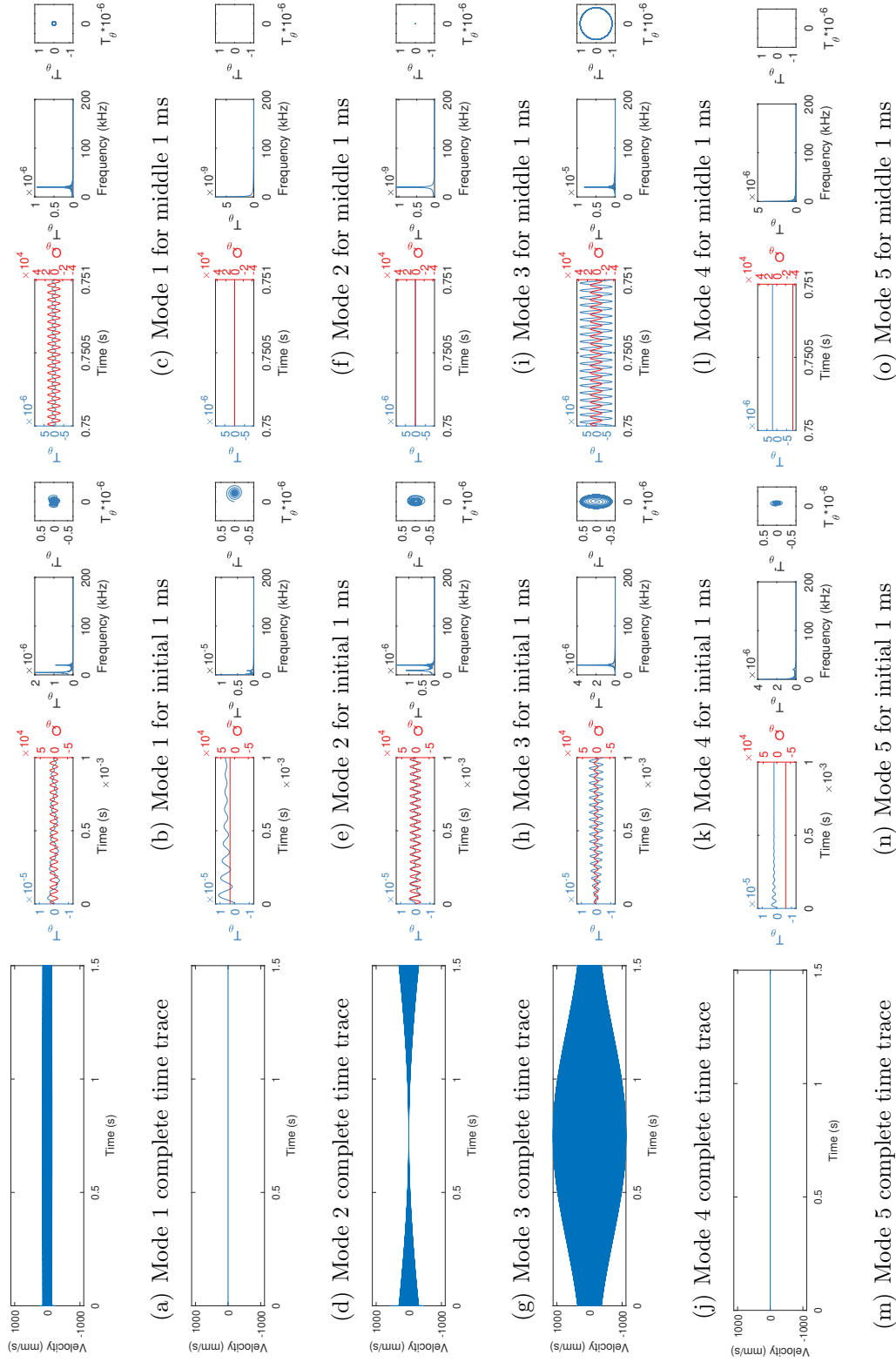


Figure 3.14. Pure stick forcing transverse velocity response for substrate height $a = 2.5$ in broken down. The first column is transverse velocity response modal contributions, the second column is the modal response in blue and forcing in red at $t = 0$ s, and third column is the modal response in blue and forcing in red at $t = 0.75$ s.

3.4.3.2 Pure Slip Forcing

The transverse velocity response to pure slip forcing, shown in Figure 3.7(b), is broken down into the contribution from the first five modes, which can be seen in the first column in Figure 3.15. The modal contributions to the transverse velocity response for pure slip forcing has the same trends as those for pure stick forcing, seen in Figure 3.14. Specifically, mode 1 is significant but not dominant, mode 2 is negligible in the response, mode 3 contributes significantly at the beginning and end of the weld cycle, mode 4 is dominant but its dominance varies during the entire weld cycle, and mode 5 is negligible in the response. The magnitude of the transverse velocity response to pure slip forcing is larger than that for pure stick forcing. The modal response and modal forcing variation in time to pure slip forcing is analyzed and illustrated in the second and third columns of Figure 3.15. The variation of the pure slip modal responses during the weld cycle follows the same trends as the modal contributions to the transverse velocity response during the weld cycle for pure slip forcing. The modal response phase plots have similar trends as those for pure stick forcing, seen in the second and third columns of Figure 3.14. The similarity of the phase plots at $t = 0.75$ s is attributed to a resonance dominating the response and hiding the multiple-harmonics. The modal forcing for modes 1, 3, and 5 are square waves, which indicates that these modes are influenced by the f_2 forcing component. The modal forcing for mode 2 contains a DC offset with an impulse-like harmonic waveform indicating that the f_1 and f_3 forcing components influence the response of mode 2. The modal forcing for mode 5 only contains a DC offset, which indicates that the response in mode 5 is influenced by the normal f_1 forcing component.

3.4.3.3 Partial Slip Forcing

Finally for $a = 2.5$ in, transverse velocity response to partial slip forcing, shown in Figure 3.7(c), is broken down into the contribution from the first five modes and can be seen in the first column of Figure 3.16. The modal contributions to the

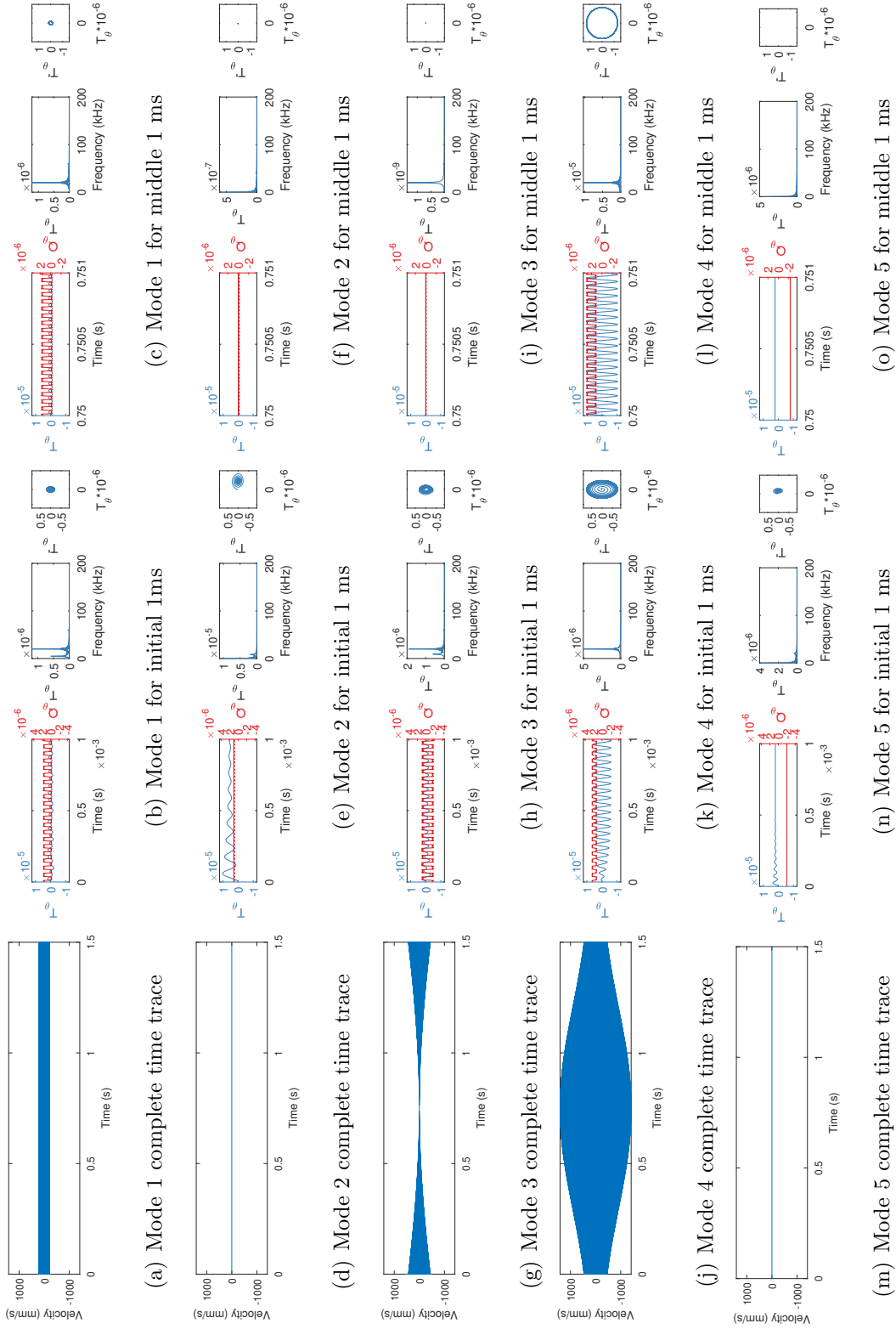


Figure 3.15. Pure slip forcing transverse velocity response for substrate height $a = 2.5$ in broken down. The first column is transverse velocity response modal contributions, the second column is the modal response in blue and forcing in red at $t = 0$ s, and third column is the modal response in blue and forcing in red at $t = 0.75$ s.

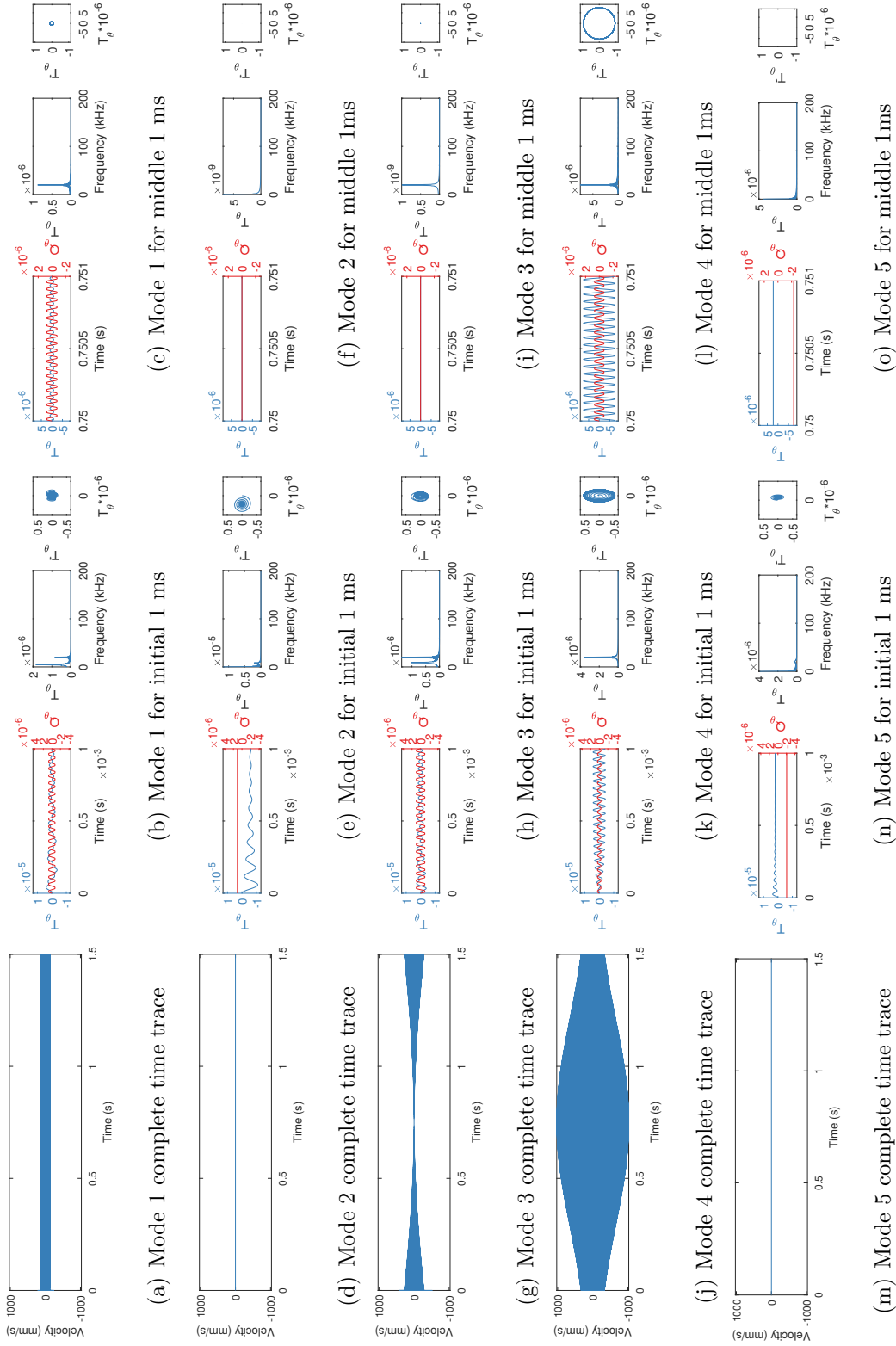


Figure 3.16. Partial slip forcing transverse velocity response for substrate height $a = 2.5$ in broken down. The first column is transverse velocity response modal contributions, the second column is the modal response in blue and forcing in red at $t = 0$ s, and third column is the modal response in blue and forcing in red at $t = 0.75$ s.

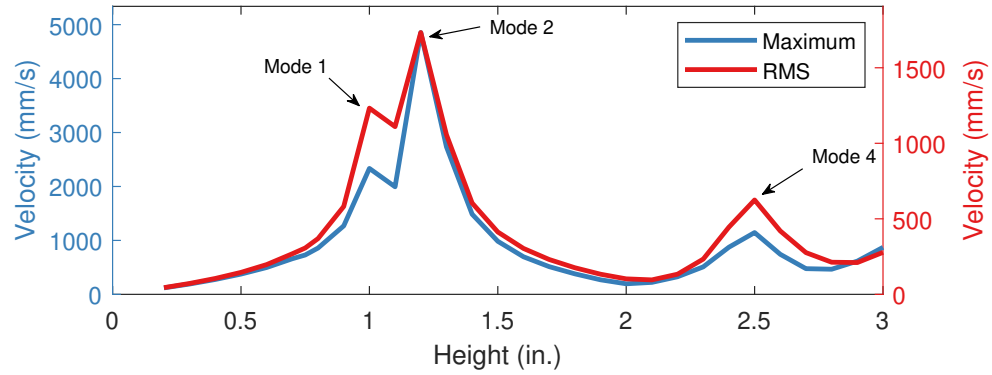
transverse velocity response for partial slip forcing has the same trends as those for pure stick and pure slip forcing, seen in the first column of Figure 3.14 and Figure 3.15 respectively. These trends are that mode 1 is significant but not dominant, mode 2 is negligible, mode 3 contributes significantly at the beginning and end of the weld cycle, mode 4 is dominant but its dominance varies during the entire weld cycle, and mode 5 is negligible. The transverse velocity response to partial slip forcing is smaller in magnitude than the transverse velocity response to pure slip forcing and slightly smaller to pure stick forcing. The modal response and modal forcing variation in time to partial slip forcing is analyzed and illustrated in the second and third columns of Figure 3.16. The variation of the partial slip modal responses during the weld cycle follows the same trends as the modal contributions to the transverse velocity response during the weld cycle for partial slip forcing. The modal response phase plots have similar trends as those for pure stick and pure slip forcing, seen in the second and third columns of Figure 3.14 and Figure 3.15 respectively. The transverse f_2 forcing component is responsible for the responses of modes 1, 3, and 4, which is indicated by the clipped sine waveform of the respective modal forcing. The modal forcing for modes 2 and 5 contains a DC offset with no harmonic component because partial slip forcing does not contain a f_3 forcing component.

From these analyses, the transverse velocity response is mainly influenced by the first four modes. As the height of the substrate is varied, the dominant modes in the transverse velocity response change. At $a = 1$ in mode 1 is dominated, at $a = 2$ in modes 2 and 4 are dominant, and at $a = 2.5$ in mode 4 is dominant. The transverse velocity response of the substrate varies during a weld cycle due to modes cutting on and off as the moving line load traverses the substrate length. The f_2 forcing component is largely responsible for the transverse velocity response, while the other forcing components have a negligible impact. With the current model, the dominant mode and the shape of transverse velocity response during the weld cycle is sensitive to the substrate height and the point in the weld cycle, but insensitive to the forcing model used. We have shown that the transverse velocity response varies greatly

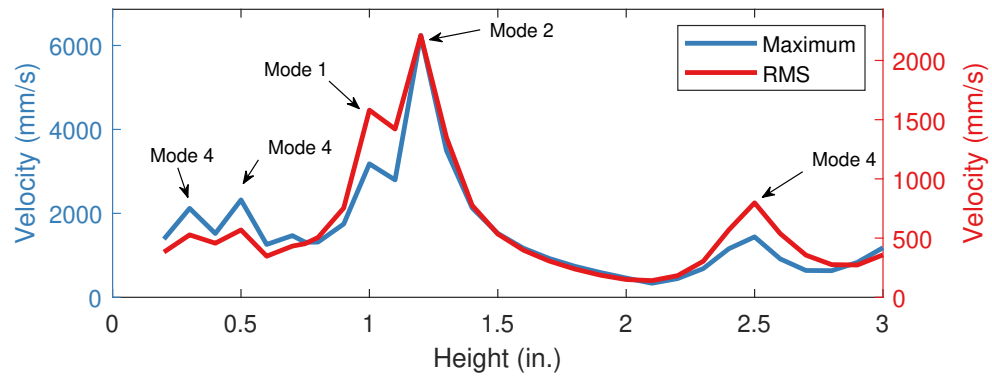
during a weld cycle, and thus the entire weld cycle must be considered during model development. To further test the height dependence and effect of a forcing model, a wider range of heights are investigated in the following section to find potentially problematic substrate heights, or height-to-width ratios.

3.5 Transverse Velocity Response to Variations in Substrate Height

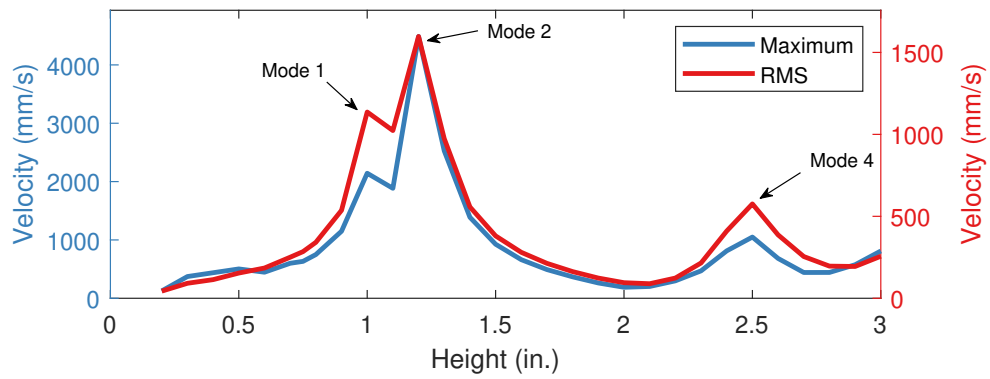
In the previous section, we demonstrated that for a discrete number of heights, higher-order modes can become dominant and that the trends in the transverse velocity response were not affected by the forcing model used. In order to be confident in this conclusion, we simulated the transverse velocity response under the moving line load ($x_1 = a, x_2 = 0, x_3 = z_0 + st$), using the same simulation parameters used in Section 3.3, except a was varied from 0.2 in to 3 in at a step size of 0.1 in. The maximum and RMS values of the transverse velocity responses beginning from $t = 1$ ms to ignore high-amplitude transients were determined using MATLAB, and a curve was generated as a function of height, seen in Figure 3.17. The overall trends in the transverse velocity response versus height for pure stick, pure slip, and partial slip forcing are similar. At heights below the critical height-to-width ratio, the maximum and RMS values of the transverse velocity response are less than those at the critical height-to width ratio. As the height approaches the critical height-to-width ratio, the maximum and RMS values of the response increase due to the resonance of the first mode, seen in Table 3.3. As the height is further increased, the maximum and RMS velocity response curves increase to a maxima at a height of 1.2 in due to the resonance of the second mode. This trend has not been demonstrated experimentally, however, the model in [12] predicted the linear weld density, a bonding quality indicator, to be at a minimum at a height-to-width ratio of 1.2. As the height is further increased, the maximum and RMS velocity response curves decrease to a local minima near a height of 2 in. This is in agreement with the experimental trends seen in [17] in that bonding could be reinitiated at this substrate height. Furthermore, as



(a) Pure stick forcing



(b) Pure slip forcing



(c) Partial slip forcing

Figure 3.17. Maximum and RMS of transverse velocity response directly under forcing model moving line load versus height for substrate of width $b = 1$ in, text arrows indicate dominant modes.

the height is increased to 2.5 in, another peak in the maximum and RMS velocity response curves occur due to a resonance of the fourth mode. As the height passes this peak, the maximum and RMS velocity response curves decrease in value. Near the end of the height range in this study, there is a slight increase in maximum and RMS velocity response curves, which could be caused by resonances of higher-order modes. The differences in maximum and RMS velocity response curves are attributed to the transverse velocity response variation in time as modes are cut on and off during the entire weld cycle.

Although the trends of the transverse velocity response for pure stick, pure slip, and partial slip forcing with respect to height are similar, there are some differences between the pure slip and pure stick/partial slip forcing response curves. In analyzing the causes for these differences, the focus will be on the f_2 component in the different forcing models. In the pure slip response curves, seen in Figure 3.17(b), there are peaks at heights less than the critical height-to-width ratio, $a = 1$ in. These peaks are attributed to the f_2 component for pure slip forcing containing multiple harmonic frequencies. The harmonic frequencies are multiples of the excitation frequency can become resonant with natural frequencies at heights less than critical height-to-width ratio because the natural frequencies are greater than the excitation frequency. As mentioned previously, the magnitude of the response for pure slip forcing is greater than that for either pure stick or partial slip forcing. This difference in magnitude was attributed to the f_2 component waveform component which resembles a square wave, as compared to the sine wave and clipped sine wave for pure stick and partial slip forcing respectively. The square wave waveform results in an increased energy input into the response which explains the increase in magnitude from pure slip forcing. The f_2 component for partial slip also contains multiple harmonic frequencies due to the clipped sine waveform; however, the parameters used in this study are such that very little energy is put into the higher-order harmonic components, and thus there are no peaks in the response curve at heights less than the critical height-to-width ratio.

The transverse velocity response curves in Figure 3.17 can be thought of as analogous to a frequency response function plot. Peaks in the maximum and RMS transverse velocity response curves indicate that at that height, the substrate transverse dynamic compliance is at a maxima. This can be used to infer that at that height, the differential motion between the foil and substrate will decrease, and thus bonding degradation will occur. In our current model, we demonstrate that there is a maxima in the velocity response curves at a height of 1.2 in. This additional problematic height, or height-to-width ratio, has not been demonstrated in experimental testing, but has been predicted in a previous model [12]. No experimental studies have shown the response amplitude past a height of 2in. The peaks at a height of 1.2 in and 2.5 in are caused by the higher-order dominant modes, which indicates that a single-mode approximation cannot sufficiently describe the dynamics of the substrate at heights above the critical height-to-width ratio. The current model approximates the interfacial friction between foil and substrate, and assumes the interfacial friction waveform is constant. In reality, the waveform is dependent upon the interfacial slip between foil and substrate, and thus will not be constant. However, the applied line load contained approximations of the interfacial friction for varying degrees of differential motion from pure stick to pure slip, and the general trend of the response curves remained the same. Therefore, it is likely that these trend predictions are valid if a linear model is sufficient to describe the dynamics of the substrate during the UAM process. Additionally, we assumed that coefficient of friction is constant. As shown in Appendix D, the coefficient of friction, μ , is proportional to the magnitude of substrate response. Thus, the qualitative trends in the response will not change by increasing or decreasing the coefficient of friction value.

3.5.1 Critical Height-To-Width Ratio At Substrate Width of 0.5 in

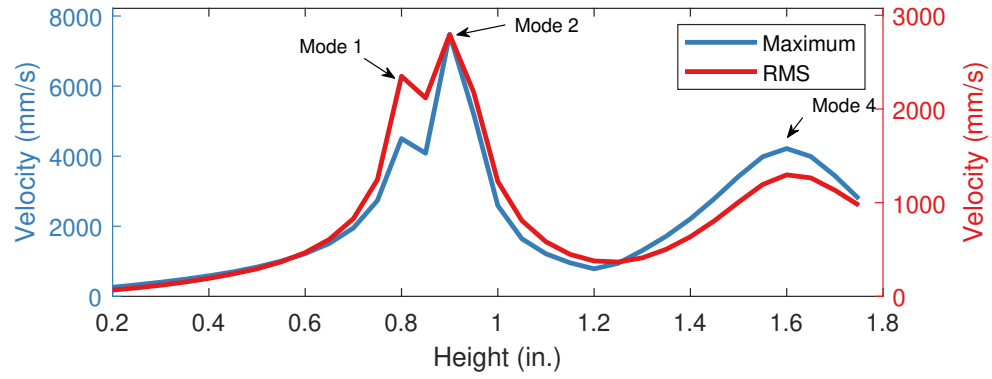
The focus of this chapter has been on studying the response of the substrate with the nominal tape width $b = 1$ in; however, in [16] additional widths were tested, and

demonstrated that the critical height-to-width ratio also occurs at a substrate width of $b = 0.5$ in. Changing the dimensions of the substrate also changes the natural frequencies, and thus there should be no resonant interactions with the sonotrode at the critical height-to-width ratio. Therefore, the physics behind the critical height-to-width ratio at this substrate width differs from that of the nominal tape width, $a = 1$ in. For this reason, a preliminary study was performed to address this concern. Maximum and RMS transverse velocity response curves were developed using the same parameters as previous analysis, however, now the width of the substrate is $b = 0.5$ in and the height is varied from $a = 0.2$ in to $a = 1.75$ in. The results for these simulations were repeated for the three forcing models and can be seen in Figure 3.18.

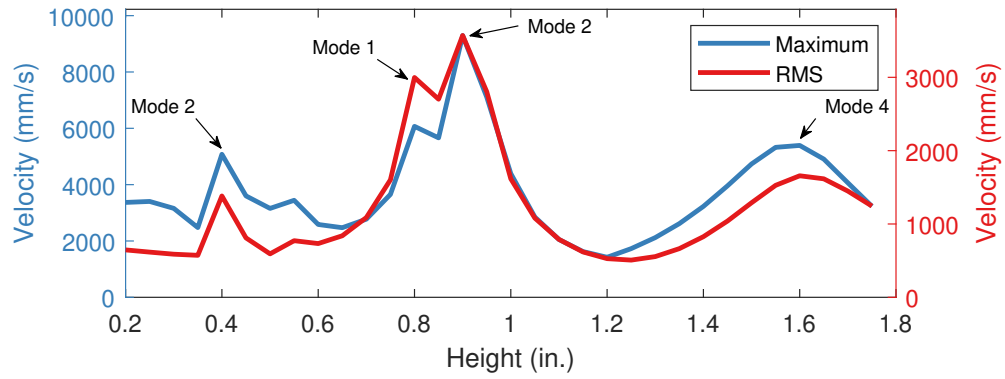
The maximum and RMS values of the transverse velocity response at the critical height-to-width ratio (in this case at $a = 0.5$ in) are nominally less than or equal to the values at all greater heights. Therefore, the bond degradation at the critical height-to-width ratio occurs due to an increase in dynamic compliance that remains above this nominal dynamic compliance level for all heights greater than $a = 0.5$ in. The model results for a substrate width $a = 0.5$ in appear to agree with experimental observations and provide a limited explanation for the critical height-to-width ratio occurring at a width of 0.5 in as compared to the nominal tape width 1 in.

3.6 Summary

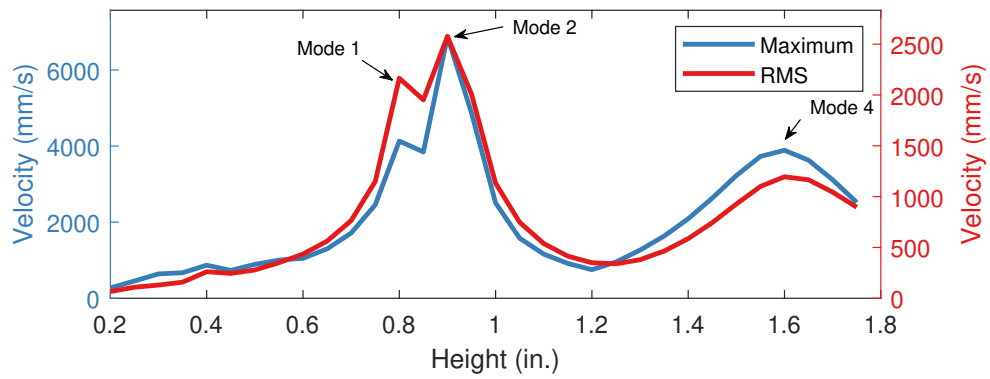
This chapter presents the simulation results of the current UAM model for the three forcing models to study the resonant interactions between the substrate and sonotrode. The natural frequencies converge to the natural frequencies of a FE model in ABAQUS as the span of basis functions increases. At the span of $I = 7$, $K = 5$, and $J = 5$, the percent difference between the first ten modal frequencies of the Galerkin approximation and the FE model is less than 3%. As the height increases above the critical height-to-width ratio, higher-order modes become resonant with the sonotrode



(a) Pure stick forcing



(b) Pure slip forcing



(c) Partial slip forcing

Figure 3.18. Maximum and RMS of transverse velocity response directly under forcing model moving line load versus height for substrate of width $b = 0.5$ in, text arrows indicate dominant modes.

excitation frequency. All three forcing model results show a good qualitative match with experimental results from [17]. During a weld cycle, the moving line load, i.e. the sonotrode, is traversing the substrate length resulting in modes cutting on and off, which causes variation in the transverse velocity response of the substrate. In addition, the dominant mode in the transverse velocity response changes as the substrate height increases. Using this model, a prediction of problematic heights, or height-to-width ratios, due to an increase in transverse dynamic compliance of the substrate was established. Additionally, a limited explanation was provided for the experimental observations of the critical height-to-width ratio phenomenon for a substrate width of 0.5 in, as compared to the nominal tape width.

4. EMBEDDING TRIBOELECTRIC NANOGENERATOR IN METAL MATRIX VIA UAM

4.1 Introduction

With the advent of drones and unmanned aerial vehicles for military uses, novel sensors have to be created to fill the requirements of this emerging technology. One area of promising research is the development of embedded sensors. Embedding a sensor within a structure reduces potential damage to the sensor and allows for real-time monitoring of the structure. However, embedding sensors in metal-matrices poses a challenge due to issues with typical fabrication techniques, but with UAM the low process temperature allows for direct embedding of sensors without the need for protective layers around the typically sensitive devices [1, 21]. Previous research in UAM has embedded fiber optics, fiber Bragg gratings, and PVDF phases in aluminum matrices [38, 51–56, 59]. However, these sensor devices are fragile, expensive, or require specialized equipment to monitor. A sensor technology that has not been used in UAM is triboelectric nanogenerators (TENGs). TENGs are useful because they are flexible, robust, inexpensive, easy to manufacture, and have a simple output measurement.

4.2 Triboelectric Nanogenerator

Triboelectric nanogenerators (TENGs) were first developed in 2012 by [63], and have a wide variety of uses ranging from energy harvesting to structural health monitoring. TENGs have four basic working modes: 1) vertical-contact separation, 2) in-plane sliding, 3) single-electrode, and 4) free-standing triboelectric layer [63]. The following discussion will focus on the mode most suitable for the devices considered in this work: vertical-contact separation. The basic mechanism behind a vertical-

contact separation TENG can be demonstrated using Figure 4.1 (a) as a reference. The TENG consists of two dielectrics separated by an air gap. On the opposite surface of the dielectrics are conductive electrodes. As one or both of the dielectrics

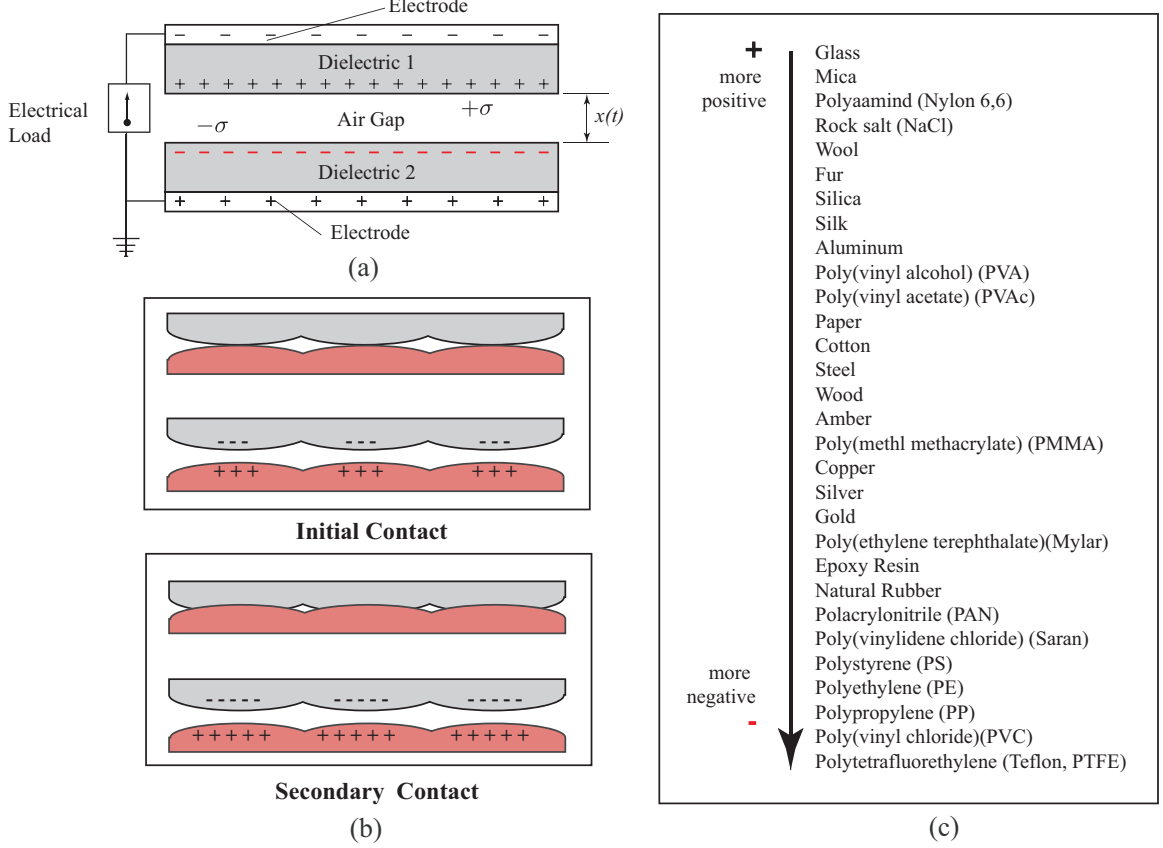


Figure 4.1. Vertical contact mode triboelectric nanogenerator: (a) schematic of two dielectric generator, (b) process of contact electrification, and (c) triboelectric series that is an amalgamation of several different series from the literature [64].

are perturbed by external excitation, the dielectric surfaces come into contact producing opposite charges through contact electrification [63], seen in Figure 4.1 (b). Subsequently, the contact surface charges on the dielectrics produce opposite charges on the electrodes through electrostatic induction [63]. The free charges on the elec-

trodes can produce a short-circuit current to balance the electrostatic equilibrium or an open-circuit voltage across the electrodes.

The working materials in TENGs are determined using the “triboelectric series”, i.e., a list of materials empirically ordered based on their tendency to acquire a positive or negative charge, seen in Figure 4.1 (c). It is important to note, the underlying physics behind this chart are still in question. As an example, both polyethylene and Teflon®(PTFE) are considered nonpolar, meaning they contain no permanently dipolar molecules, however, they develop strong negative charges upon contact. Despite this contradiction, the triboelectric series has been established for 150 years and forms the basis for determining the material pairings for triboelectric devices developed to date. Using the series and basic design of vertical-contact separation, TENGs can be used as self-powered sensors for detecting external stimuli via the deformation of the TENG [65,66].

TENGs can be applied to current UAM research to develop a novel proof-of-concept embedded sensor in a metal-matrix that detects contact or impact of an external object with the metal-matrix. The development of an embedded sensor can then be expanded to build a spatially-dependent embedded sensor array. The remainder of this chapter begins with the development of two single sensor designs and uses one of the designs to create a sensor array. Following the sensor design, the sensors are fabricated and then embedded in a metal-matrix using UAM. Then, the embedded sensors are tested using touch testing for preliminary evaluation of sensors, solenoid testing for sensor characterization, and drop testing to demonstrate impact detection.

4.3 Design of TENG-AL3003 Composites

The TENG sensors used in this study are in vertical-contact separation mode. The cross-section of the TENG is shown in Figure 4.2 (a). The sensors are made from a

combination of Kapton and ITO/PET (Indium tin oxide/polyethylene terephthalate) layers, and the metal-matrix is AL3003.

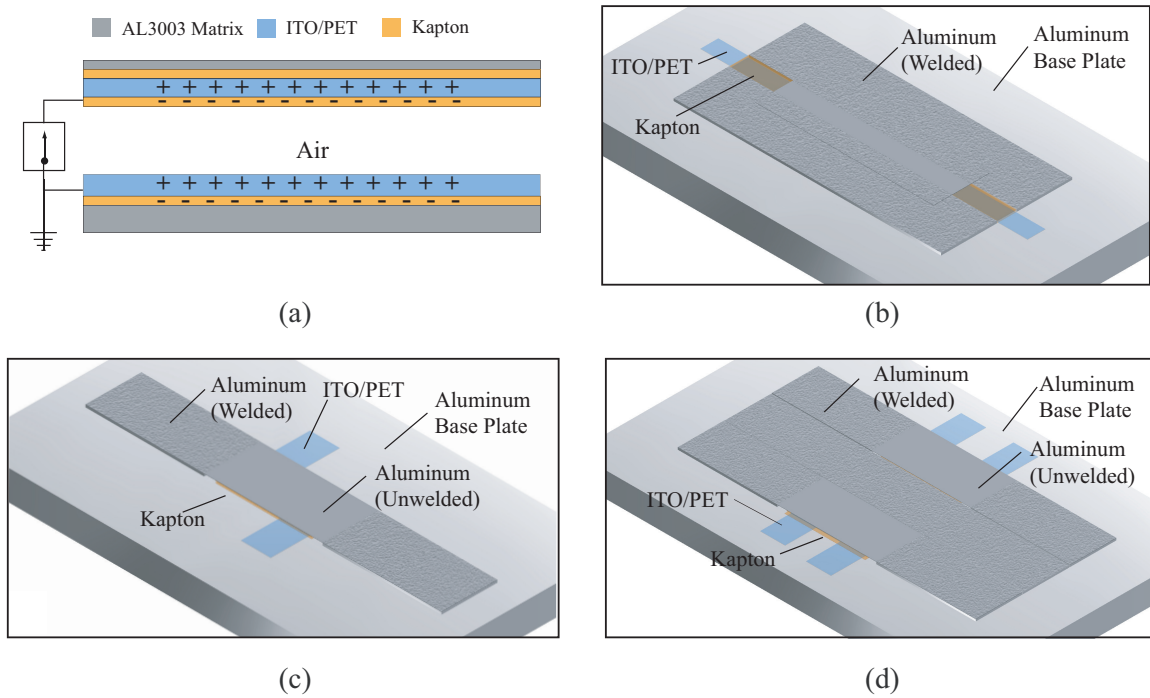


Figure 4.2. Triboelectric metal-matrix composite: (a) embedded TENG sensor cross-section with ITO/PET and Kapton dielectric layers, (b) single sensor channel design, (c) single sensor pocket design, and (d) pocket design sensor array.

The Kapton layer between the ITO/PET layer and AL3003 matrix is used to insulate the TENG sensor from the electrically-conductive matrix. The dielectric surfaces for this design are Kapton for the top part, and ITO/PET for the bottom part. The electrode for the top part and bottom part of the TENG is the ITO/PET layers. Thus, the ITO/PET layer acts as both the dielectric and electrode for the bottom part.

The typical method of embedding components is creating a channel or a pocket in the substrate, placing the component in the channel/pocket, and then welding a

foil or metal tape over the channel/pocket. From the embedding methodology, two general matrix designs were developed: a channel design, and a pocket design.

Seen in Figure 4.2 (b), for the channel design, the individual layers are bonded to create the channel, and the TENG sensor is placed between built sections. The channel width is 0.33 in, or a third of the nominal tape width in UAM. The channel length is 4 in, although the embedded section is only 3 in. The top part of the TENG is adhered to the embedding foil, and the bottom part of the TENG is adhered to the substrate. The channel depth is such that there should be an approximate 0.1 mm gap between the top and bottom parts of the TENG.

In the pocket design, the pocket is created by building two tabs on the baseplate that are separated by 2 in, then adhering the top part of the TENG to the embedding tape and the bottom part to the substrate within the pocket, and finally welding the embedding tape to the tabs. The pocket width is equal to a tape width, 0.9375 in, and the end tabs have a length of 2 in and a width equal to the tape width. The pocket depth, or the tab heights, are such that there will be a small gap, on the order of 0.1 mm, between the top and bottom parts of the TENG. Two prototypes of this design will be fabricated. The first is a prototype of a single embedded sensor, seen in Figure 4.2 (c). The second prototype for the pocket design, seen in Figure 4.2 (d), is a spatially-dependent sensor array. The two pockets are separated by a welded section of aluminum tapes of width 0.9375 in and length of 6 in. Note that for the pocket design, the TENG is not fully encapsulated; however, the objective of this research was to develop a proof-of-concept, and this design is sufficient to illustrate the concept of a metal structure enclosing a TENG.

4.4 Fabrication of TENG-AL3003 Composites

The TENG sensor components were fabricated in the ADAMS lab. In manufacturing the pocket design, a square of dimensions 1.5 in by 1.5 in was cut out of an ITO/PET sheet of thickness 0.2 mm using a manual paper cutter. After creating

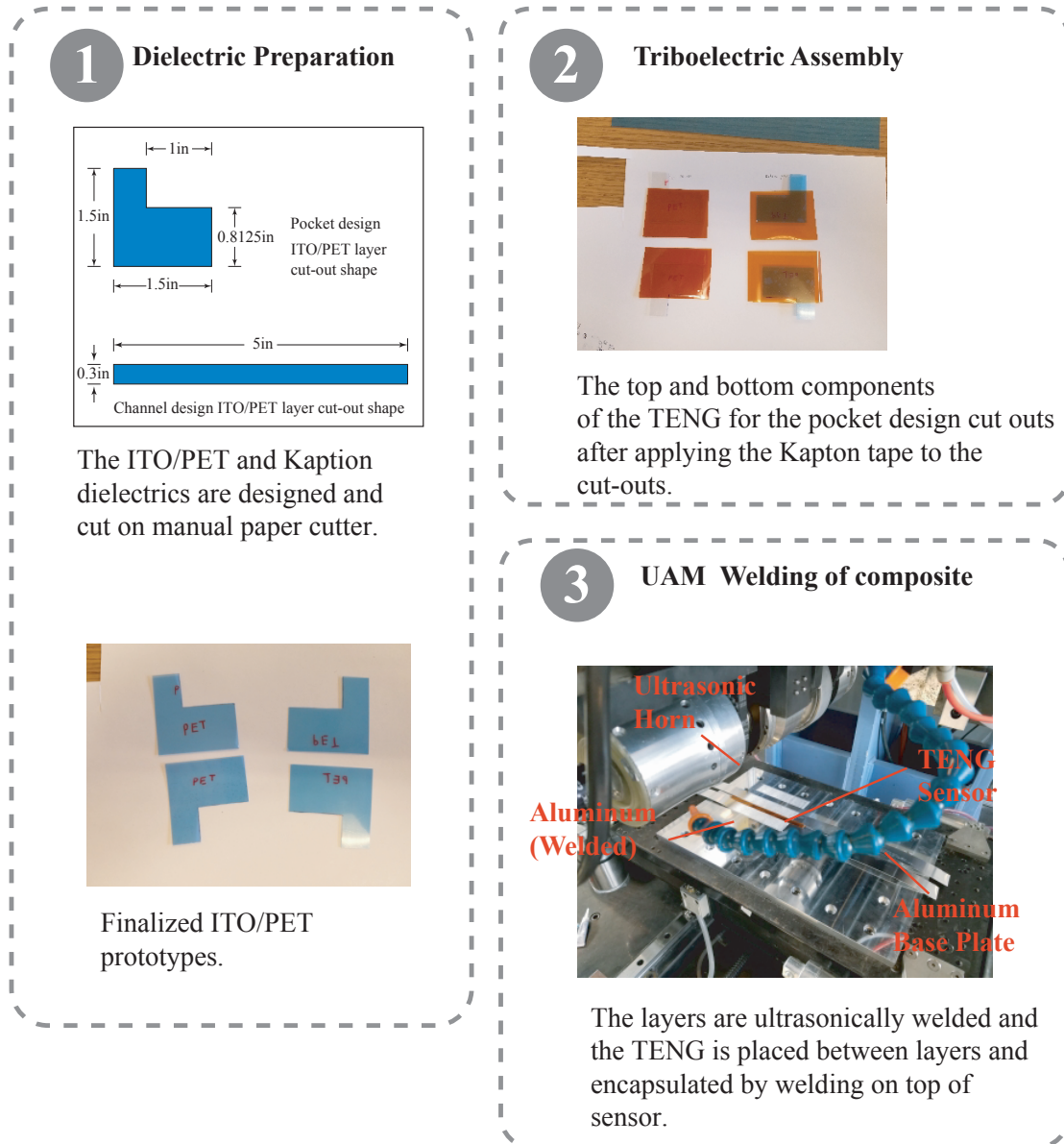


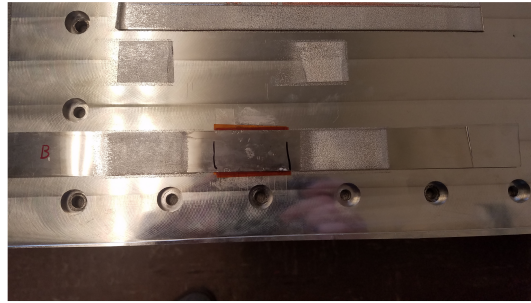
Figure 4.3. Schematic of complete manufacturing and assembly of TENG metal-matrix composites using UAM.

the square piece of ITO/PET, the shape outline for the top and bottom parts of the TENG sensor were traced onto the ITO/PET square using a pen. The shape was then cut out using scissors, which the cut-outs for the pocket design can be seen in Figure 4.3.

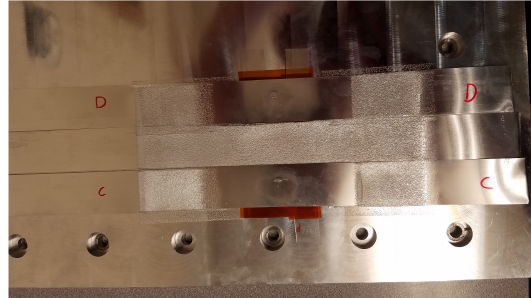
Next, the top part of the TENG sensor was wrapped in Kapton tape (thickness of 0.0025 in), and Kapton tape was adhered to the bottom side of the bottom part of the TENG sensor. The top and bottom parts of the TENG sensor for the pocket design can be seen in Figure 4.3 after applying the Kapton tape to the cut-outs. Excess Kapton was trimmed from the cut-outs using scissors and an X-acto knife leaving about 1/16 in on each side. A similar procedure was repeated for the channel design TENG sensor parts except the dimensions are different, which can be seen in Figure 4.3.

Once the parts for the embedded TENG sensor were created, the metal-matrix was built on a Fabrisonic R220 UAM machine, which is a 5kW single transducer UAM system. This system was calibrated and the sonotrode cleaned using the procedures in Appendix D and Appendix E, respectively. For the channel design, the channel walls were built by welding five successive layers of AL3003 tapes, each with thickness of 0.15 mm. The welding parameters used to create the metal-matrix were a compressive force of 900 lbf, weld speed of 125 ipm, and an amplitude of 16 μ m. In creating the metal-matrix, the bottom part of the TENG sensor was adhered to the substrate inside the channel walls with Loctite super glue, and the top part of the TENG sensor was adhered to the bottom surface of the embedding AL3003 tape also with Loctite super glue. The AL3003 channel design metal-matrix with the bottom part of the TENG sensor adhered to the substrate can be seen in Figure 4.3.

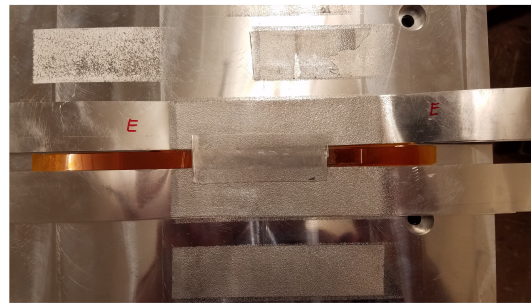
The super glue was allowed to cure, and then the AL3003 tape with the top part of the TENG sensor was manual placed over the channel to be centered over the bottom part of the TENG sensor. Additionally, the tape was centered over the channel width so that the tape could successfully be bonded to the metal-matrix. The tape was clamped and then welded to the channel metal-matrix using the aforementioned welding parameters, except the normal load was decreased to 600 lbf because the surface area of the welded section of the tape was decreased. The completed build for the single sensor channel design, named sensor E, is shown in Figure 4.4 (c).



(a)



(b)



(c)

Figure 4.4. Prototypes of TENG metal-matrix composites: (a) sensor B, (b) sensors C and D, and (c) sensor E.

The fabrication process for the pocket design metal-matrix began with successive welding of five layers of AL3003 tape for each tab, using the welding parameters: a compressive force of 900 lbf, weld speed of 125 ipm, and an amplitude of $16\ \mu\text{m}$. After building the pocket design metal-matrix, the bottom part of the TENG sensor is manually centered and adhered to the baseplate between the tabs, and the top part of the TENG sensor is manually adhered to the bottom surface of the embedding

AL3003 tape. The superglue was cured, and then the embedding tape was placed across the tabs such that top part of the TENG sensor was directly over the bottom part. The tape was clamped, and then welded to each tab individually using the aforementioned welding parameters. The completed build of a single sensor pocket design, named sensor B, is shown in Figure 4.4 (a).

In creating the metal-matrix for the pocket design sensor array, two pockets were built and separated by a welded section of 5 tape layers of AL3003. The completed build for the pocket design sensor array, named sensor C and sensor D, can be seen in Figure 4.4 (b). During the welding process, the top part of the TENG sensor in sensors C and D became dislodged and was no longer adhered to the embedding AL3003 tape. Although not intended, this sensor damage during embedding could demonstrate the robustness of the sensor design.

4.5 Experimental Testing of TENG-AL3003 Composites

After fabrication of the TENG-AL3003 composites, the baseplates were removed from the Fabrisonic R220 machine to perform various testing. The three testing methods were: touch testing, solenoid testing, and drop testing. Touch testing was performed first in which a finger tapped the surface of metal-matrix above the TENG sensors to evaluate the embedded sensors with a simple-to-perform test. Next, the embedded sensors were characterized using solenoid testing, in which a solenoid actuator tapped the surface of the metal-matrix above the TENG sensors with various solenoid voltage amplitudes and actuation frequencies. Finally in drop testing, a golf ball was dropped onto the metal-matrix above the TENG sensors to evaluate the embedded sensors impact detection. The open circuit voltage of the TENG sensor was measured using a Siglent Technologies SDS1202X-E 200 MHz Digital Oscilloscope with a 1 M Ω impedance probe. The TENG sensors voltage output was not amplified or filtered by a circuit prior to connecting to the oscilloscope. The oscilloscope recorded the voltage data and saved it to a USB drive. The data files were then transferred to a

PC to plot and analyze the data using MATLAB. An estimated signal-to-noise ratio (SNR) analysis was performed for the sensor results. For touch testing and solenoid testing, the estimated SNR was the average voltage of the impulse peaks versus the RMS of the signal between the first and second peaks as the noise. For drop testing, the estimated SNR was the voltage of the first impulse peak indicating impact versus the RMS of the signal between the first and second peaks as the noise.

4.5.1 Touch Testing

In touch testing, a finger was used to tap the surface of the metal-matrix above the TENG sensor. The experimental setup for touch testing is shown in Figure 4.5.

Touch testing was performed for sensor B, the single sensor pocket design, and can be seen in Figure 4.6(a). The impulse peaks when contact was made, near 1.3 V in magnitude, are easily distinguishable from the noise. This observation is reinforced by the estimated SNR in Table 4.1 for sensor B, which is large in magnitude indicating sensor B is functional.

Touch testing for sensors C and D, the pocket design sensor array, was performed simultaneously and can be seen in Figure 4.6(b). Sensor C was connected to oscilloscope channel 2, and sensor D was connected to channel 1. Both sensors demonstrate large impulse peaks when respective contact is made. The impulse peaks for sensors C and D are around 0.5 V, which is less than the impulse peaks for sensor B. This observed difference could be indicative of the top part of the TENG sensor becoming dislodged during embedding, or it simply could be due to inaccuracies with the applied force during touch testing. However, both sensors have relatively large estimated SNRs, seen in Table 4.1. There is a negligible response in the sensor C signal when the sensor D signal has an impulse peak. Likewise, there is a negligible response in the sensor D signal when the sensor C signal has an impulse peak. These results indicate that the sensors could be used as a spatially-dependent sensor array, however, further tests would need to be performed. Although the top parts of the

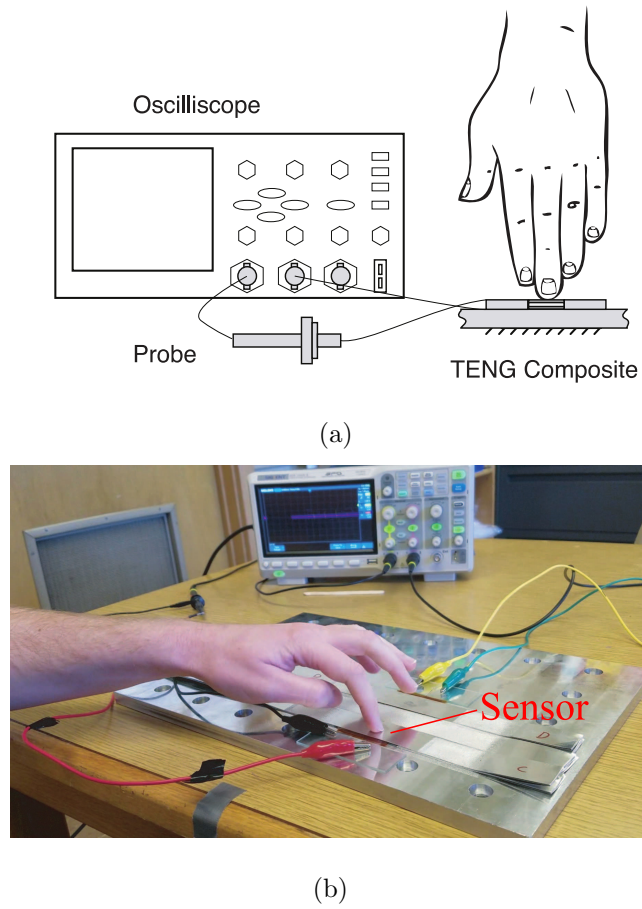


Figure 4.5. Experimental touch test setup: (a) schematic of test setup and (b) picture of test setup

TENG sensor were dislodged during embedding, both sensors C and D demonstrate functionality in touch testing.

Table 4.1. Estimated signal-to-noise ratio analysis for touch testing results from Figure 4.6.

Sensor	Average voltage of impulse peaks	RMS of noise	Ratio
Sensor B	1.296 V	0.0637 V	20.35
Sensor C	0.515 V	0.0158 V	32.59
Sensor D	0.579 V	0.0320 V	18.09
Sensor E	0.029 V	0.0036 V	8.14

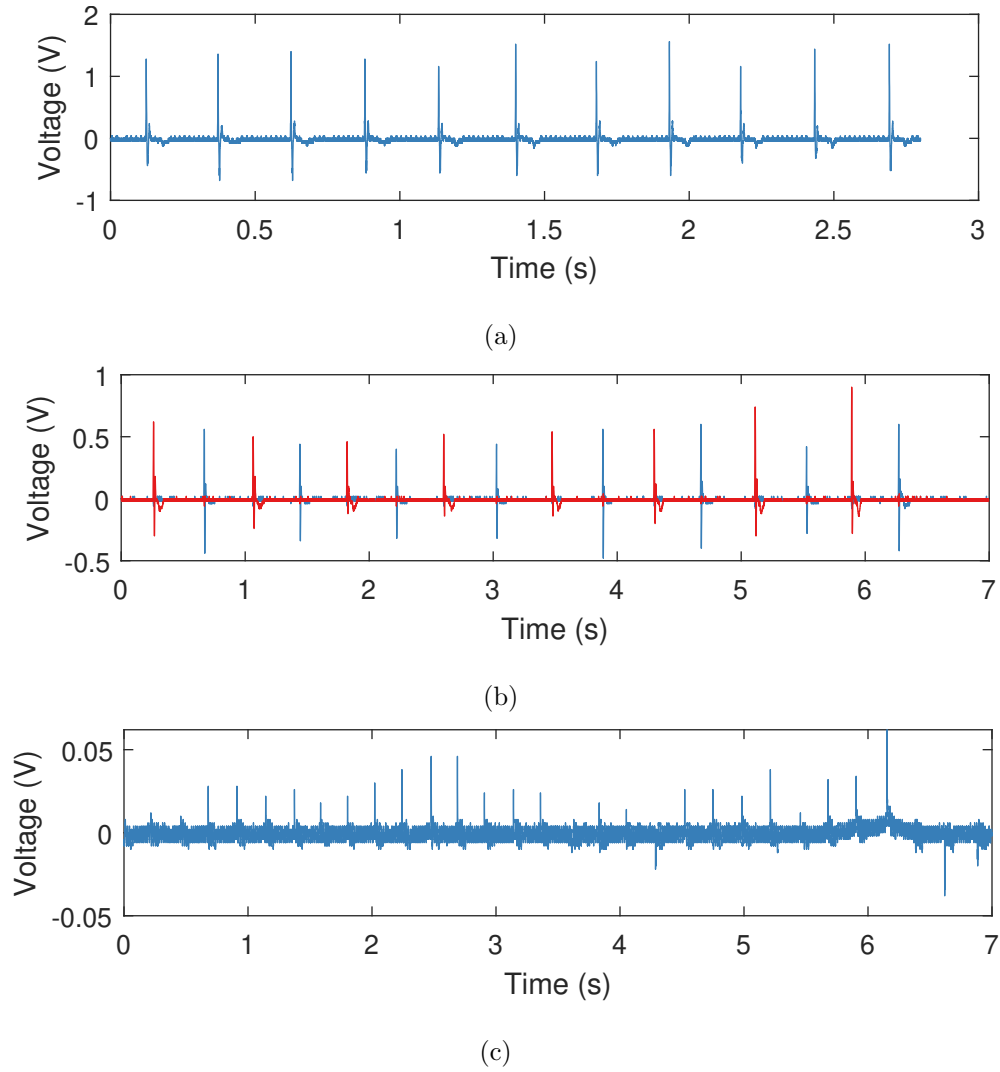


Figure 4.6. Touch testing results: (a) sensor B (pocket design) touch test response, (b) sensors C and D (pocket design sensor array) touch test responses, and (c) sensor E (channel design) touch test response.

Touch testing for sensor E, the single sensor channel design, to repeated finger tapping can be seen in Figure 4.6(c). Sensor E can detect finger tapping, however, the impulse peaks are around 30 mV. Additionally, the estimated SNR is much lower than those for sensors B, C and D, seen in Table 4.1. Thus, the channel design appears to be much less sensitive than the pocket design to applied loads.

Note that pressing on the surface of the metal-matrix above the TENG sensor causes the contact of the two dielectric surfaces. This results in a positive spike followed by a negative spike during recoil. The positive spike dissipates because once the contact between top and bottom parts is established, the voltage diminishes due to the finite input resistance of the probe.

4.5.2 Solenoid Testing

For solenoid testing, a solenoid actuator was mounted to an 80/20 frame and the frame clamped to a table. The embedded TENG sensor was then placed underneath the plunger, so the plunger could impact the metal-matrix above the center of the TENG sensor. The experimental setup for solenoid testing can be seen in Figure 4.7. The solenoid actuation waveform, which was a square-wave, was controlled with an Arduino and a 30 V power supply. Since the TENG sensors are sensitive to charge, a plastic cap was attached to the solenoid actuator plunger because the plunger was metal. The solenoid testing parameters that were used for sensor characterization are listed in Table 4.2.

Table 4.2. Parameter list for solenoid testing

Parameters	Value
Voltage Amplitude	5, 7.5, 10 V
Frequency	1, 2.5, 5 Hz

After reaching the desired solenoid parameters for a test, the oscilloscope recorded approximately 10 taps of the solenoid plunger for the various actuation frequencies. Figure 4.8 contains example plots of the experimental results for sensors C, D, and E, to solenoid actuation at 5 V input amplitude and 1 Hz frequency. Sensor B was not tested due to its similar response to sensors C and D during touch testing. For sensors C and D, the impact of the solenoid with the aluminum matrix directly above the respective sensors is easily distinguishable from noise, seen in Figure 4.8(a) and

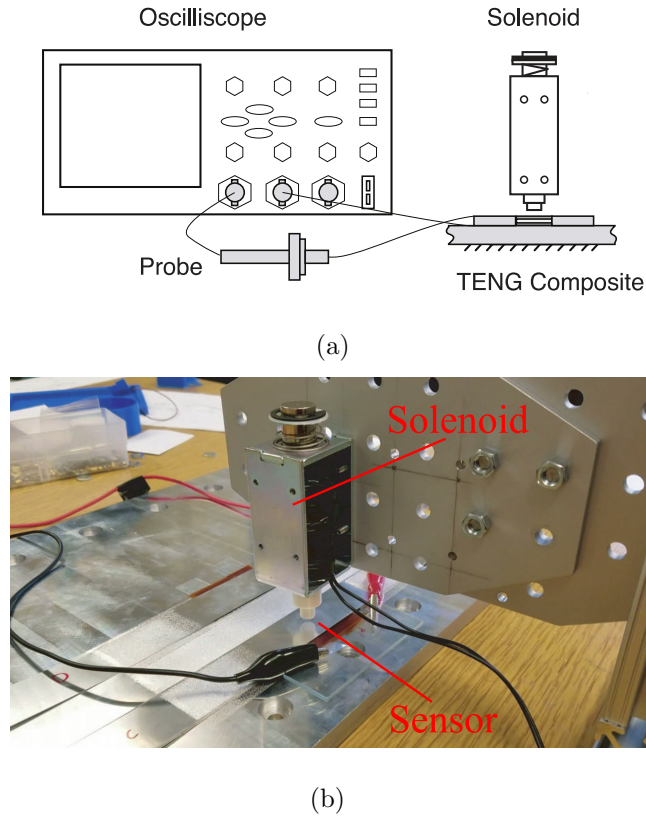


Figure 4.7. Experimental solenoid test setup: (a) schematic of test setup and (b) picture of test setup

Figure 4.8(b). In agreement, sensors C and D have a relatively large estimated SNR, seen in Table 4.3. The results from sensor E are extremely noisy, seen in Figure 4.8(c). The RMS noise for sensor E during the solenoid test is much larger in magnitude than during the touch test, seen in Table 4.3. This increase in RMS noise is attributed to the solenoid and power supply electromagnetically interacting with the sensor. Based on touch testing results, the sensor E output voltage is too small to distinguish from the increased signal noise during solenoid testing.

These tests were repeated using the other solenoid input parameters, listed in Table 4.2, for sensor characterization to solenoid voltage amplitude and actuation frequency. The solenoid voltage amplitude was assumed to be proportional to applied load. The raw data for solenoid testing of sensors C, D, and E can be seen in Appendix

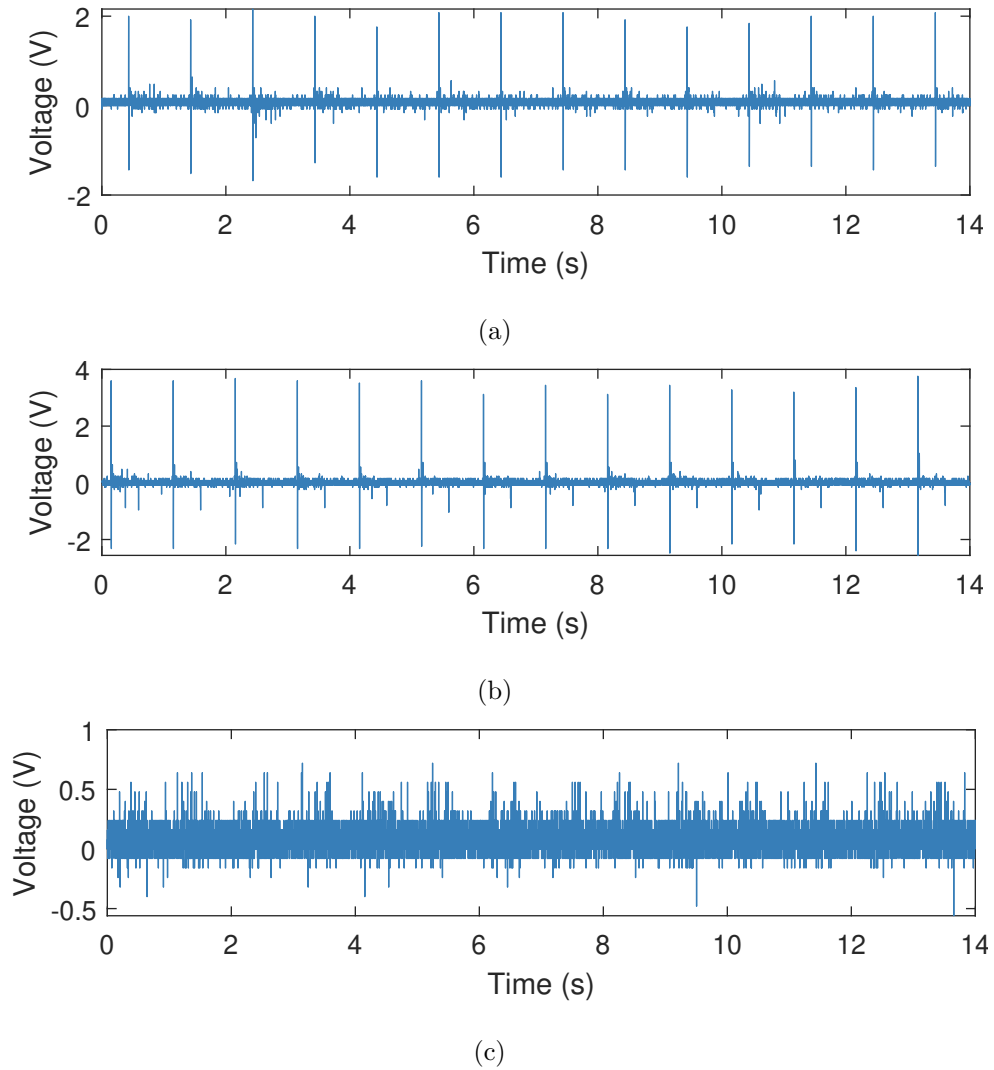
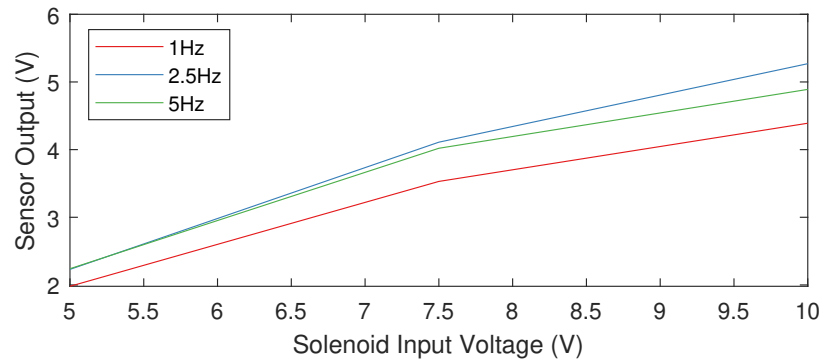


Figure 4.8. Preliminary solenoid testing results: (a) sensor C (pocket design) response to 5 V and 1 Hz solenoid actuation, (b) sensor D (pocket design) response to 5 V and 1 Hz solenoid actuation, and (c) sensor E (channel design) response to 5 V and 1 Hz solenoid actuation.

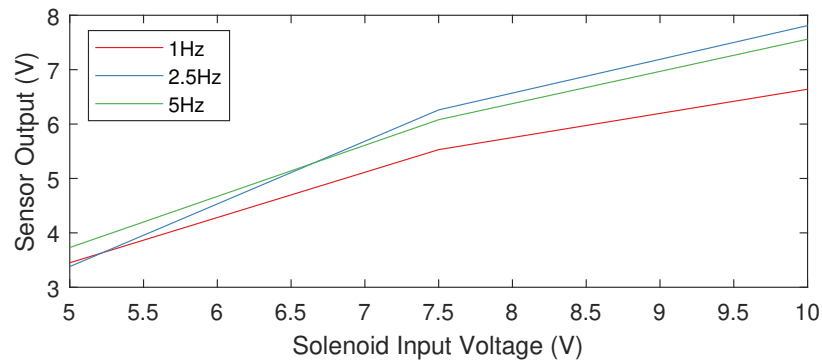
C. Seen in Figure 4.9, as the solenoid voltage amplitude increases, i.e. as the force increases, the output voltage impulse peaks also increase in magnitude for sensors C and D. The increase in sensor output voltage with respect to solenoid voltage amplitude appears to be nearly linear, although there is likely some saturation if the solenoid voltage amplitude was increased further. There is little correlation between frequency and sensor output voltage, although from Figure 4.9, there does seem to be

Table 4.3. Estimated signal-to-noise ratio analysis for preliminary solenoid testing (5 V, 1 Hz) from Figure 4.8.

Sensor	Average voltage of impulse peaks	RMS of noise	Ratio
Sensor C	2.013 V	0.1092 V	18.43
Sensor D	3.424 V	0.1058 V	32.36
Sensor E	N/A	0.1342 V	N/A



(a)



(b)

Figure 4.9. Calibration of the average impulse peaks of the sensor output voltage to the solenoid input voltage: (a) sensor C and (b) sensor D.

a decrease in the variance of sensor output voltage as the frequency increases. Overall, the pocket design sensor output has a nearly linear relationship with solenoid voltage amplitude, or applied load, and little to no dependence on frequency.

4.5.3 Drop Testing

In drop testing, a golf ball was dropped from a height of 33 in and impacted with the surface of the metal-matrix above the TENG sensor. The golf ball was guided by a plastic tube with a diameter of approximately 2 in. The experimental setup is shown in Figure 4.10. The experimental drop test results for sensors C, D, and E,

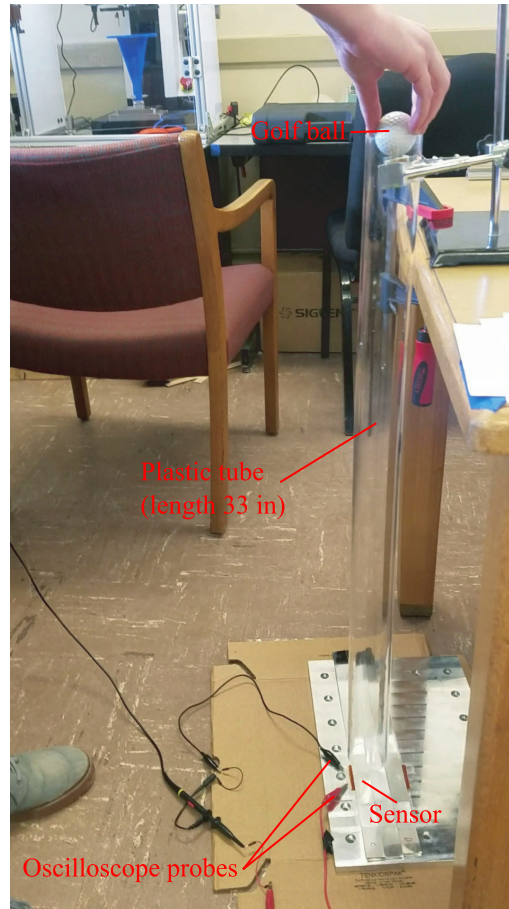


Figure 4.10. Experimental drop test setup

are displayed in Figure 4.11.

For both sensors C and D, there is a large initial impulse peak in the sensor output voltage as the golf ball impacts the surface of the metal-matrix. The subsequent impulse peaks are attributed to the golf ball repeatedly bouncing on the surface. The second impulse peak due to the second bounce is about the same size as the

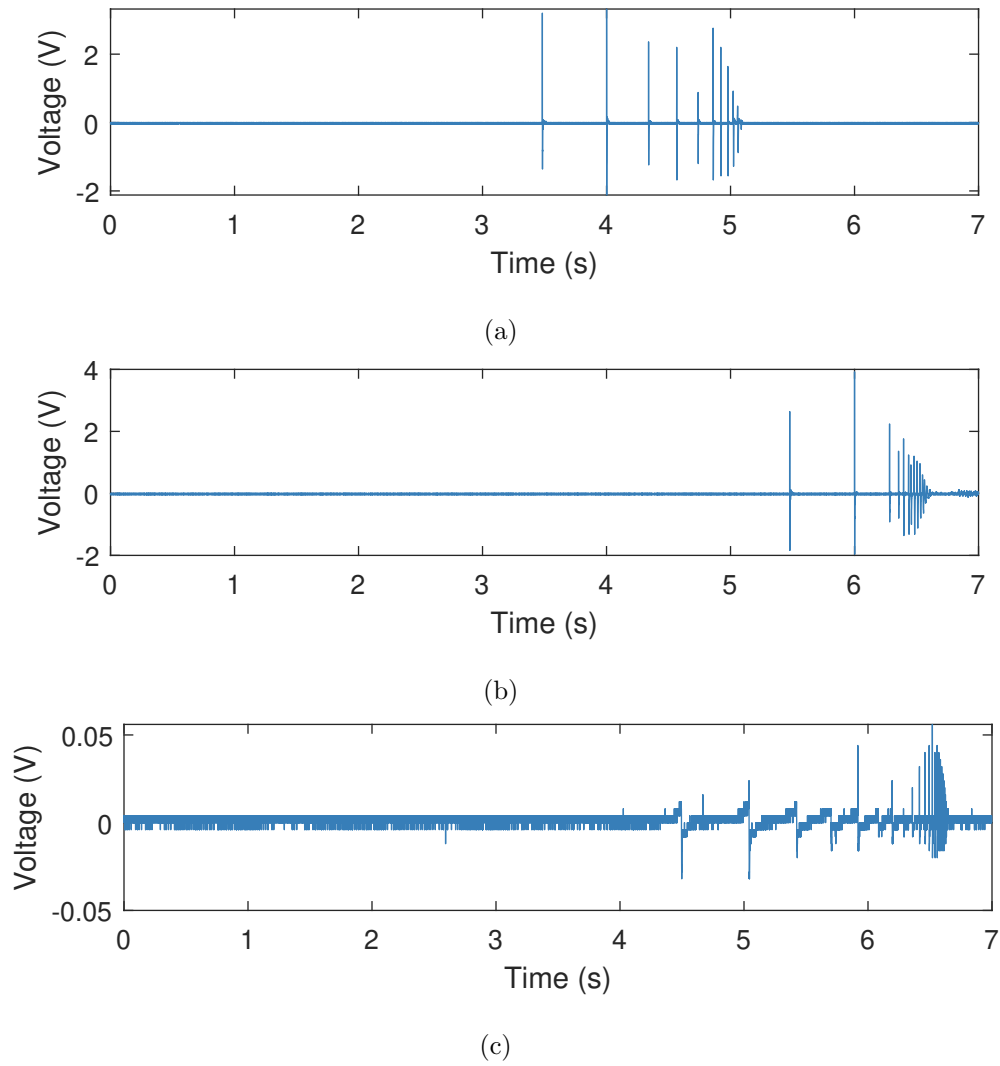


Figure 4.11. Drop testing results: (a) sensor C (pocket design) drop test response, (b) sensor D (pocket design) drop test response, and (c) sensor E (channel design) drop test response.

impulse peak from the first bounce. This contradictory observation is attributed to the golf ball impacting the metal-matrix above the sensor in a different spot with each bounce. Therefore, an analysis of the magnitude of each peak is unlikely to produce meaningful results. What is interesting is how many bounces the sensors record. The sensors seem to detect the golf ball bouncing until cessation, which indicates that

the sensors can detect small applied load. Additionally, both sensors C and D have large estimated SNRs, seen in Table 4.4.

Table 4.4. Estimated signal-to-noise ratio analysis for drop testing results from Figure 4.11.

Sensor	First impulse voltage	RMS of noise	Ratio
Sensor C	3.20 V	0.0285 V	112.28
Sensor D	2.64 V	0.0301 V	87.71
Sensor E	0.044 V	0.0033 V	13.33

Because of the low output voltage from sensor E, it is not entirely obvious in Figure 4.11(c) which impulse peak is the impact of the golf ball. However, we assumed that the golf ball impacts the metal-matrix above the sensor at approximately 6 seconds. The impact response for sensor E is similar to those for sensors C and D, but at a much lower voltage. From Table 4.4, Sensor E has an estimated SNR smaller than sensors C and D. However, the estimated SNR is large enough that this design could be feasible as an impact sensor if the time of impact is more easily distinguishable. All drop test results indicate that the embedded TENG sensors can detect impacts, although the results from sensors C and D indicate that the pocket design is more reliable in detecting an impact from an external object.

4.6 Summary

TENGs are useful as an embedded sensor because the materials are inexpensive and flexible, and the sensor output is a simple voltage measurement. Two sensor designs were developed: a channel design and a pocket design. The TENG sensors are made of ITO/PET sheets and Kapton tape. The TENG sensors were embedded in AL3003 metal-matrix using a Fabrisonic R220 UAM machine. Three sensor systems were fabricated: a single sensor channel design, a single sensor pocket design, and a pocket design sensor array. The single sensors were used to determine the efficacy of

the design, and the sensor array was used to demonstrate that a spatially-dependent array could be created. Testing was performed using touch testing, a solenoid testing, and drop testing. Implementation of an embedded TENG sensor is easier with the channel design, but the embedded sensor output voltage is low. The pocket design requires more work to fully embed the sensor, but the embedded sensor output voltage is high. Both of the current designs were functional after embedding, however, the pocket design is more viable for use as an embedded sensor for detecting contact or impact to the metal-matrix from an external object.

5. CONCLUDING REMARKS

5.1 Summary

The objectives of this research was to develop a multi-modal model to explore the effect of the dynamic interaction between the substrate and sonotrode on the substrate modes of vibration during the entire weld cycle, and to develop an inexpensive, flexible embedded sensor in a metal-matrix via UAM that is capable of detecting contact or impact to the metal-matrix composite. In answering the first objective, a 3-D dynamic multi-modal model of the substrate during the UAM process was developed to explore resonant interactions between the substrate and sonotrode. The development of the model was broken into two steps, first the free vibration solution of the substrate was determined through a Galerkin approximation, and second the forced response due to substrate-sonotrode interaction was determined through modal decomposition. The interaction between the sonotrode and substrate is described using three different forcing models, which approximated the interfacial friction between the foil and substrate induced by sonotrode excitation and compression. After deriving the semi-analytical model, the transverse velocity response was simulated for various heights, or height-to-width ratios, to study the transverse dynamic compliance of the substrate. In studying the model results, a few observations can be made: the model results qualitatively match with trends in the experimental results; the dominant mode in the substrate response changes as the height increases; the excited modes of vibration are cut on and off during a weld cycle as the sonotrode travels across the length of the substrate; and the three forcing models appear to have little impact on the height and weld cycle trends of the substrate response. With the knowledge developed from this model, new control schemes could potentially be

developed, and welding paths could be intelligently planned to minimize problematic modes of vibration at particular substrate heights.

In addressing the second objective, triboelectric nanogenerators (TENGs) were embedded in an AL3003 metal-matrix fabricated on a Fabrisonic R220 UAM machine. Two TENG sensor designs were developed and implemented in single sensor format. Additionally, one sensor design was implemented in a sensor array. The embedded sensors detected contact and impact to the surface of the metal-matrix. The experimental results indicate that the sensors could be used to create a spatially-dependent array. Additionally, the embedded sensors were characterized using a solenoid actuator to contact the surface of the metal-matrix. One sensor design was unsuitable to solenoid characterization due to low output voltage combined with signal noise induced by the solenoid. However, the other sensor design has a consistent nearly linear relationship between output voltage and dynamically applied load over a frequency range of 1-5 Hz. The proof-of-concept composites created in this work could be used to develop embedded sensors to detect explosive fragmentation or shockwaves. For example, a spatially-dependent sensor array could be used to determine the relative location of the detonation.

5.2 Contributions

From this work, several advances in the understanding of substrate-sonotrode dynamic interactions have been made, as well as the fabrication of a novel smart metal-matrix composite via UAM. These advances are:

- Higher-order modes cannot be ignored in the development of dynamic models of the substrate during the UAM process, especially at substrate heights greater than the critical height-to-width ratio.
- Excitation of multiple modes of vibration during a weld cycle requires consideration of modeling the entire weld cycle.

- Provided a prediction of problematic substrate heights at a wider range of height-to-width ratios.
- An explanation was provided, although limited, into the bond degradation seen at the critical height-to-width ratio for substrate width of 0.5 in.
- Triboelectric nanogenerators are embedded in a metal-matrix via UAM for the first time .
- Demonstrated the efficacy of TENGs to be utilized as embedded contact or impact sensors in a metal-matrix.

5.3 Future Work

Although contributions have been made to the understanding of substrate dynamics during a weld cycle, further experimental tests need to be performed to validate these claims. This could be accomplished through monitoring the substrate response or measuring the relative velocity of the foil-substrate interface directly underneath the sonotrode for a wider range of height-to-width ratios during a weld cycle. Currently, the developed model cannot predict the quality of bonding, just that bonding is unlikely to occur at certain heights due to an increase in transverse dynamic compliance. In order to characterize bond quality, an energy based model, similar to [11], should be added. This would require that the slip between the foil and substrate be directly simulated rather than using an approximation of the interfacial friction waveform for varying degrees of differential motion. Additionally, a constant coefficient of friction at the foil-substrate interface is likely not realistic [8, 28]. Replacing the constant coefficient of friction with one that is dependent upon state or relative velocity between foil and substrate, similar to [67], will provide a more accurate characterization of the foil-substrate interfacial friction. Additionally, the state-dependent coefficient of friction could introduce instability in the substrate response, similar to brake squeal [68, 69], thus providing a more complete explanation of the bond de-

gration at the critical height-to-width ratio for a substrate width of 0.5 in. Finally, the forcing was modeled as a moving line load, when in reality the sonotrode would impose a contact patch, similar to the Hertzian contact patch in [17]. Introducing a contact patch could allow for additional considerations into uneven stick-slip motion at the foil-substrate interface. With these changes to the current model and further experimental validation, the substrate model could be combined with a model of the welder system, similar to [36] and [37], to create a novel control scheme for the UAM system.

Although the current embedded TENG sensors are considered a success, further improvements to the design and testing need to be performed. The two main weaknesses are in the fabrication process. The TENG sensors were manufactured using manual processes such as cutting with scissors. Using an automated process, such as laser cutting, can improve dimensional accuracy and allow the fabrication of smaller TENG sensors to fully realize the intended uses. The second weakness is in the fabrication of the metal-matrix. The Fabrisonic R220 UAM machine is a test-bed system and does not include the subtractive processes of the new commercial systems, like the Fabrisonic SonicLayer[®] 4000. With a milling step included in the fabrication process, fully embedding the pocket sensor design can be completed by milling a pocket in the baseplate, then placing the sensor in the pocket, and welding a foil directly over the pocket. Further sensor characterization to directly correlate applied load to sensor output voltage is needed. From our testing, we know that the sensors are useful in determining whether contact was made, but with a more thorough characterization the sensors output voltage can be used for measurements rather than just sensing. With a better sensor characterization, a spatially-dependent sensor array that can correlate sensor voltage output into a determination of an explosive detonation location can be developed. Additionally, the two objectives could be connected by utilizing the novel control scheme of the UAM system to mitigate problematic height-to-width ratios when building a composite.

REFERENCES

- [1] D. White. Ultrasonic consolidation of aluminum tooling. *Advanced Materials & Processes*, 161(1):64–65, 2003.
- [2] Fabrisonic LLC. Who are we? <https://fabrisonic.com/company>. Accessed: 04-08-2020.
- [3] Fabrisonic LLC. Gradient material solutions. <https://fabrisonic.com/gradient-material-solutions/>. Accessed: 04-14-2020.
- [4] R.R. Dehoff and S.S. Babu. Characterization of interfacial microstructures in 3003 aluminum alloy blocks fabricated by ultrasonic additive manufacturing. *Acta Materialia*, 58(13):4305–4315, 2010.
- [5] M.R. Sriraman, H. Fujii, M. Gonser, S.S. Babu, and M. Short. Bond characterization in very high power ultrasonic additive manufacturing. In *2010 International Solid Freeform Fabrication Symposium*, Austin, TX, 2010.
- [6] S. Shimizu, H.T. Fujii, Y.S. Sato, H. Kokawa, M.R. Sriraman, and S.S. Babu. Mechanism of weld formation during very-high-power ultrasonic additive manufacturing of al alloy 6061. *Acta Materialia*, 74:234–243, 2014.
- [7] G.D. Janaki Ram, C. Robinson, and B.E. Stucker. Use of ultrasonic consolidation for fabrication of multi-material structures. *Rapid Prototyping Journal*, 13(4):226–235, 2007.
- [8] A. Siddiq and E. Ghassemieh. Thermomechanical analyses of ultrasonic welding process using thermal and acoustic softening effects. *Mechanics of Materials*, 40(12):982–1000, 2008.
- [9] A. Siddiq and T.E. Sayed. A thermomechanical crystal plasticity constitutive model for ultrasonic consolidation. *Computational Materials Science*, 51(1):241–251, 2012.
- [10] G.S. Kelly. *A thermo-mechanical finite element analysis of acoustic softening during ultrasonic consolidation of aluminum foils*. Master’s thesis, University of Delaware, 2012.
- [11] G.S. Kelly, S.G. Advani, J.W. Gillespie, and T.A. Bogetti. A model to characterize acoustic softening during ultrasonic consolidation. *Journal of Materials Processing Technology*, 213(11):1835–1845, 2013.
- [12] Q. Mao. *Understanding the Bonding Process of Ultrasonic Additive Manufacturing*. PhD thesis, Clemson University, 2017.
- [13] F. Blaha and B. Langenecker. Dehnung von zink-kristallen unter ultraschalleinwirkung. *Naturwissenschaften*, 42(20):556, 1955.

- [14] B. Langenecker. Effect of ultrasound on deformation characteristics of metals. *IEEE Transactions on Sonics and Ultrasonics*, 13(1):1–8, 1966.
- [15] H.P.C. Daniels. Ultrasonic welding. *Ultrasonics*, 3(4):190–196, 1965.
- [16] C. Robinson, C. Zhang, G.D. Janaki Ram, E.J. Siggard, B.E Stucker, and L. Li. Maximum height to width ratio of freestanding structures built using ultrasonic consolidation. In *2006 International Solid Freeform Fabrication Symposium*, Austin, TX, 2006.
- [17] J.M. Gibert. *Dynamics of Ultrasonic Consolidation*. PhD thesis, Clemson University, 2009.
- [18] D.R. Foster, G.A. Taber, S.S. Babu, and G.S. Daehn. In situ velocity measurements of very high power ultrasonic additive manufacturing using a photonic doppler velocimeter. *Science and Technology of Welding and Joining*, 19(2):157–163, 2013.
- [19] Y. Lu, H. Song, G.A. Taber, D.R. Foster, G.S. Daehn, and W. Zhang. In-situ measurement of relative motion during ultrasonic spot welding of aluminum alloy using photonic doppler velocimetry. *Journal of Materials Processing Technology*, 231:431–440, 2016.
- [20] I. Gibson, D.W. Rosen, and B. Stucker. *Additive Manufacturing Technologies: Rapid Prototyping to Direct Digital Manufacturing*. Springer, New York, 2010.
- [21] M.R. Sriraman, M. Gonser, H.T. Fujii, S.S. Babu, and M. Bloss. Thermal transients during processing of materials by very high power ultrasonic additive manufacturing. *Journal of Materials Processing Technology*, 211(10):1650–1657, 2011.
- [22] J. Riemenschneider, R. Mitkus, and S. Vasista. Integration of actuations by additive layer manufacturing. In *ASME 2017 Conference on Smart Materials, Adaptive Structures and Intelligent Systems. Volume 2: Modeling, Simulation and Control of Adaptive Systems; Integrated System Design and Implementation; Structural Health Monitoring*, Snowbird, UT, 2017.
- [23] D. White. Ultrasonic Object Consolidation, U.S. Patent 6 519 500 B1, Feb. 2003.
- [24] M. Norfolk (Fabrisonic LLC). Not ALL 3D Printers Use Powder. <https://fabrisonic.com/3dprinting-no-powder/>, 2018, (Accessed: 04-28-2020).
- [25] C. Huang and E. Ghassemieh. 3D coupled thermomechanical finite element analysis of ultrasonic consolidation. *Materials Science Forum*, 539-543:2651–2656, 2007.
- [26] C. Zhang and L. Li. A friction-based finite element analysis of ultrasonic consolidation. *Welding Journal*, 87(7):187s–194s, 2008.
- [27] A. Siddiq and E. Ghassemieh. Theoretical and FE analysis of ultrasonic welding of aluminum alloy 3003. *Journal of Manufacturing Science and Engineering (Transactions of the ASME)*, 131(4):041007 (11), 2009.
- [28] S. Koellhoffer, J.W. Gillespie, S.G Advani, and T.A Bogetti. Role of friction on the thermal development in ultrasonically consolidated aluminum foils and composites. *Journal of Materials Processing Technology*, 211(11):1864–1877, 2011.

- [29] D. Pal and B.E. Stucker. Modelling of ultrasonic consolidation using a dislocation density based finite element framework: In this paper a dislocation density based constitutive model is developed and implemented into a crystal plasticity quasi-static finite element. *Virtual and Physical Prototyping*, 7(1):65–79, 2012.
- [30] S. Zhang, D. Yi, H. Zhang, L. Zheng, Y. Zhang, Z. Yang, and M. Norfolk. Towards understanding of ultrasonic consolidation process with “process map”. *Rapid Prototyping Journal*, 21(4):461–468, 2015.
- [31] G.S. Kelly, S.G. Advani, and J.W. Gillespie. A model to describe stick–slip transition time during ultrasonic consolidation. *The International Journal of Advanced Manufacturing Technology*, 79:1931–1937, 2015.
- [32] C. Zhang and L. Li. A study of static and dynamic mechanical behavior of the substrate in ultrasonic consolidation. In *2006 International Solid Freeform Fabrication Symposium*, Austin, TX, 2006.
- [33] C. Zhang and L. Li. Effect of substrate dimensions on dynamics of ultrasonic consolidation. *Ultrasonics*, 50(8):811–823, 2010.
- [34] J.M. Gibert, E.M Austin, and G. Fadel. Effect of height to width ratio on the dynamics of ultrasonic consolidation. *Rapid Prototyping Journal*, 16(4):284–294, 2010.
- [35] J.M. Gibert, G. Fadel, and M.F. Dagaq. On the stick-slip dynamics in ultrasonic additive manufacturing. *Journal of Sound and Vibration*, 332(19):4680–4695, 2013.
- [36] A. Hehr. *Process Control and Development for Ultrasonic Additive Manufacturing with Embedded Fibers*. PhD thesis, The Ohio State University, 2016.
- [37] A. Hehr and M.J. Dapino. Dynamics of ultrasonic additive manufacturing. *Ultrasonics*, 73:49–66, 2017.
- [38] C.Y. Kong and R.C. Soar. Fabrication of metal–matrix composites and adaptive composites using ultrasonic consolidation process. *Materials Science & Engineering*, 412(1):12–18, 2005.
- [39] Y. Yang, G.D. Janaki Ram, and B.E. Stucker. Bond formation and fiber embedment during ultrasonic consolidation. *Journal of Materials Processing Technology*, 209(10):4915–4924, 2009.
- [40] D. Li and R.C. Soar. Characterization of process for embedding SiC fibers in Al 6061 O matrix through ultrasonic consolidation. *Journal of Engineering Materials and Technology*, 131(2):021016–1–021016–6, 2009.
- [41] Y. Yang, B.E. Stucker, and G.D. Janaki Ram. Mechanical properties and microstructures of SiC fiber-reinforced metal matrix composites made using ultrasonic consolidation. *Journal of Composite Materials*, 44(26):3179–3194, 2010.
- [42] H. Guo, M.B. Gingerich, L.M. Headings, R. Hahnlen, and M.J. Dapino. Joining of carbon fiber and aluminum using ultrasonic additive manufacturing (UAM). *Composite Structures*, 208:180–188, 2019.

- [43] C.Y. Kong, R.C. Soar, and P.M. Dickens. Ultrasonic consolidation for embedding SMA fibres within aluminium matrices. *Composite Structures*, 66(1):421–427, 2004.
- [44] R.J. Friel and R.A. Harris. A nanometre-scale fibre-to-matrix interface characterization of an ultrasonically consolidated metal matrix composite. *Proceedings of the Institution of Mechanical Engineers, Part L: Journal of Materials Design and Applications*, 224(1):31–40, 2009.
- [45] P.J. Wolcott, C.D. Hopkin, L. Zhang, and M.J. Dapino. Smart switch metamaterials for multiband radio frequency antennas. *Journal of Intelligent Material Systems and Structures*, 22(13):1469–1478, 2011.
- [46] P. Evans, R. Hahnlen, M. Dapino, and J. Pritchard. Dimensionally stable optical metering structures with NiTi composites fabricated through ultrasonic additive manufacturing. In *ASME 2013 Conference on Smart Materials, Adaptive Structures and Intelligent Systems. Volume 1: Development and Characterization of Multifunctional Materials; Modeling, Simulation and Control of Adaptive Systems; Integrated System Design and Implementation*, Snowbird, UT, 2013.
- [47] R. Hahnlen and M.J. Dapino. NiTi–Al interface strength in ultrasonic additive manufacturing composites. *Composites Part B*, 59:101–108, 2014.
- [48] M.J. Dapino. Smart structure integration through ultrasonic additive manufacturing. In *ASME 2014 Conference on Smart Materials, Adaptive Structures and Intelligent Systems. Volume 2: Mechanics and Behavior of Active Materials; Integrated System Design and Implementation; Bioinspired Smart Materials and Systems; Energy Harvesting*, Newport, RI, 2014.
- [49] A. Hehr and M.J. Dapino. Interfacial shear strength estimates of NiTi–Al matrix composites fabricated via ultrasonic additive manufacturing. *Composites Part B*, 77:199–208, 2015.
- [50] J.J. Scheidler and M.J. Dapino. Stiffness tuning of FeGa structures manufactured by ultrasonic additive manufacturing. In *SPIE 9059, Industrial and Commercial Applications of Smart Structures Technologies 2014*, 2014.
- [51] T. Monaghan, A. Capel, S. Christie, R. Harris, and R. Friel. Solid-state additive manufacturing for metallized optical fiber integration. *Composites Part A: Applied Science and Manufacturing*, 76:181–193, 2015.
- [52] C. Mou, P. Saffari, D. Li, K. Zhou, L. Zhang, R. Soar, and I. Bennion. Smart structure sensors based on embedded fibre bragg grating arrays in aluminium alloy matrix by ultrasonic consolidation. *Measurement Science and Technology*, 20(3):034013 (6pp), 2009.
- [53] J.J. Schomer, A. Hehr, and M. Dapino. Characterization of embedded fiber optic strain sensors into metallic structures via ultrasonic additive manufacturing. In *SPIE - The International Society for Optical Engineering, 9803*, 2016.
- [54] J.J. Schomer and M. Dapino. Smart structure integration through ultrasonic additive manufacturing. In *ASME 2017 Conference on Smart Materials, Adaptive Structures and Intelligent Systems. Volume 2: Modeling, Simulation and Control of Adaptive Systems; Integrated System Design and Implementation; Structural Health Monitoring*, Snowbird, UT, 2017.

- [55] A. Hehr, M. Norfolk, J. Wenning, J. Sheridan, P. Leser, P. Leser, and J. Newman. Integrating fiber optic strain sensors into metal using ultrasonic additive manufacturing. *JOM*, 70(3):315–320, 2018.
- [56] A. Hehr, M. Norfolk, J. Sheridan, M. Davis, P. Leser, W. Leser, and J. Newman. Spatial strain sensing using embedded fiber optics. *JOM*, 71(4):1528–1534, 2019.
- [57] D. Schick, S. Suresh Babu, D.R. Foster, M. Dapino, M. Short, and J.C. Lippold. Transient thermal response in ultrasonic additive manufacturing of aluminum 3003. *Rapid Prototyping Journal*, 17(5):369–379, 2011.
- [58] E.J. Siggard, A.S. Madhusoodanan, B.E. Stucker, and B. Eames. Structurally embedded electrical systems using ultrasonic consolidation (UC). In *17th Solid Freeform Fabrication Symposium*, 2006.
- [59] R. Hahnlen and M.J. Dapino. Performance and modeling of active metal-matrix composites manufactured by ultrasonic additive manufacturing. In *Volume 7979, Industrial and Commercial Applications of Smart Structures Technologies 2011*, San Diego, CA, 2011.
- [60] E.v.K. Hill. The vibrational response of the rectangular parallelepiped with completely stress-free boundaries. *Journal of the Acoustical Society of America*, 75(2):442–446, 1984.
- [61] A. Leissa and Z-D. Zhang. On the three-dimensional vibrations of the cantilevered rectangular parallelepiped. *Journal of the Acoustical Society of America*, 73(6):2013–2021, 1983.
- [62] V.K. Astashev and V.I. Babitsky. *Ultrasonic Processes and Machines: Dynamics, Control and Applications (Foundations of Engineering Mechanics)*. Springer-Verlag, New York, 1st edition, 2007.
- [63] F. Fan, Z. Tian, and Z.L. Wang. Flexible triboelectric generator! *Nano Energy*, 1(2):328–334, 2012.
- [64] A.F. Diaz and R.M. Felix-Navarro. A semi-quantitative tribo-electric series for polymeric materials: the influence of chemical structure and properties. *Journal of Electrostatics*, 62(4):277–290, 2004.
- [65] L. Lin, Y. Xie, S. Wang, W. Wu, S. Niu, X. Wen, and Z.L. Wang. Triboelectric active sensor array for self-powered static and dynamic pressure detection and tactile imaging. *ACS Nano*, 7(9):8266–8274, 2013.
- [66] G. Zhu, W.Q. Yang, T. Zhang, Q. Jing, J. Chen, Y.S. Zhou, P. Bai, and Z.L. Wang. Self-powered, ultrasensitive, flexible tactile sensors based on contact electrification. *Nano Letters*, 14(6):3208–3213, 2014.
- [67] E.J. Berger, C.M. Krousgrill, and F. Sadeghi. Stability of sliding in a system excited by a rough moving surface. *Journal of Tribology*, 119(4):672–680, 1997.
- [68] F. Chen, C. An Tan, and R.L. Quaglia. *Disk Brake Squeal: Mechanism, Analysis, Evaluation, and Reduction/Prevention*. SAE International, Pennsylvania, 2006.
- [69] A. Tuchinda. *Development of Validated Models for Brake Squeal Predictions*. PhD thesis, Imperial College London, 2003.

- [70] S.S. Rao. *Vibration of continuous systems*. John Wiley & Sons, Inc., Hoboken, N.J., 2007.

A. MODESHAPES

The mode shapes for the model presented herein this document at heights other than at the critical height-to-width ratio.

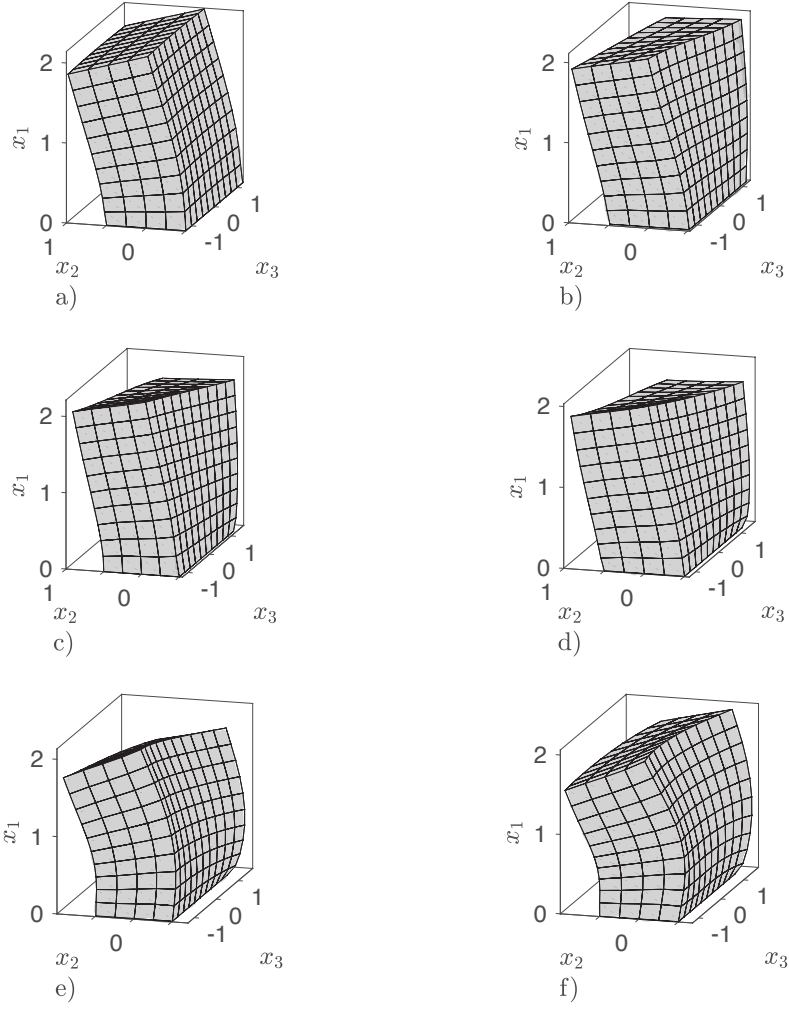


Figure A.1. First six modeshapes of dimension 2.0 in \times 1.0 in \times 2.5 with natural frequencies: a) $f_1 = 7182.97$ Hz, b) $f_2 = 11476.17$ Hz, c) $f_3 = 11611.02$ Hz, d) $f_4 = 25498.50$ Hz, e) $f_5 = 25597.53$ Hz, and f) $f_6 = 27992.99$ Hz

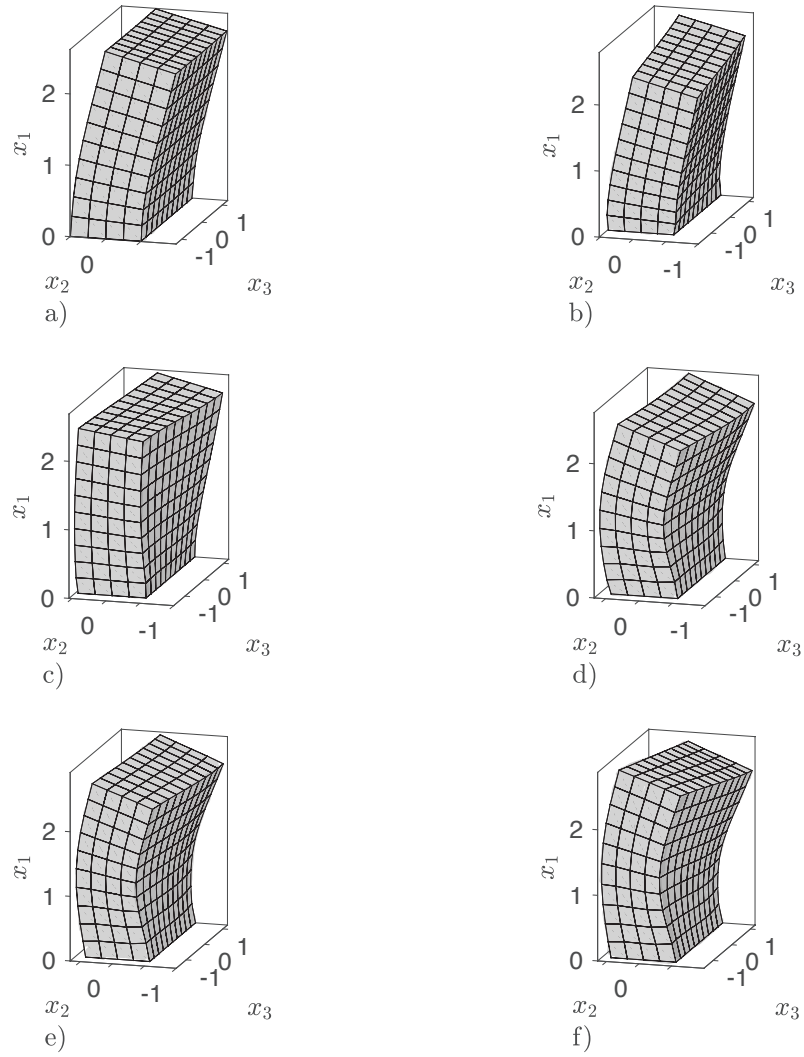


Figure A.2. First six modeshapes of dimension $2.5 \text{ in} \times 1.0 \text{ in} \times 2.5$ with natural frequencies: a) $f_1 = 4828.97 \text{ Hz}$, b) $f_2 = 8498.22 \text{ Hz}$, c) $f_3 = 9017.96 \text{ Hz}$, d) $f_4 = 19795.63 \text{ Hz}$, e) $f_5 = 20560.21 \text{ Hz}$, and f) $f_6 = 22613.99 \text{ Hz}$

B. MODEL VALIDATION

The semi-analytical model and the developed MATLAB simulation script is first validated by approximating a cantilevered Euler-Bernoulli beam with tip excitation. The solution to a cantilevered Euler-Bernoulli beam is known, and thus our semi-analytical model can be compared to a system with a known solution. Furthermore, the analytical convolution solution and Fourier series approximations to the forcing models are validated by simulating the response using ODE45 in MATLAB. ODE45 allows us to numerically solve the exact forcing functions without needing to approximate the forcing with a Fourier series. Using both Euler-Bernoulli approximation validation and ODE45 validation will provide us with good confidence in our model results.

B.1 Model Approximation of Euler-Bernoulli Beam Response

From [70], the governing equation for transverse vibration of a cantilevered Euler-Bernoulli beam is

$$EI \frac{\partial^4 w(x, t)}{\partial x^4} + \rho A \frac{\partial^2 w(x, t)}{\partial t^2} = f(x, t). \quad (\text{B.1})$$

The assumed solution for the cantilevered beam is

$$w(x, t) = \sum_{n=1}^{\infty} W_n(x) T_n(t), \quad (\text{B.2})$$

where $W_n(x)$ are the mass-normalized modes shapes and $T_n(t)$ are the time-dependent solution to the modal equation of motion for the n^{th} mode. From [70], the free vibration solution to Equation (B.1) is

$$W_n(x) = C_n (\cos(\beta_n x) - \cosh(\beta_n x)) - \frac{\cos(\beta_n L) + \cosh(\beta_n L)}{\sin(\beta_n L) + \sinh(\beta_n L)} (\sin(\beta_n x) - \sinh(\beta_n x)), \quad (\text{B.3})$$

where L is the length of the beam and the characteristic equation is $\cos(\beta L) \cosh(\beta L) = -1$. The mode shapes are mass-normalized to satisfy

$$\int_0^L \rho A W_n^2(x) dx = 1. \quad (\text{B.4})$$

Because an Euler-Bernoulli beam is 1-D and we are simulating transverse deflection, the line load for the analytical model from Equation (2.29) becomes

$$\bar{\mathbf{f}} = (f_2 \hat{\mathbf{e}}_2) \frac{1}{a} \delta\left(\alpha - \frac{a}{a}\right) \frac{2}{b} \delta(\eta) \frac{2}{c} \delta\left(\zeta - \frac{2}{c}\left(z_0 - \frac{s}{\Omega}\tau\right)\right). \quad (\text{B.5})$$

B.1.1 Pure Stick Forcing Euler-Bernoulli Beam Approximation

For pure stick forcing, the excitation waveform of f_2 is a sinusoid, thus the Euler-Bernoulli beam solution will be for a pure sine tip excitation. The tip force takes the form of

$$f(x, t) = \mu F_p \delta(x - L) \sin(\Omega t) \quad (\text{B.6})$$

The forced vibration solution using the assumed solution from Equation (B.2) to the tip force from Equation (B.6) is

$$T_n(t) = \frac{\mu F_p W_n(L)}{\omega_n} \left(\frac{-\Omega \sin(\omega_n t) + \omega_n \sin(\Omega t)}{\omega_n^2 - \Omega^2} \right). \quad (\text{B.7})$$

To approximate the Euler-Bernoulli tip force in our model, the forcing from Equation (B.5) becomes

$$\bar{\mathbf{f}} = (\mu F_p \sin(\tau) \hat{\mathbf{e}}_2) \frac{1}{a} \delta\left(\alpha - \frac{a}{a}\right) \frac{2}{b} \delta(\eta) \frac{2}{c} \delta\left(\zeta - \frac{2}{c}\left(z_0 - \frac{s}{\Omega}\tau\right)\right). \quad (\text{B.8})$$

Using this definition of the forcing, the response was simulated using the parameters listed in Table B.1. The velocity response was measured at $(\alpha = \frac{1}{\pi}, \eta = 0, \zeta = 0)$ and the response for the exact solution and the model approximation can be seen in Figure B.1. The model response closely matches the response for the exact solution for an Euler-Bernoulli beam. The response differs due to the slight differences in the natural frequencies and because there are modes present in the response that are not in an Euler-Bernoulli beam, i.e. the model is a 3-D parallelepiped and the Euler-Bernoulli beam exact solution is 1-D.

Table B.1. Parameter list of Euler-Bernoulli beam approximation for pure stick forcing

Parameters	Value
a	20 in
b	1 in
c	1 in
F_p	1000 lbf/in
μ	0.3
Ω	$2\pi \times (500)$ rad/s
λ_d	0
s	0 in/s
z_0	0

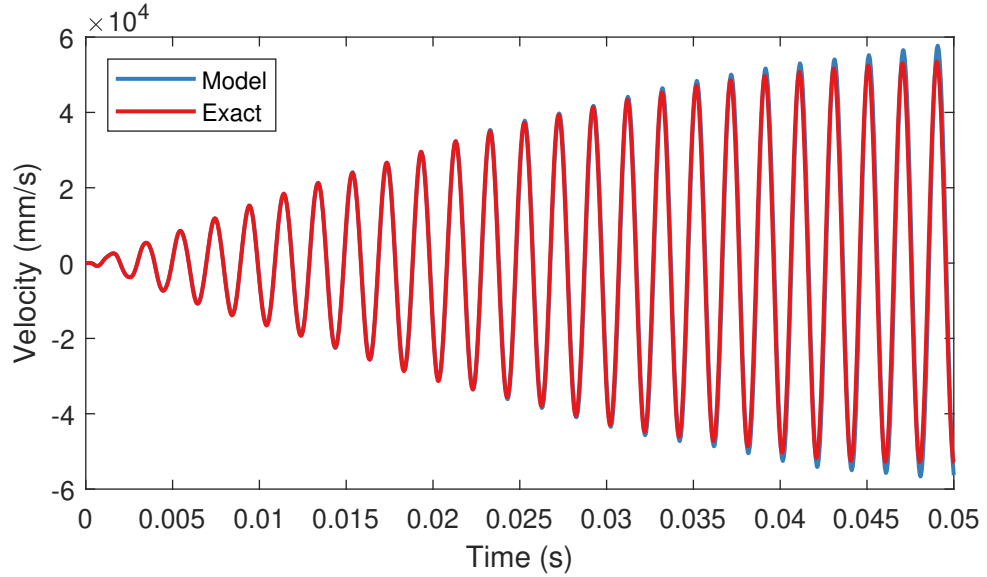


Figure B.1. Pure stick forcing model approximation compared to exact solution of Euler-Bernoulli beam vibration response.

B.1.2 Pure Slip Forcing Euler-Bernoulli Beam Approximation

For pure slip forcing, the waveform of the excitation is a cosinusoidal in nature. Therefore, the Euler-Bernoulli beam will be approximated with a pure cosine tip force. The tip force takes the form of

$$f(x, t) = \mu F_p \delta(x - L) \cos(\Omega t). \quad (\text{B.9})$$

The forced vibration solution to the tip force from Equation (B.9) is

$$T_n(t) = \frac{\mu F_p W_n(L)}{\omega_n} \left(\frac{\omega_n (\cos(\Omega t) - \cos(\omega_n t))}{\omega_n^2 - \Omega^2} \right). \quad (\text{B.10})$$

Because for pure slip forcing the f_2 component is approximated as a Fourier series, the pure cosine forcing is approximated as a one-term Fourier series. To approximate the Euler-Bernoulli tip force in our model, the forcing from Equation (B.5) becomes

$$\bar{\mathbf{f}} = (a_{2,1} \cos(\tau) \hat{\mathbf{e}}_2) \frac{1}{a} \delta\left(\alpha - \frac{a}{a}\right) \frac{2}{b} \delta\left(\eta\right) \frac{2}{c} \delta\left(\zeta - \frac{2}{c}\left(z_0 - \frac{s}{\Omega}\tau\right)\right), \quad (\text{B.11})$$

where $a_{2,1}$ is equal to μF_p . Using this definition of the forcing, the response was simulated using the parameters listed in Table B.2.

Table B.2. Parameter list of Euler-Bernoulli beam approximation for pure slip forcing

Parameters	Value
a	20 in
b	1 in
c	1 in
F_p	1000 lbf/in
μ	0.3
Ω	$2\pi \times (500)$ rad/s
λ_d	0
s	0
z_0	0

The velocity response was measured at ($\alpha = \frac{1}{\pi}$, $\eta = 0$, $\zeta = 0$) and is shown in Figure (B.2). The velocity response from the model matches well with the exact solution for the Euler-Bernoulli beam. There is a slight difference in the response which is attributed to small differences in the natural frequencies, and the model contains modes that are not in an Euler-Bernoulli beam because the model is 3-D whereas the Euler-Bernoulli beam exact solution is 1-D.

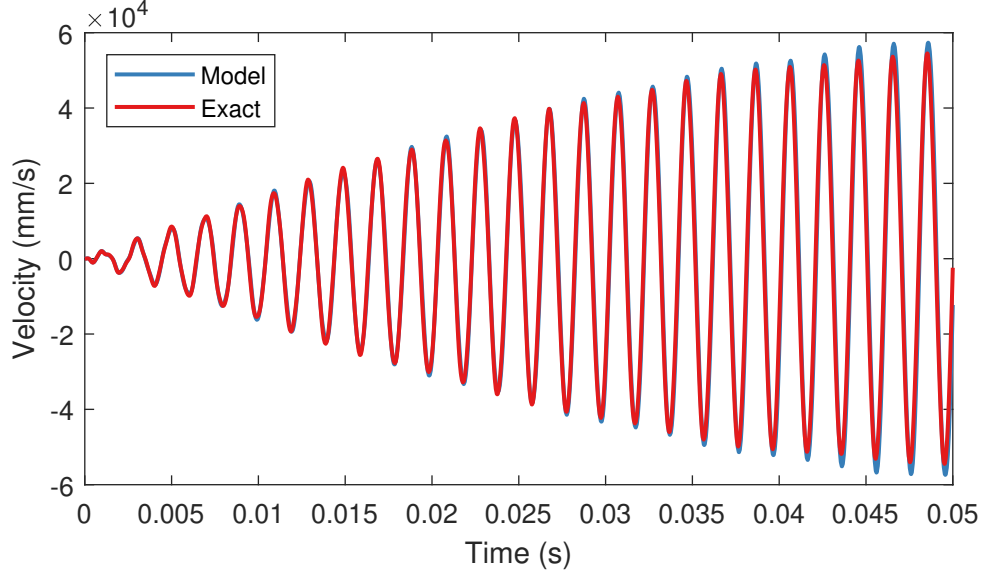


Figure B.2. Pure slip forcing model approximation compared to exact solution of Euler-Bernoulli beam vibration response.

B.1.3 Partial Slip Forcing Euler-Bernoulli Beam Approximation

For partial slip forcing, the excitation waveform is sinusoidal in nature, thus the Euler-Bernoulli beam solution will be for a pure sine tip excitation. The tip force is the same as Equation (B.6). The forced vibration solution is the same as Equation (B.7). Because the partial slip forcing components are approximated as a Fourier series, the pure sine tip excitation is approximated as a one-term Fourier series. The maximum frictional force in the pure slip forcing model is set to the amplitude of the pure sine wave. To approximate the Euler-Bernoulli tip force in our model, the forcing from Equation (B.5) becomes

$$\bar{\mathbf{f}} = (b_{2,1} \sin(\tau) \hat{\mathbf{e}}_2) \frac{1}{a} \delta\left(\alpha - \frac{a}{a}\right) \frac{2}{b} \delta\left(\eta\right) \frac{2}{c} \delta\left(\zeta - \frac{2}{c}\left(z_0 - \frac{s}{\Omega}\tau\right)\right), \quad (\text{B.12})$$

where $b_{2,1}$ is equal to μF_p . Using this definition of the forcing, the response was simulated using the parameters listed in Table B.3. The velocity response was measured at $(\alpha = \frac{1}{\pi}, \eta = 0, \zeta = 0)$ and is shown in Figure (B.3). Qualitatively the model response looks similar to the exact solution for the Euler-Bernoulli beam. Much like

Table B.3. Parameter list of Euler-Bernoulli beam approximation for partial slip forcing

Parameters	Value
a	20 in
b	1 in
c	1 in
F_p	1000 lbf/in
μ	0.3
Ω	$2\pi \times (500)$ rad/s
λ_d	0
s	0
z_0	0
maxF	300 lbf/in

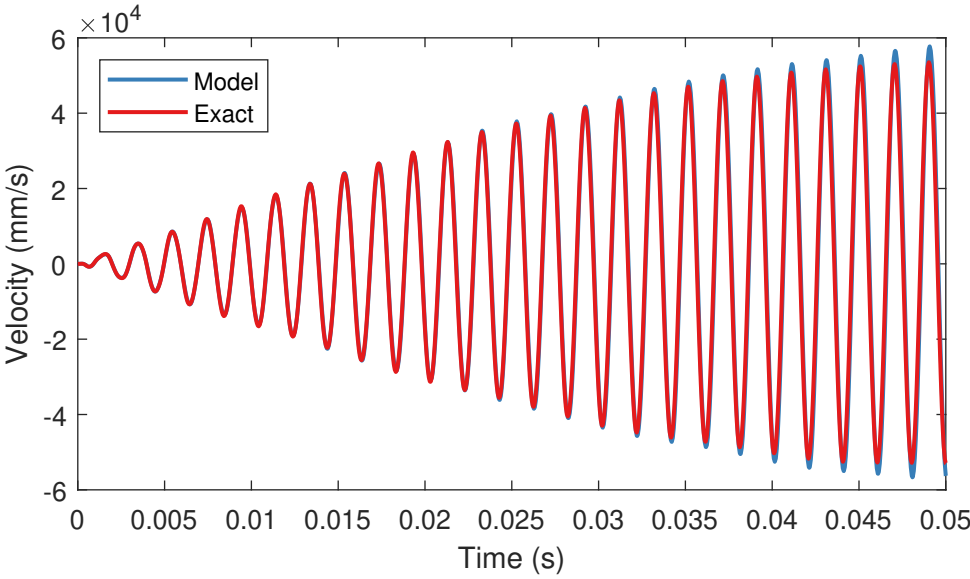


Figure B.3. Partial slip forcing model approximation compared to exact solution of Euler-Bernoulli beam vibration response.

pure stick and pure slip forcing, the exact solution response differs slightly from the model response due to the small differences in natural frequencies and the 3-D model contains modes not present in the 1-D exact solution of an Euler-Bernoulli beam.

The model and various forcing models can be simplified down to approximate an Euler-Bernoulli beam vibration response. This validation gives good confidence in the model and the developed code; however, additional validation is explored.

B.2 Code and Model Validation through ODE45 Comparison

After approximating an Euler-Bernoulli beam vibration response, the model and code was evaluated by using ODE45 to determine the response. ODE45 was used to numerically solve Equation (2.27) for the various forcing models with non-zero parameter values. The Euler-Bernoulli approximation assumed parameter values, such as $s = 0$ or $z_0 = 0$, could hide potential errors in the code. Additionally, ODE45 can determine the solution without approximating the forcing using a Fourier series. Therefore, the objective of ODE45 validation was to ensure there are no errors in the developed code and verify the validity of the Fourier series approximation to the forcing model components.

B.2.1 Pure Stick Forcing ODE45 Comparison

To evaluate pure stick forcing response, the parameters used to validate the semi-analytical convolution response by comparing to the ODE45 response are shown in Table B.4. Both responses were measured at $(\alpha = 1, \eta = 0, \zeta = z_0 - \frac{s}{\Omega}\tau)$ for the first 1ms of excitation and can be seen in Figure (B.4).

The semi-analytical convolution response and the ODE45 response are effectively the same. This gives good confidence in the analytical convolution and the respective code for pure stick forcing.

Table B.4. ODE45 Parameter list for pure stick forcing

Parameters	Value
a	0.5 in
b	1 in
c	2.5 in
F_p	1000 lbf/in
μ	0.3
Ω	$2\pi \times (20 \times 10^3)$ rad/s
λ_d	0.05
s	$\frac{c}{1.5}$
z_0	$\frac{-c}{2}$

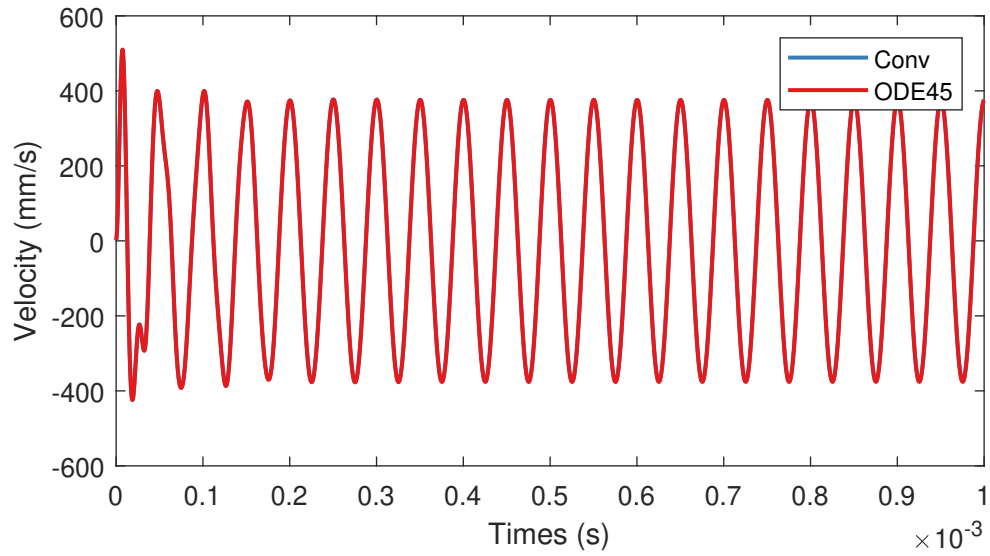


Figure B.4. Semi-analytical convolution response and ODE45 response to pure stick forcing using parameters listed in Table B.4.

B.2.2 Pure Slip Forcing ODE45 Comparison

To evaluate pure slip forcing response, the parameters used to validate the semi-analytical convolution response by comparing to ODE45 response can be seen in

Table B.5. The convolution response uses a 10-term Fourier series approximation for the f_2 and f_3 forcing component seen in Equation (2.33), and both responses were measured at $(\alpha = 1, \eta = 0, \zeta = z_0 - \frac{s}{\Omega}\tau)$ for the first 1ms of excitation and plotted in Figure (B.5). The semi-analytical convolution response and the ODE45 response

Table B.5. ODE45 Parameter list for pure slip forcing

Parameters	Value
a	0.5 in
b	1 in
c	2.5 in
F_p	1000 lbf/in
μ	0.3
Ω	$2\pi \times (20 \times 10^3)$ rad/s
λ_d	0.05
s	$\frac{c}{1.5}$
z_0	$\frac{-c}{2}$
X_{amp}	16μ m

are practically the same. This indicates that the Fourier series approximation for the pure slip forcing components was valid and the analytical convolution and respective code has no errors.

B.2.3 Partial Slip Forcing ODE45 Comparison

To evaluate partial slip forcing response, the parameters used to validate the semi-analytical convolution response by comparing to ODE45 response can be seen in Table B.6. The convolution response uses a 5-term Fourier series approximation for the f_2 forcing component seen in Equation (2.37), and both responses were simulated at $(\alpha = 1, \eta = 0, \zeta = z_0 - \frac{s}{\Omega}\tau)$ for the first 1ms of excitation and can be seen in Figure (B.6). The semi-analytical convolution response and the ODE45 response

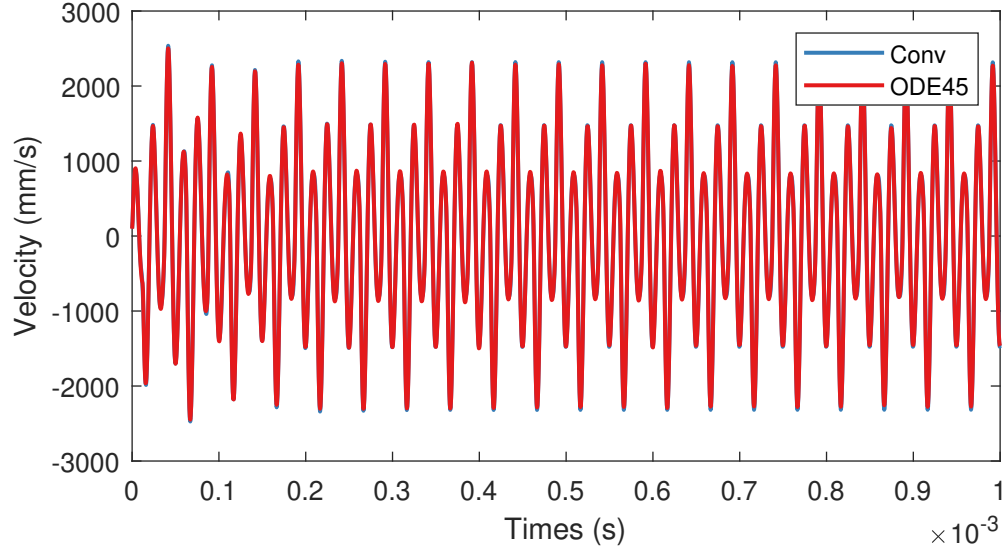


Figure B.5. Semi-analytical convolution response and ODE45 response to pure slip forcing using parameters listed in Table B.5.

Table B.6. ODE45 Parameter list for partial slip forcing

Parameters	Value
a	0.5 in
b	1 in
c	2.5 in
F_p	1000 lbf/in
μ	0.3
Ω	$2\pi \times (20 \times 10^3)$ rad/s
λ_d	0.05
s	$\frac{c}{1.5}$
z_0	$\frac{-c}{2}$
maxF	250 lbf/in

are practically the same. This indicates that the Fourier series approximation for the partial slip forcing components was valid and there are no errors in the analytical convolution and respective code.

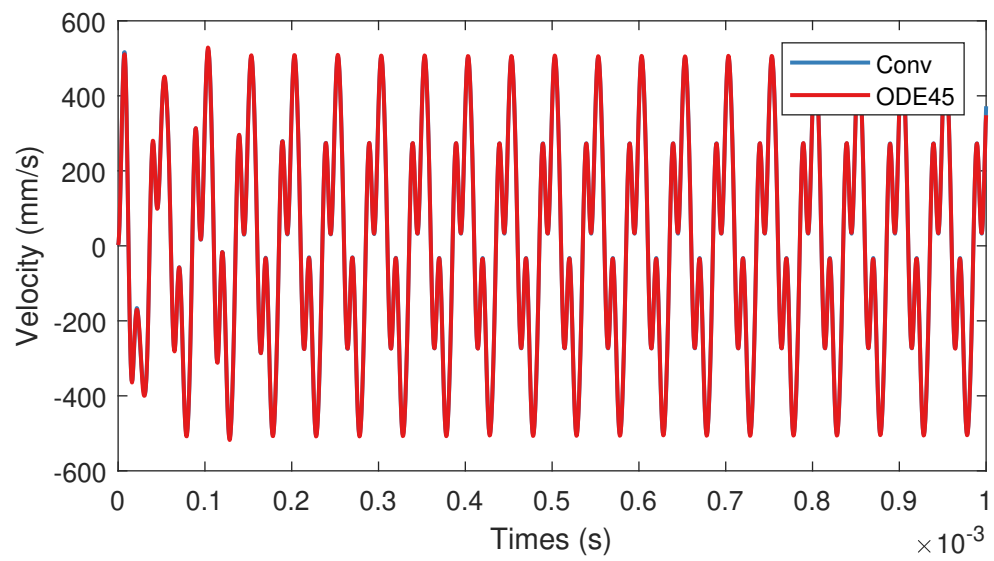
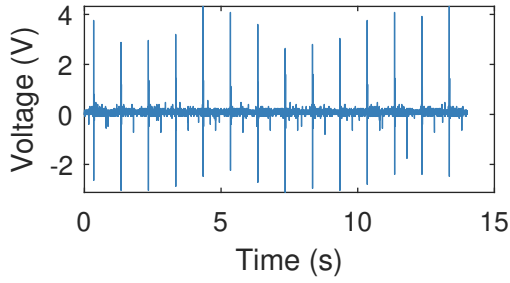


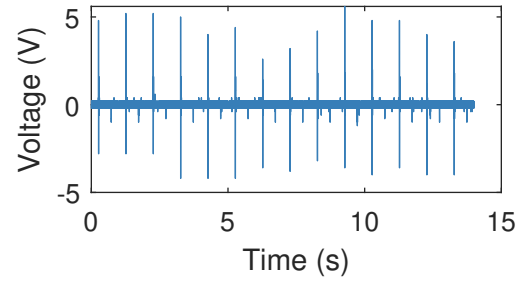
Figure B.6. Semi-analytical convolution response and ODE45 response to partial slip forcing using parameters listed in Table B.6.

C. RAW EXPERIMENTAL DATA FOR SOLENOID TESTING

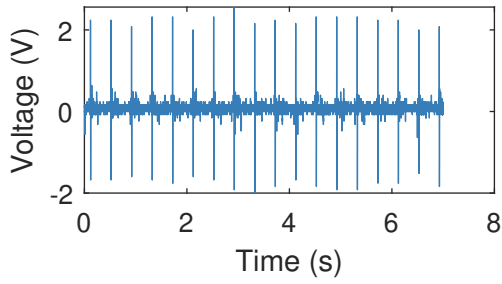
The raw data files for solenoid testing for sensors C, D and E can be seen in Figure C.1, Figure C.2, and Figure C.3. The 5V, 1Hz response plots are missing from the appendix because they are in the main body in Figure 4.7. The results for sensors C and D were used to create the calibration curves seen in Figure 4.9.



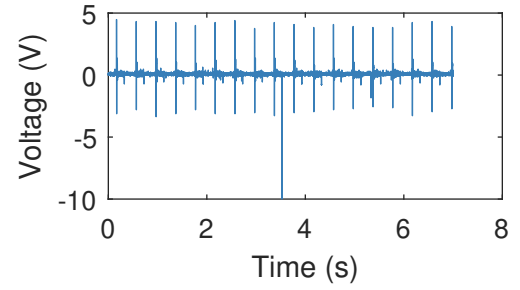
(a) 7.5 V, 1 Hz



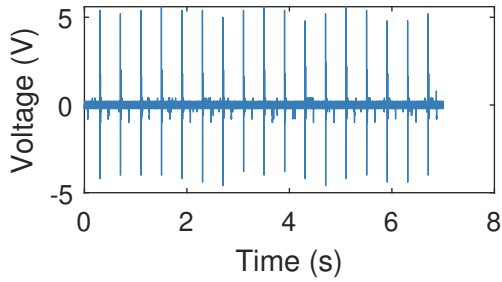
(b) 10 V, 1 Hz



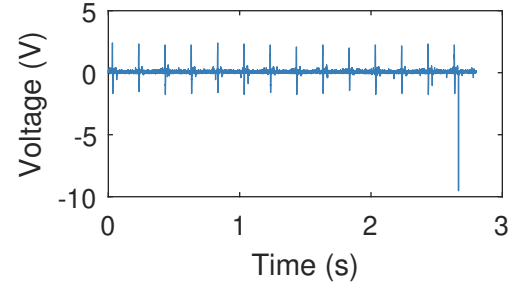
(c) 5 V, 2.5 Hz



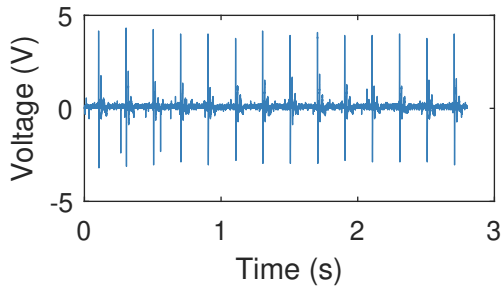
(d) 7.5 V, 2.5 Hz



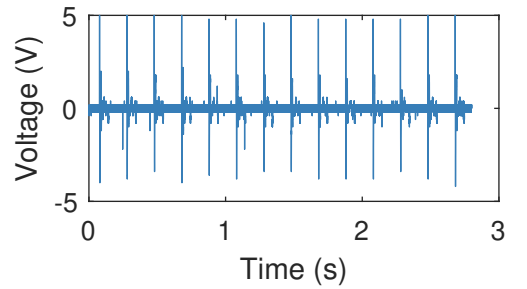
(e) 10 V, 2.5 Hz



(f) 5 V, 5 Hz



(g) 7.5 V, 5 Hz



(h) 10 V, 5 Hz

Figure C.1. Solenoid testing for sensor C, where the subfigure caption contains the respective solenoid voltage amplitude and actuation frequency.

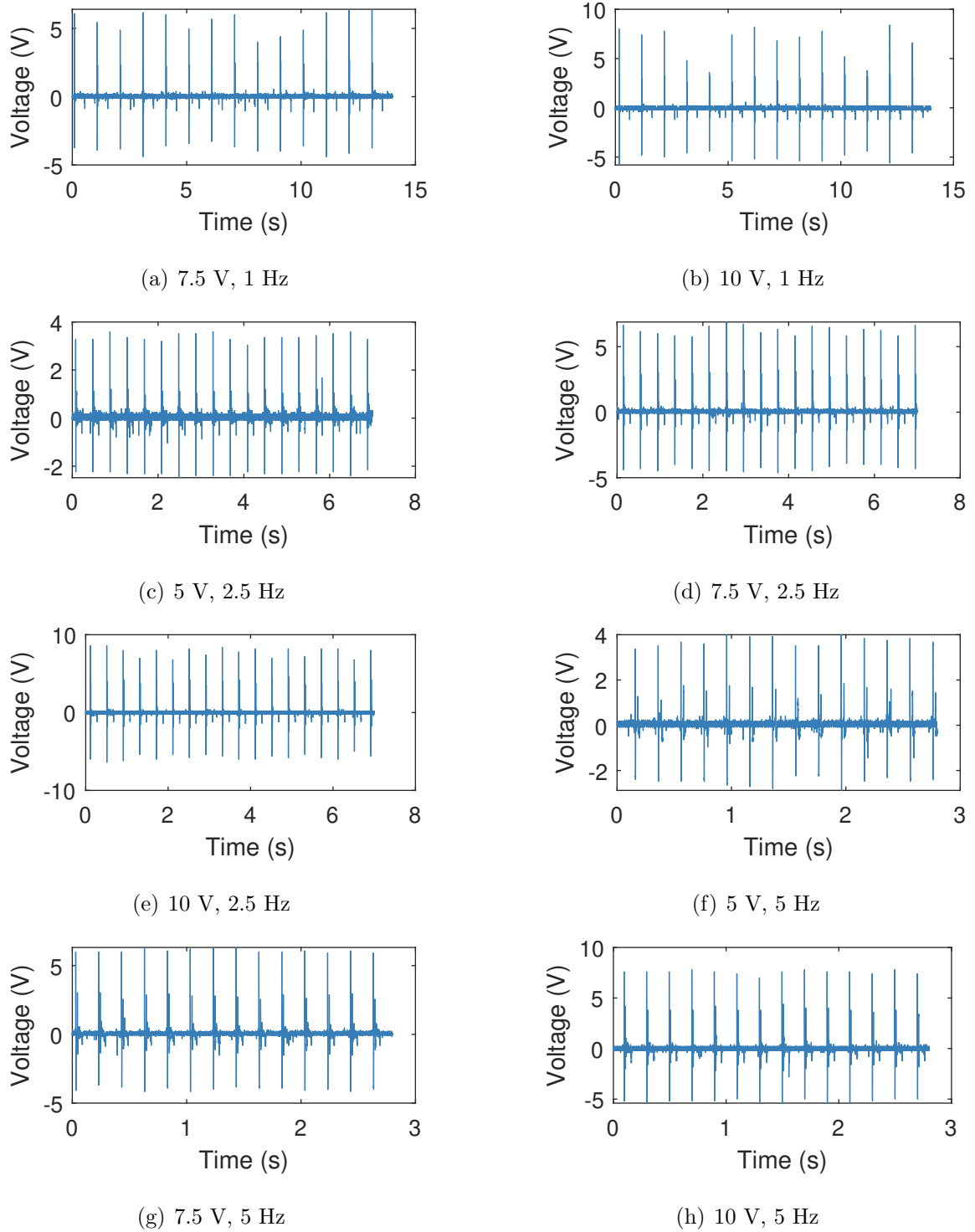
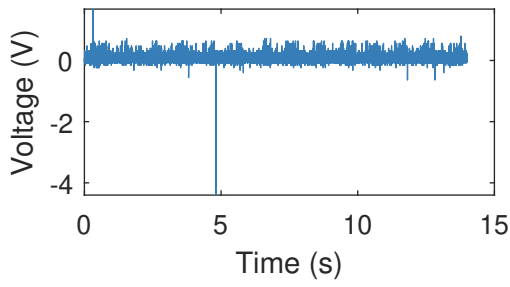
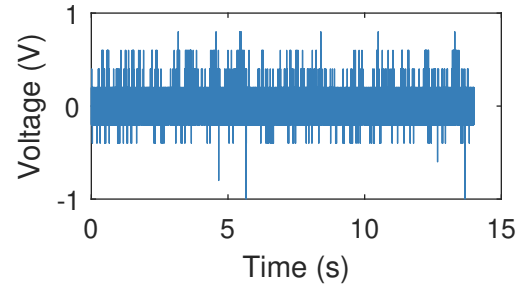


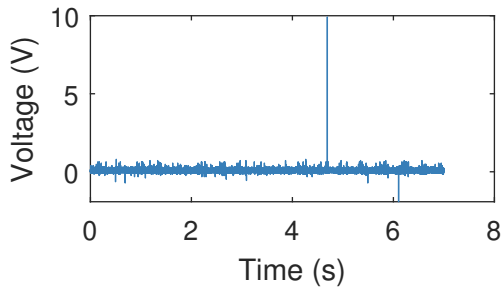
Figure C.2. Solenoid testing for sensor D, where the subfigure caption contains the respective solenoid voltage amplitude and actuation frequency.



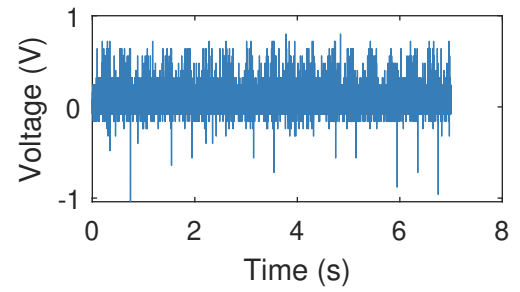
(a) 7.5 V, 1 Hz



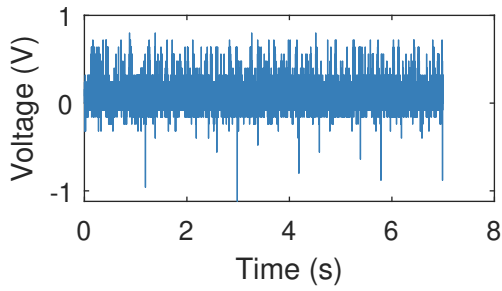
(b) 10 V, 1 Hz



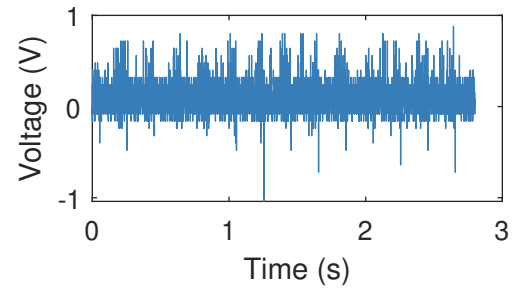
(c) 5 V, 2.5 Hz



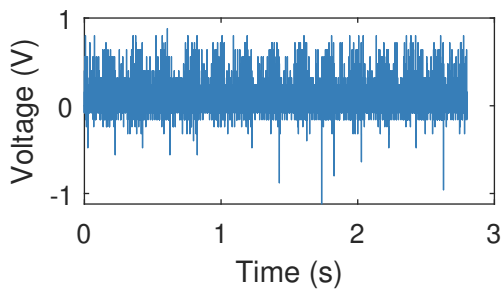
(d) 7.5 V, 2.5 Hz



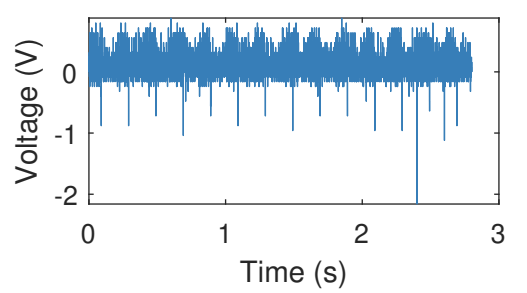
(e) 10 V, 2.5 Hz



(f) 5 V, 5 Hz



(g) 7.5 V, 5 Hz



(h) 10 V, 5 Hz

Figure C.3. Solenoid testing for sensor E, where the subfigure caption contains the respective solenoid voltage amplitude and actuation frequency.

D. FRICTION COEFFICIENT RELATIONSHIP WITH SUBSTRATE MODEL RESPONSE

In the current model, the constant coefficient of friction is assumed to be 0.3, a value chosen somewhat arbitrarily. The effect of the friction coefficient magnitude on the substrate response is explored to determine if the value chosen affects the trends with height and weld cycle. In order to explore this, the response to pure stick forcing is simulated for three values of μ : 0.3, 0.5, 0.7. The material properties are listed in Table 3.1, and the simulation parameters are listed in Table 3.4. Similar to previous simulations, the transverse velocity response under the pure slip moving line load with the three different values of μ is simulated for a substrate with dimensions $a = 0.5$ in, $b = 1$ in, and $c = 2.5$ in, and can be seen in Figure D.1.

The maximum and RMS of the transverse velocity responses are then compared to μ in Figure D.2. Based on RMS and maximum values from the responses, the model response magnitude is proportional to the constant coefficient of friction, and thus changes to a more accurate coefficient value would not impact the trends in height and during the weld cycle.

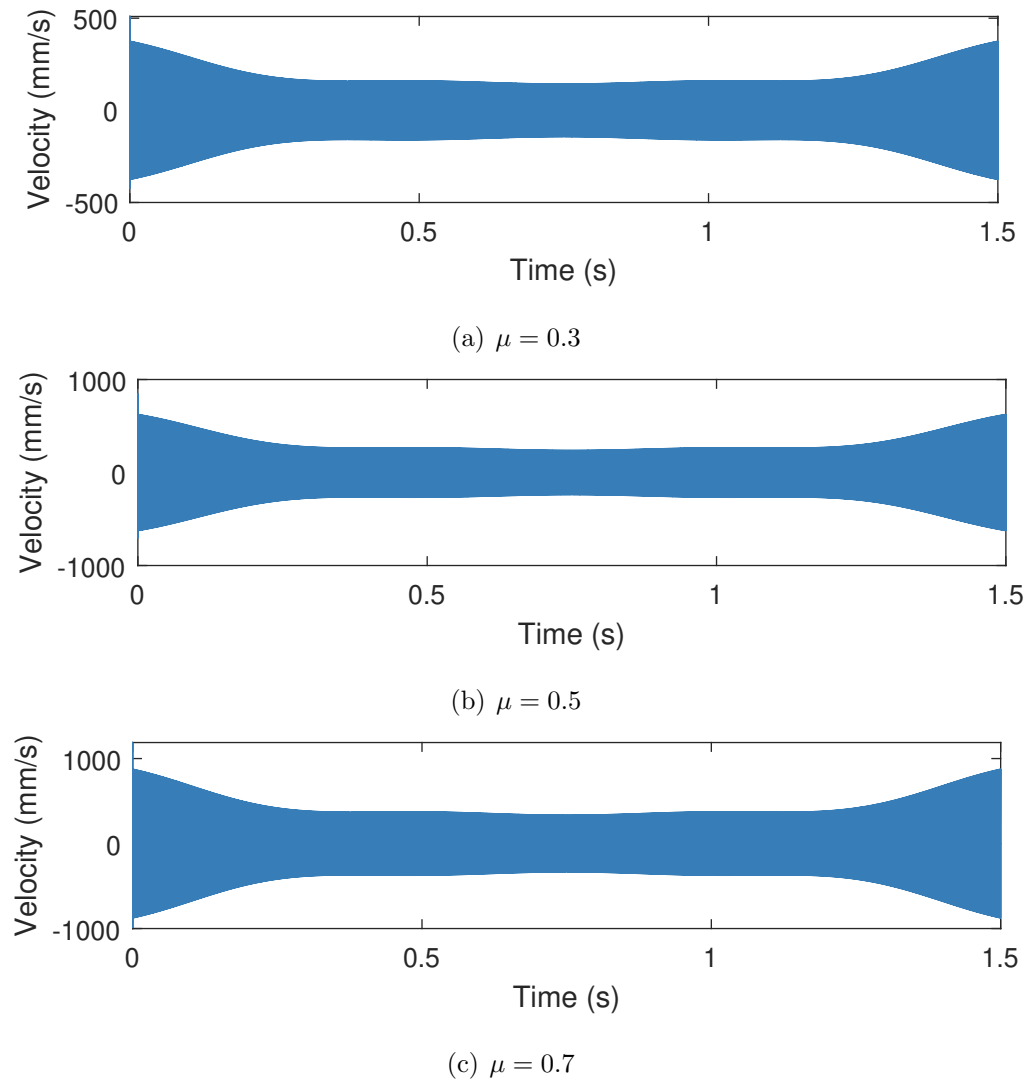


Figure D.1. The transverse velocity response under the moving line load for pure stick forcing with different coefficients of friction, μ .

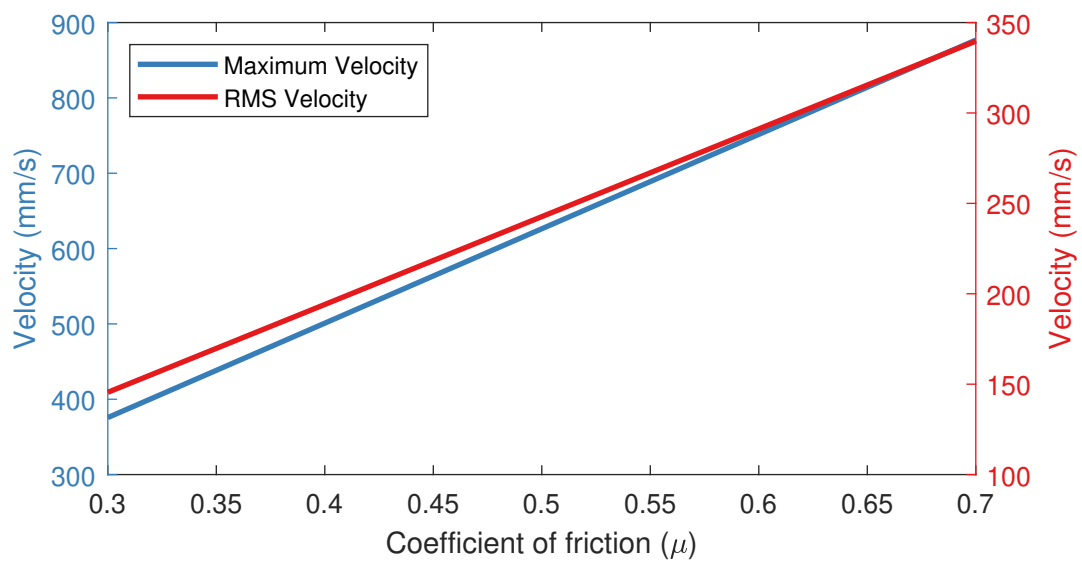


Figure D.2. Maximum and RMS value of transverse velocity response of substrate with dimensions $a = 0.5$ in, $b = 1$ in, and $c = 2.5$ in, to pure stick forcing for various coefficients of friction.

E. EXPERIMENTAL CALIBRATION OF SONOTRODE VIBRATION AMPLITUDE

The relationship between controller amplitude percent to sonotrode vibration amplitude is intrinsic to each UAM machine. This relationship does not transfer between machines, and thus must be performed prior to experimental testing and use. For our UAM machine, a Fabrisonic R220, the calibration was performed in free-air. Due to the control system for typical UAM systems, the sonotrode vibration amplitude should be similar in free-air and under load. The measurements were taken with a Polytech PSV400 scanning vibrometer. The laser placement on the sonotrode during calibration can be seen in Figure E.1, The sonotrode vibration displacement was recorded for various controller amplitude percents, and the resultant calibration curve can be seen in Figure E.2. The calibration has a near linear relationship between am-

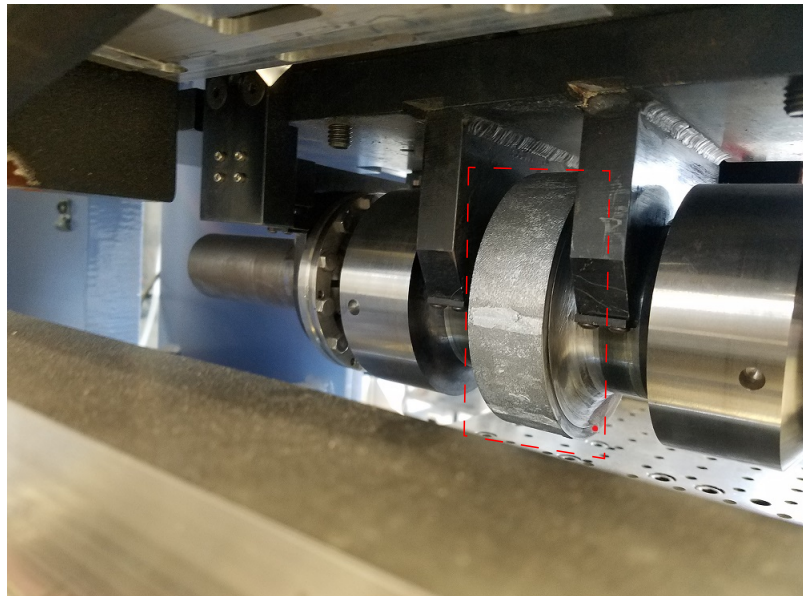


Figure E.1. Fabrisonic R220 sonotrode, marked by dotted red line, with red dot on face indicating measurement location for calibration.

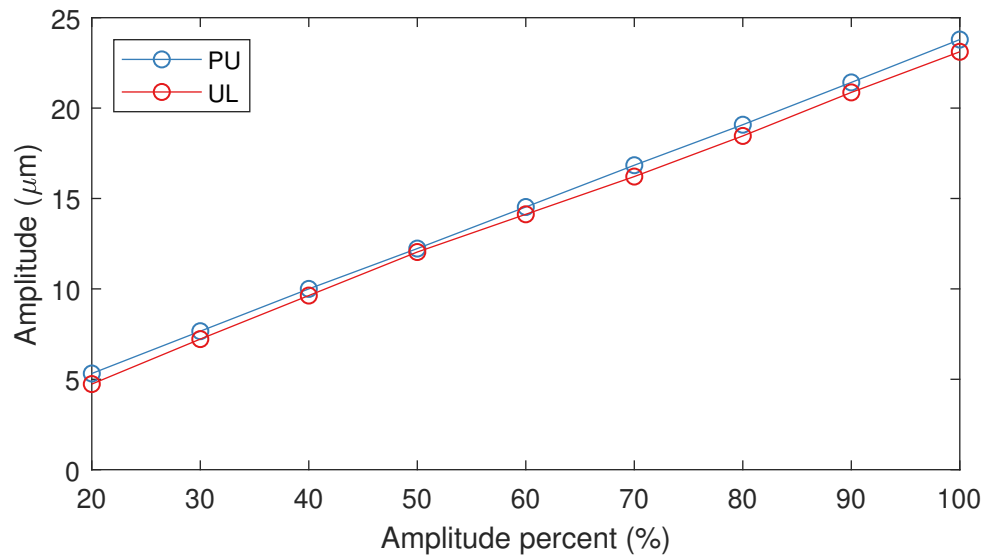


Figure E.2. Sonotrode vibration amplitude versus controller amplitude percent in free air. The line marked 'PU' is the calibration curved developed when the Fabrisonic R220 was at Purdue University and the line marked 'UL' is when it was at University of Louisville.

plitude and amplitude percent, and the calibration developed at Purdue matches with a previous calibration.

F. FABRISONIC R220 SONOTRODE CLEANING PROCEDURE

During the operation of UAM, foil or tape can bond to the sonotrode instead of the substrate, referred to as nuggeting. In order to remove aluminum nuggets, a bath of sodium hydroxide, NaOH, solution (20% W/W) is used. The NaOH solution is poured into a plastic cup, and then the cup is placed directly underneath the sonotrode. Next, the sonotrode is lowered into the NaOH bath, and the sonotrode is rotated through the bath for 4 to 8 hours depending on the severity of the nuggeting. For the previously explained process, the sonotrode cleaning set-up can be seen in Figure F.1. After the nuggets have been removed through a chemical reaction with the NaOH solution, the NaOH solution is properly discarded. Then, the sonotrode is rotated through a water bath for 10 minutes to remove NaOH solution from the surface of the sonotrode.

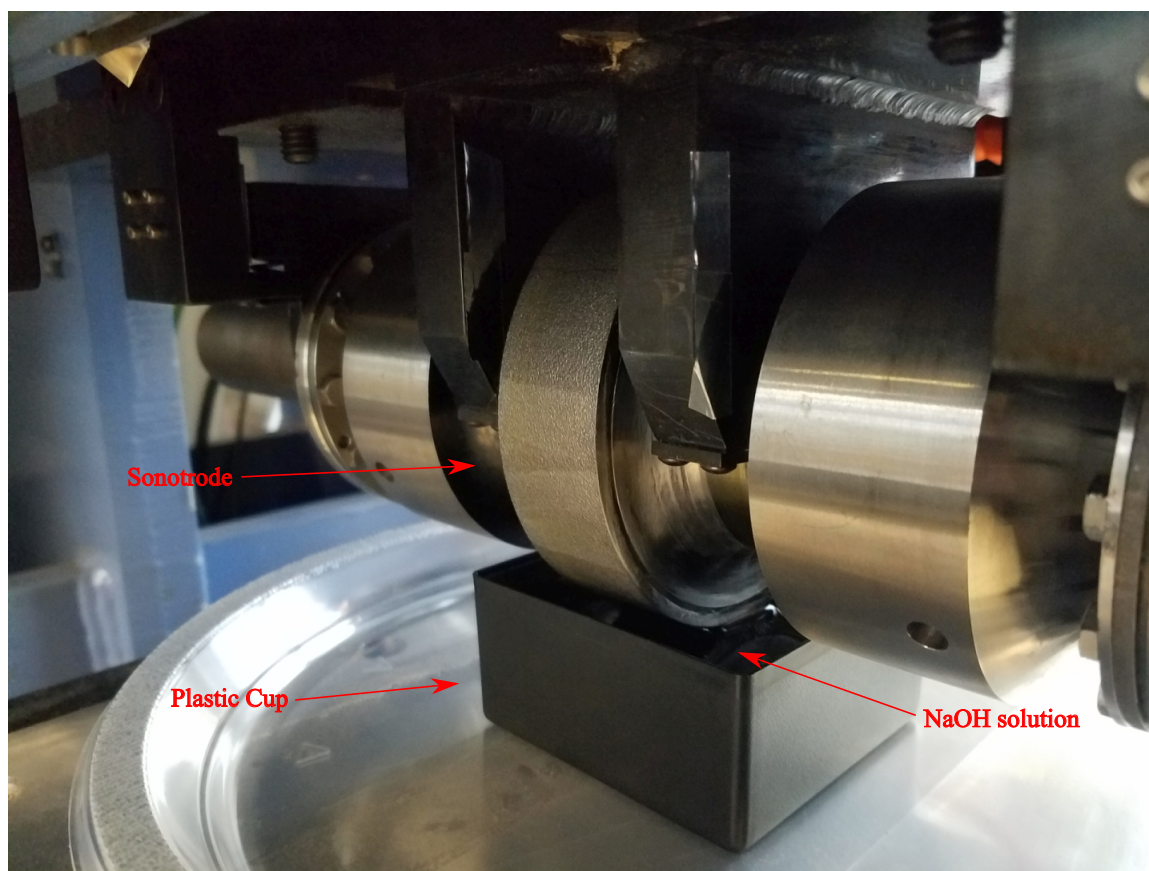


Figure F.1. Sonotrode cleaning set-up on Fabrisonic R220 UAM machine with sonotrode, plastic cup, and NaOH solution labeled.